ENERGY DEPENDENCE OF NET-Λ FLUCTUATIONS MEASURED BY THE STAR DETECTOR AT RHIC

A Dissertation Presented to

the Faculty of the Department of Physics

University of Houston

In Partial Fulfillment

of the Requirements for the Degree

Doctor of Philosophy

By

Nalinda Kulathunga Mudiyanselage

December 2018

ENERGY DEPENDENCE OF NET-Λ FLUCTUATIONS MEASURED BY THE STAR DETECTOR AT RHIC

Nalinda Kulathunga Mudiyanselage

APPROVED:

Dr. Rene Bellwied, Chairman
Department of Physics

Dr. John Miller
Department of Physics

Dr. Claudia Ratti
Department of Physics

Dr. Anthony Timmins
Department of Physics

Dr. Gomika Udugamasooriya
Collage of Pharmacy

Dean, College of Natural Sciences and Mathematics

Acknowledgements

It is my pleasure to acknowledge the many people who have assisted me throughout my graduate career. I would never have been able to finish my dissertation without the guidance of my committee members, help from friends, and support from my family. Firstly, I would like to express my sincere gratitude to my advisor Dr. Rene Bellwied for the continuous support of my Ph.D. study and related research. He was a role model for me and I will be forever grateful for his guidance, patience, and motivation. His guidance helped me in all the time of research and writing of this dissertation. I could not have imagined having a better advisor and mentor for my Ph.D. study. Besides my advisor, I would like to thank the rest of my thesis committee Dr. John Miller, Dr. Claudia Ratti, Dr. Anthony Timmins, and Dr. Gomika Udugamasooriya, for their insightful comments and encouragement throughout these five years. I would like to express my gratitude to Dr. Jochen Thaeder, Dr. William J. Llope and Dr. A. M. Schmah for their help and valuable contributions to the analysis. I am grateful to all my fellow graduate students and colleagues for the stimulating discussions, and for all the fun we have had in the last five years. I would also like to thank my parents and my brother for supporting me throughout writing this dissertation and my life in general. This journey would not have been possible without the support and guidance of my father, Mr. K. M. Kusumasena and loving mother, Mrs. H. A. Podimanike. Most importantly, I would like to thank my loving wife, Saumali Daundasekara for providing me with unfailing support and motivation. I could not have done it without her caring, support, and encouragement.

ENERGY DEPENDENCE OF NET-Λ FLUCTUATIONS MEASURED BY THE STAR DETECTOR AT RHIC

An Abstract of a Dissertation

Presented to

the Faculty of the Department of Physics

University of Houston

In Partial Fulfillment

of the Requirements for the Degree

Doctor of Philosophy

By

Nalinda Kulathunga Mudiyanselage

December 2018

Abstract

The measurement of conserved charge distributions has generated considerable interest in understanding the cumulants of conserved quantum numbers in the quantum chromo-dynamics (QCD) phase diagram, in particular the behavior near a possible critical end point and hadronization near the chemical freeze-out line. Net-protons and net-kaons have been used as proxies for net-baryons and net-strangeness, respectively. In this work, the measurement of efficiency corrected and feed-down corrected cumulant ratios ($C_2/C_1, C_3/C_2$) of net-Λ ($\Lambda - \bar{\Lambda}$) are presented. Net-Λ fluctuations were subjected to strangeness and baryon number conservation. Results are presented for five beam energies ($\sqrt{s_{NN}}$ = 19.6, 27, 39, 62.4, and 200 GeV Au + Au collisions) as a function of centrality and rapidity. We compared the net-Λ results to the published net-proton and net-kaon results at STAR. The results are presented with the comparisons to Poisson baseline, the negative binomial distribution (NBD) expectations, the ultra relativistic quantum molecular dynamics model and the hadron resonance gas (HRG) model. The data were corrected for efficiency in two ways, a transverse momentum (p_T) - dependent and a p_T - independent method. Both methods yielded similar results. Any feed-down contribution from multi-strange baryons did not affect the net-Λ cumulant ratios. A non-monotonic behavior of the net-Λ cumulant ratios indicating QCD critical point was not observed as a function of collision centrality or energy. The energy dependence of the measured net-Λ C_2/C_1 stayed closer to HRG calculations assuming kaon freeze-out conditions than the HRG calculations based on proton/charge freeze-out conditions. This could potentially be an indication of the predicted sequential hadronization. The net-Λ cumulant ratios showed weak dependence on the selected rapidity window. The deviation of NBD expectation for net-Λ C_2 from the measured C_2 increased as a function of increasing rapidity window, which could be attributed to baryon-number conservation.

Contents

List of Figures

List of Tables

Chapter 1

Introduction

1.1 The evolution of the universe

At the very early stage of it's evolution, the expansion of the universe was initiated from a very dense and high temperature state according to the Big Bang model [1]. This state of matter is predicted to be very different from what we observe today. Due to the extremely high energy density and temperature, nuclear matter could not exist the way it is at present and finally after many advancements in both theory and experiments, a new state of mater was discovered [2]. This state of matter, known as the quark gluon plasma (QGP) is the soup of free quarks and gluons which are known to be the basic constituents of nuclear matter.

Few moments after the Big Bang, the system started to cool-down and expand rapidly. Numerous phase transitions took place over a period of about thirteen billion years and resulted in the state of nuclear matter we have today. For a better understanding of this process, new theories and experiments have been established.

High energy particle collisions are the best way to probe the dynamics of a system similar to the conditions at the beginning of the universe. In these collisions, an environment similar to the very beginning of the universe is created in the lab to investigate the physics processes during the phase transitions associated with nuclear matter.

Figure 1.1 shows a schematic diagram which illustrates the different eras in the evolution of the universe. This cosmological model is based on theoretical predictions together with experimental observations. The accelerated expansion of the universe was established after the observation of supernova's cosmological red shift which is a measure of how fast the supernovae are receding from us. Furthermore, the discovery of the cosmic microwave background provides a substantial confirmation of the Big Bang picture.

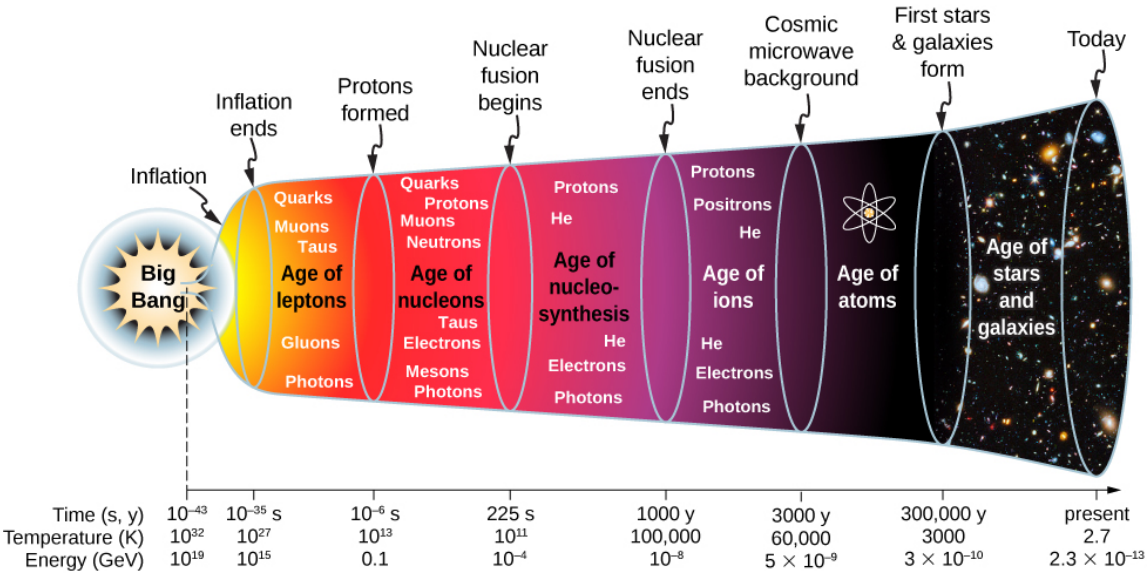

Figure 1.1: Schematic for the visualization of evolution of the universe after the Big Bang.

In this dissertation, the focus is on the phase transition from quarks and gluons to the "Age of Nucleons" in Figure 1.1, which occurred $\sim 10^{-6}$ seconds after the Big

Bang.

1.2 Standard model

The standard model is a classification of elementary particles and their interactions according to many theoretical predictions followed by their experimental confirmations. All the forces in nature can be classified into four categories namely, weak interaction, strong interaction, electromagnetic interaction, and gravity. Except for gravity, all the other interactions can be described by the standard model.

The standard model includes six leptons (electron, muon, tau, and their respective neutrinos), six quarks (up, down, charm, strange, top, and bottom), four gauge bosons (photon, gluon, Z boson, and W bosons) and the Higges boson. Figure 1.2 shows a schematic of the standard model, where the first three columns show three generations of matter, the 4^{th} column shows the gauge bosons and in the 5^{th} column, the Higges boson. Masses, charges, and quantum numbers associated with six different types of quarks are listed in Table 1.1.

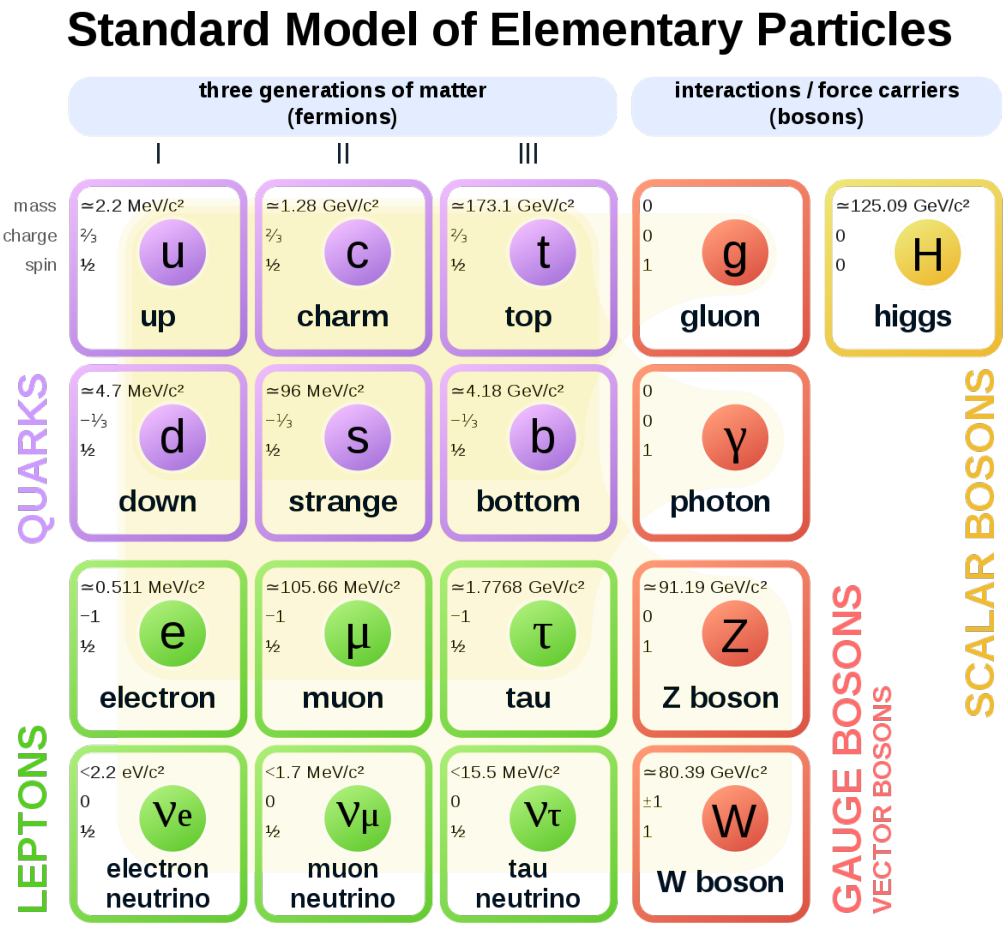

Figure 1.2: Schematic of the classification of elementary particles and interactions according to the standard model.

Theoretical descriptions of the interactions associated with three generations of matter (quarks and leptons) via the gauge bosons are supported by quantum electrodynamics (QED), quantum chromodynamics (QCD), and electro-weak theory (EWT). QED explains the interaction of charged particles through photons. Z bosons and W bosons are the weak force carriers as described by EWT. Finally, QCD describes the interaction between quarks and gluons through the exchange of *color charge*.

Table 1.1: List of quarks with their symbols, masses, charges, and corresponding quantum numbers.

Quark	Symbol	Mass (MeV)	Charge	Quantum No.
Up	u	$1.5 \longrightarrow 4$	$+\frac{2}{3}$	Isospin $= +\frac{1}{2}$
Down	d	$3 \longrightarrow 8$	$-\frac{1}{3}$	Isospin $= -\frac{1}{2}$
Strange	s	$80 \longrightarrow 130$	$-\frac{1}{3}$	Strangeness $= -1$
Charm	c	$1150 \longrightarrow 1350$	$+\frac{2}{3}$	Charmness $= +1$
Bottom	b	$4100 \longrightarrow 4400$	$-\frac{1}{3}$	Bottomness $= -1$
Top	t	$1.743 \times 10^5 \pm 5100$	$+\frac{2}{3}$	Topness $= +1$

1.3 Quantum Cromodynamics (QCD)

As mentioned earlier, quarks experience the strong interaction because they carry color charges. Color-charge, is in many ways analogous to the electric charge. However, there are important differences. One of them, the electric charge, is a scalar, but color-charge is not. The total color-charge of a system can be obtained by combining the individual charges of the constituents according to the group theoretic rules analogous to those used when combining angular momenta in quantum mechanics. There are three different color-charge states *red, green,* and *blue*. QCD is the theory of strong interactions where these color-charge quantum numbers are used to explain the interactions between quarks and gluons. *Color confinement* and *asymptotic freedom* are two phenomena in QCD that are essential in understanding the strong interaction. These phenomena will be briefly discussed in the next sections.

1.3.1 Asymptotic freedom

One of the prominent features in QCD is the phenomenon called *asymptotic freedom*. It states that the interaction strength between quarks, which is also known as the coupling constant (α_s) becomes weaker as the distance between the quarks gets smaller.

In electrodynamics, the interaction between two charged particles in a vacuum is described by the Coulomb law. But in quantum field theory, the vacuum is not empty and vacuum fluctuations can occur when a photon passes through it. The interaction between two electrons in a vacuum is given by $F = \alpha_{em}(r)/r^2$ where, α_{em} is the fine structure constant which depends on the distance, r, or the momentum transfer, q. The dependence of α_{em} on the momentum scale (or $\frac{1}{r}$ scale) can be determined by the differential equation,

$$\mu \frac{d\alpha(\mu)}{d\mu} = \beta(\alpha(\mu)) \tag{1.1}$$

Here μ stands for the momentum scale and the β function may be calculated in perturbation theory and the solution for the α_{em} is,

$$\alpha_{\mathrm{em}}(\mu) = \frac{\alpha_{\mathrm{em}}\left(\mu_0\right)}{1 - \frac{\alpha_{\mathrm{em}}(\mu_0)}{3\pi} \ln \frac{\mu^2}{\mu_0^2}} \tag{1.2}$$

Here, it is obvious that the coupling becomes stronger when the distance gets shorter. That means, QED becomes a highly coupled theory at short distances. In QCD, the same differential equation holds except the β function is now different,

$$\beta(\alpha) = -\frac{\beta_0}{2\pi}\alpha^2 + \ldots \tag{1.3}$$

From the re-normalization group equation, the strong coupling constant (α_s) can be derived as in Equation 1.4. This shows that, when the momentum scale approaches ∞ ($r \longrightarrow 0$), the coupling approaches 0 and this phenomena is called *asymptotic freedom*. This characteristic of α_s allows the use of the perturbative approach to study free quark matter at large momentum transfers in a system such as the one produced by heavy-ion collisions. Here, Λ_{QCD} is the scale at where the coupling becomes larger and the perturbative approach fails.

$$\alpha_s(\mu) = \frac{2\pi}{\beta_0 \ln\left(\mu/\Lambda_{\mathrm{QCD}}\right)} \tag{1.4}$$

This peculiar behaviour of the strong coupling as a function of running scale, Q, is experimentally verified as shown in Figure 1.3.

1.3.2 Color confinement

One other prominent feature in QCD in the low-energy regime (distance scale $> 1/\Lambda_{QCD}$) is the *color confinement*. As mentioned in Section 1.2, gluons and photons are the mediators of the force between their respective particles quarks and charged. However, there is an important difference. Photons have no charge but, gluons carry color charges which give rise to the phenomenon called *color confinement*.

If two electrically charged particles are separated, the force between them decreases as the distance increases. This is because photons irradiate in all directions and the intensity decreases as $\sim 1/r^2$. In QCD, this is different because the flux between two quarks acts in a way that it irradiates from a so-called "color-flux tube". Thus, the force between quarks does not decrease but stays constant as the distance increases. Eventually, if the tube contains enough energy, then it will breakdown

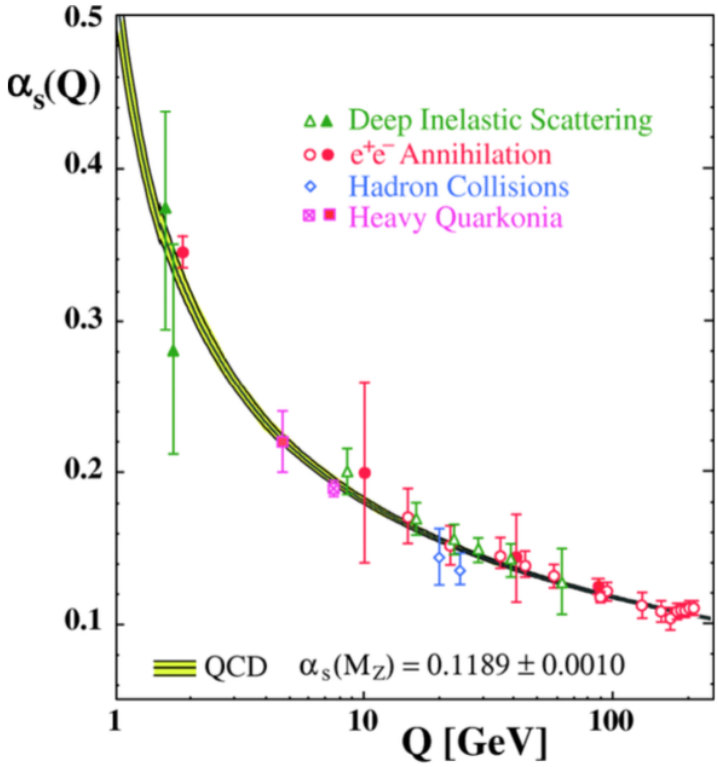

Figure 1.3: Comparison of QCD expectation of the running coupling constant and results from different experimental observations as a function of energy scale Q [3].

into a quark and anti-quark pair.

This phenomenon can further be explained by considering the potential $V_S(r)$,

$$V_S(r) \propto -\frac{4}{3}\frac{\alpha_S}{r} + kr \tag{1.5}$$

Here, r is the distance between the quarks, α_s is the strong coupling constant, and k is the field energy per unit length which describes long range interactions. At short distances, Equation 1.5 resembles the Coulomb interactions while at large distances, the kr term dominates. Therefore, in nature, color-charged particles can not be isolated and always come in the form of color-neutral hadrons.

1.3.3 QCD phase diagram

The phase diagram is a representation of the existence of different states associated with matter with respect to certain thermodynamic variables such as temperature, pressure, or density. For instance, the phase diagram of water represents the different states of water as a function of pressure and temperature. The nuclear matter phase diagram (also known as QCD phase diagram) represents the state of nuclear matter as a function of baryon chemical potential (μ_B) and temperature (T). One version of the QCD phase diagram is shown in Figure 1.4.

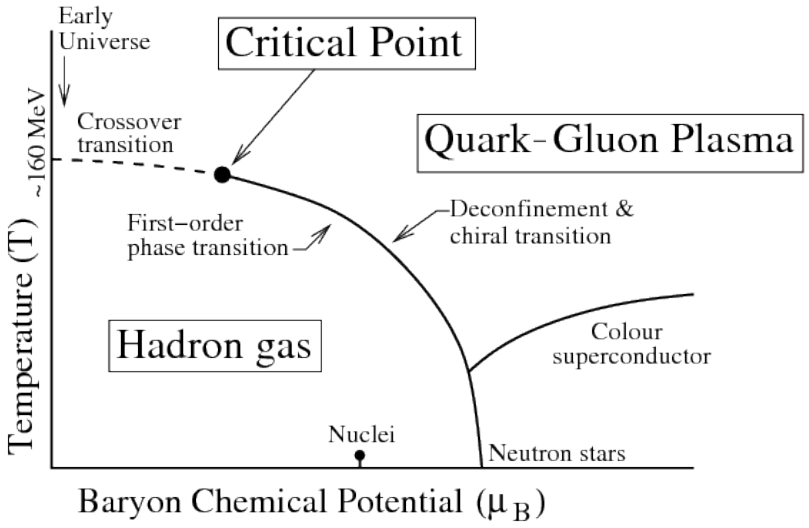

Figure 1.4: QCD phase diagram: state of nuclear matter as a function of temperature (T) and baryon chemical potential (μ_B).

In the QCD phase diagram, the baryon chemical potential, which is the measure of imbalance between matter and anti-matter, is plotted along the horizontal axis. Zero μ_B represents the perfect balance between matter and anti matter. The variable along the vertical axis is the temperature.

Led by various model predictions and experimental observations, boundaries and

limits in the QCD-phase diagram have been established. However, not all the characteristics in the QCD-phase diagram are confirmed by the experiments. Nevertheless both theory and experiments suggest that there should be distinct phases in the phase diagram. In the low-temperature region and around $\mu_B \sim 940$ MeV, there exists the ground state of nuclear matter. At temperatures greater than ~ 160 MeV (critical temperature), the phase becomes independent of the μ_B and the only possible phase is the QGP. Below the critical temperature, quarks and gluons are confined into hadrons.

The phase boundary between QGP and the hadron gas can be of different types. At very low μ_B, the phase transition is expected to be a smooth crossover where both phases can co-exist across the transition. On the other hand, when μ_B is finite, the phase transition is of 1^{st} order, where the first derivative of the Gibbs free energy with respect to the order parameters is discontinuous. According to this description, there should be an end-point to the first order phase boundary. That end point is shown in Figure 1.4 and called the *critical point*. Searching for the precise location of the critical end point in the QCD phase diagram is one of the challenging research areas in high-energy physics.

During a heavy-ion collision, the initial QGP state can be achieved and the system starts to evolve starting from very high temperatures (> 160 MeV). Then it cools-down and rapidly expands. This expansion is nearly isentropic which follows the trajectory of constant $d\mu_B/dS$, where S stands for the entropy. Both temperature and μ_B decrease in this process and eventually a phase transition takes place. Depending on the μ_B of the initial system (i.e. depending on the energy of the collision), the system can undergo either a first-order or a crossover transition. In the first-order transition regime, the phase will follow a path along the phase boundary

at the transition due to the generation of latent heat. In the crossover regime, there is no latent heat involved. Finally, the system will transit into a hadron gas of baryons and mesons and isentropically cool down.

1.4 Freeze-out parameters

At the very initial stage ($\sim fm/c$, where c denotes the speed of light) after the heavy-ion collision, the system experiences many hard processes such as fragmentation, quark pair production, and jet production. Once the system approaches the phase transition, the QGP hadronizes into a hadron gas with a fixed chemical composition. This process is called the *chemical freeze-out*. The system is in equilibrium at this time and the temperature (T) and the chemical potential (μ_B) can be defined as chemical freeze-out parameters. All the inelastic collisions stop at the chemical freeze-out and as a result, particle multiplicities get fixed. Then, these produced particles collide elastically and exchange their momenta. After the momenta become fixed, the system reaches the *kinetic freeze-out*. Figure 1.5 shows an illustration of the evolution of the system in space and time.

1.4.1 Susceptibilities of conserved charges

Conservation laws play an important role in the evolution of the system after heavy-ion collisions. Net-charge (ΔQ), net-baryon number (ΔB), and net-strangeness (ΔS) are conserved quantum numbers. Globally, these conserved quantum numbers should not fluctuate. But in an analysis where the data are recorded/analyzed in

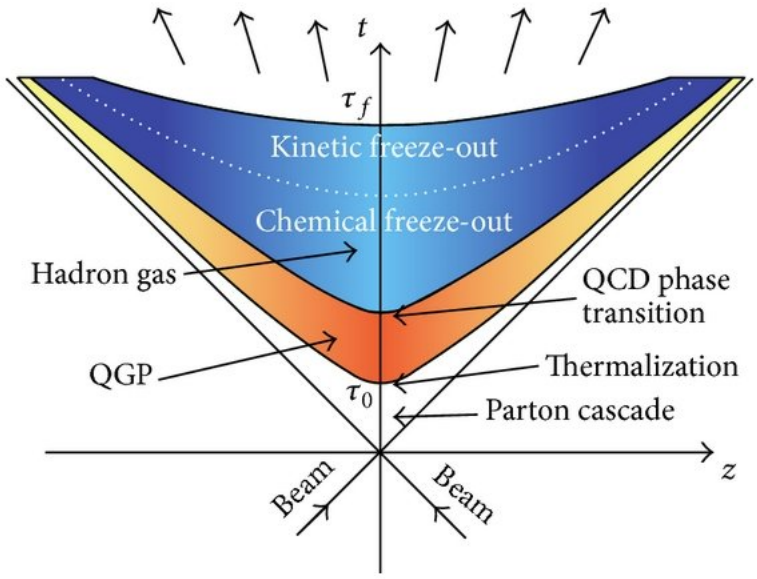

Figure 1.5: Evolution of the system after the heavy ion collision. vertical and horizontal axes represent time and space, respectively. Origin represents the moment of impact [4].

a finite acceptance, these quantities can fluctuate. Fluctuations of conserved quantum numbers are important because they carry information about the freeze-out parameters at the QCD-phase transition.

In a system after a heavy-ion collision, quantum number fluctuations can not be measured directly. Therefore, proxies for these quantum numbers such as, net-charged particles for the net-charge quantum number, net-protons for the net-baryon quantum number and net-kaons for the net-strangeness quantum number are used. These net-multiplicity distributions can be directly and accurately measured with the help of particle identification techniques used in modern-day particle detectors and as a result, fluctuations of conserved quantum numbers can be monitored.

The fluctuations of net-particle multiplicity distributions have relationships with the theoretically calculated susceptibilities. The susceptibility in thermodynamics is

the derivative of the pressure with respect to variations in baryon chemical potential and is expressed as

$$\chi_{lmn}^{QBS} = \frac{\partial^{l+m+n} p/T^4}{\partial \left(\mu_B/T\right)^l \partial \left(\mu_S/T\right)^m \partial \left(\mu_Q/T\right)^n} \tag{1.6}$$

Here, Q, B, and S stand for charge, baryon number, and strangeness, respectively. l, m, and n stand for different orders of the susceptibility. T stands for the temperature and μ stands for the chemical potential. Susceptibilities can be modeled in theory with the help of the partition function (Z) as

$$\chi_{lmn}^{QBS} = \frac{1}{VT^3} \frac{\partial^{l+m+n} (\ln Z)}{\partial \left(\mu_B/T\right)^l \partial \left(\mu_S/T\right)^m \partial \left(\mu_Q/T\right)^n} \tag{1.7}$$

Once the susceptibilities are constructed in theory as a function of temperature and chemical potential, then the extraction of freeze-out parameters can be done as explained in the next section.

1.4.2 Extraction of freeze-out parameters

As discussed in the previous sections, fluctuations and correlations of conserved quantum numbers can be used to probe the nature of strongly interacting matter as described in QCD. Lattice QCD (LQCD) calculations provide theoretical interpretations of the nature of the strong interaction. LQCD puts quarks and gluons on a discrete space-time grid and numerically simulates their interactions. Here susceptibilities can be calculated based on this lattice where the gluons live on the lattice links and quarks on the sites. For instance, as explained in [5], at vanishing μ_B, n^{th} order susceptibility of net-baryon number fluctuations can be calculated as

$$\chi_n^B = \frac{1}{VT^3} \left. \frac{\partial^n \ln Z}{\partial \left(\mu_B/T\right)^n} \right|_{\mu_B=0} \tag{1.8}$$

For small, non-zero, values of μ_B, χ_n^B can be approximately calculated by expanding it in a Taylor series as

$$\chi_{n,\mu}^B = \sum_{k=0}^{\infty} \frac{1}{k!} \chi_{k+n}^B(T) \left(\frac{\mu_B}{T}\right)^k \tag{1.9}$$

Ratios of susceptibilities with appropriate orders are related to the ratios of moments of the measured net-particle multiplicity distributions as

$$\frac{\sigma_B^2}{M_B} = \frac{\chi_{2,\mu}^B}{\chi_{1,\mu}^B}, \quad S_B\sigma_B = \frac{\chi_{3,\mu}^B}{\chi_{2,\mu}^B}, \quad \kappa_B\sigma_B^2 = \frac{\chi_{4,\mu}^B}{\chi_{2,\mu}^B} \tag{1.10}$$

Here, M_B, σ_B, S_B, and κ_B stand for mean, standard deviation, skewness, and kurtosis of net-baryon probability distributions, respectively. Consider the Taylor expansion of the simplest even-odd ratio, $\chi_{2,\mu}^B/\chi_{1,\mu}^B$

$$\frac{\sigma_B^2}{M_B} \equiv \frac{\chi_{2,\mu}^B}{\chi_{1,\mu}^B} = \frac{T}{\mu_B} \left[\frac{1 + \frac{1}{2}\frac{\chi_4^B}{\chi_2^B} \left(\mu_B/T\right)^2 + \ldots}{1 + \frac{1}{6}\frac{\chi_4^B}{\chi_2^B} \left(\mu_B/T\right)^2 + \ldots} \right] \tag{1.11}$$

A similar relationship holds for the next even-odd ratio, $\chi_{3,\mu}^B/\chi_{2,\mu}^B$. Therefore, to the leading order, the above approach can be used to extract the $\frac{T}{\mu_B}$ ratio at the chemical freeze-out at small to vanishing μ_B. The extraction of the freeze-out temperature can be addressed by the even-even ratios of cumulants. For instance, the Taylor series expansion of $\frac{\chi_{4,\mu}^B}{\chi_{2,\mu}^B}$ at vanishing μ_B gives,

$$\kappa_B\sigma_B^2 \equiv \frac{\chi_{4,\mu}^B}{\chi_{2,\mu}^B} = \frac{\chi_4^B(T)}{\chi_2^B(T)} \left[\frac{1 + \frac{1}{2}\frac{\chi_6^B(T)}{\chi_4^B(T)} \left(\mu_B/T\right)^2 + \ldots}{1 + \frac{1}{2}\frac{\chi_4^B(T)}{\chi_2^B(T)} \left(\mu_B/T\right)^2 + \ldots} \right] \tag{1.12}$$

Here, the temperature can be extracted from the explicit temperature dependence of even-even susceptibility ratios to the leading order as seen in the above expansion at $\mu_B = 0$. Further details and assumptions about these formulations can be found in [5]. The use of the hadron-resonance gas (HRG) model for the determination of freeze-out conditions is explained in Section 3.13.5.

1.5 Motivation and goals

Previously, in fluctuation measurement studies, various proxies for conserved quantum numbers have been used to compare the experimental observations with theory in order to determine the properties of the QCD-phase boundary. Net-charge and net-proton measurements are considered reasonable proxies for net-charge and net-baryon quantum numbers, respectively. But in the case of strangeness measurements, kaons alone do not provide a complete proxy since they only represent $\sim$ 70% of the strangeness in the system. Most of the remaining strangeness ($\sim$20%) is in the Lambda (Λ) baryon. The quark content of Λ baryon is up (u), down (d), and strange (s) and its anti-particle ($\bar{\Lambda}$) consists of anti-up ($\bar{u}$), anti-down ($\bar{d}$), and anti-strange ($\bar{s}$) quarks.

The primary goal of this study is to provide the net-Λ measurement for the study of net-strangeness fluctuations. Net-Λ fluctuation measurements together with the net-kaon measurements will provide a more complete measurement of the net-strangeness in the system after the collision. Furthermore, the study of the fluctuations of net-Λ distributions is important because Λs carry both baryon and strangeness quantum numbers. This provides an opportunity to investigate freeze-out parameters in the context of quark-mass dependence. With the help of HRG

and LQCD model calculations, net-Λ measurements could provide valuable information about which quarks (light quarks or heavy quarks) play a prominent role at the time of hadronization. Therefore, the second aim of this study is to compare volume-independent net-Λ measurements to theoretical models and investigate the predicted sequential hadronization [6].

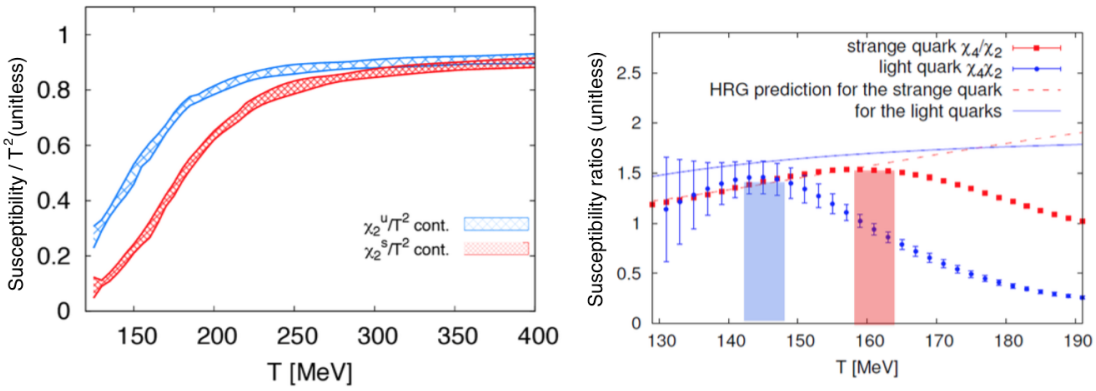

Figure 1.6: (left): Continuum extrapolated lattice QCD results for χ_2^u and χ_2^s [6], (right): Continuum extrapolated lattice QCD results for χ^4/χ^2 for light and strange quarks in comparison to HRG model calculations [7].

Theoretical calculations on the chemical freeze-out conditions (T, μ_B) in the context of different quark masses have been done using Lattice QCD and HRG models [7][8]. Figure 1.6 (left) shows a lattice QCD calculation of χ_2^u and χ_2^s where u and s super-scripts stand for *up* quarks and *strange* quarks, respectively. It is clear that for temperatures less than $\sim$ 250 MeV, the results show distinct values for different quark masses. Figure 1.6 (right), shows a comparison of χ^4/χ^2 calculated for light and strange quarks using lattice QCD results and HRG results. The main difference between these two calculations is that only lattice calculations include the quark phase and HRG does not. Therefore, the temperature at which the lattice curves deviate from HRG possibly points to the deconfinement temperature and this temperature for light quarks is less than it is for strange quarks as seen in Figure 1.6

(right).

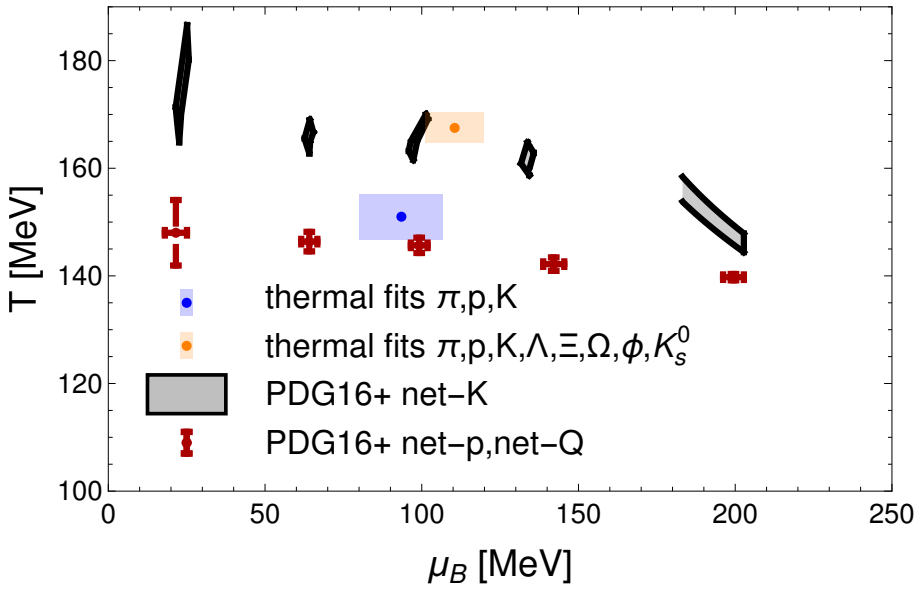

Figure 1.7: Temperature (T) and baryon chemical potential (μ_B) calculated at the chemical freeze-out using thermal fits for experimentally measured particle yields and comparing HRG model calculations with cumulant ratios of net-kaon, net-proton, and net-charge multiplicity distributions [9].

The prediction of sequential hadronization is addressed in detail by comparing HRG models with measured particle yields and net-particle multiplicity distributions as shown in Figure 1.7 where the freeze-out temperature (T) is presented as a function of chemical potential (μ_B). Two sets of points in gray and red color show the extracted freeze-out parameters from a HRG model using the measured net particle multiplicity fluctuations from STAR. Two individual points in light orange and blue show freeze-out parameters extracted using thermal fits to experimentally measured particle yields in STAR. In both HRG and thermal fits, it is clear that the freeze-out parameters follow different patterns for different particle species. Specifically in the presence of strange quarks as in kaons and Λ particles, the freeze-out curves show different values than for particles with light-quark content such as pions or protons.

With these theoretical and experimental observations, there is clearly a need for measuring net-Λ fluctuations to investigate and establish the validity of above mentioned observations. Therefore in this dissertation, we report the first measurement of net-Λ cumulants (C_1, C_2, and C_3) and cumulant ratios (C_2/C_1, C_3/C_2) as a function of collision centrality, collision energy, and rapidity.

Chapter 2

Experimental Set-up

2.1 Relativistic Heavy Ion Collider (RHIC)

The Relativistic Heavy Ion Collider (RHIC) is a particle accelerator capable of colliding accelerated heavy ions and polarized protons at a speed very close to the speed of light. RHIC is located at Brookhaven National Laboratory (BNL) in Upton, New York. An aerial view of RHIC is shown in Figure 2.1. Presently, the only actively operating heavy ion collision physics experiment at RHIC is the Solenoidal Tracker At RHIC (STAR) experiment. The primary objective of the STAR experiment is to investigate the creation and evolution of the QGP. The analysis presented here is based on the particle data collected with the STAR detector. The pioneering High Energy Nuclear Interaction eXperiment (PHENIX) was another major experiment at RHIC which completed its operations in 2017. There were two other experiments operated at RHIC namely, PHOBOS [10] and BRAHMS [11] and both completed operations in 2006 and 2005, respectively. The RHIC ring is $\sim$ 1.2 km in diameter

and is one of the largest particle accelerator facilities in the world besides the Large Hadron Collider (LHC) at CERN. RHIC started operations in the year 2000 and achieved many scientific discoveries such as the discovery of the QGP in 2005. The STAR experiment is located in the 6 o'clock position in the RHIC ring as shown in Figure 2.1.

Heavy-ion beams are prepared for the injection into the RHIC ring through several important steps. The Tandem Van de Graaff accelerator (TANDEMS) creates ions by stripping out electrons from atoms and prepare them for the acceleration. There is a 700 m long tunnel called TANDEMS to Booster (TtB) which delivers heavy ions from TANDEMS to the Alternating Gradient Synchrotron (AGS). The AGS receives protons and other ions from Booster and accelerates them before injecting into the RHIC ring. The last of the electrons are stripped out from atoms at AGS and the resulting heavy ions are focused in both horizontal and vertical directions at the same time by applying an alternating field gradient. Finally, the prepared ion beam is separated into two beams (yellow beam and blue beam) as it enters the RHIC ring. Beams are injected to the RHIC ring so that they travel in opposite directions as shown in Figure 2.1 by the yellow and blue color rings. RHIC has the capability of colliding nuclei from 5 - 200 GeV per nucleon and polarized protons up to 510 GeV.

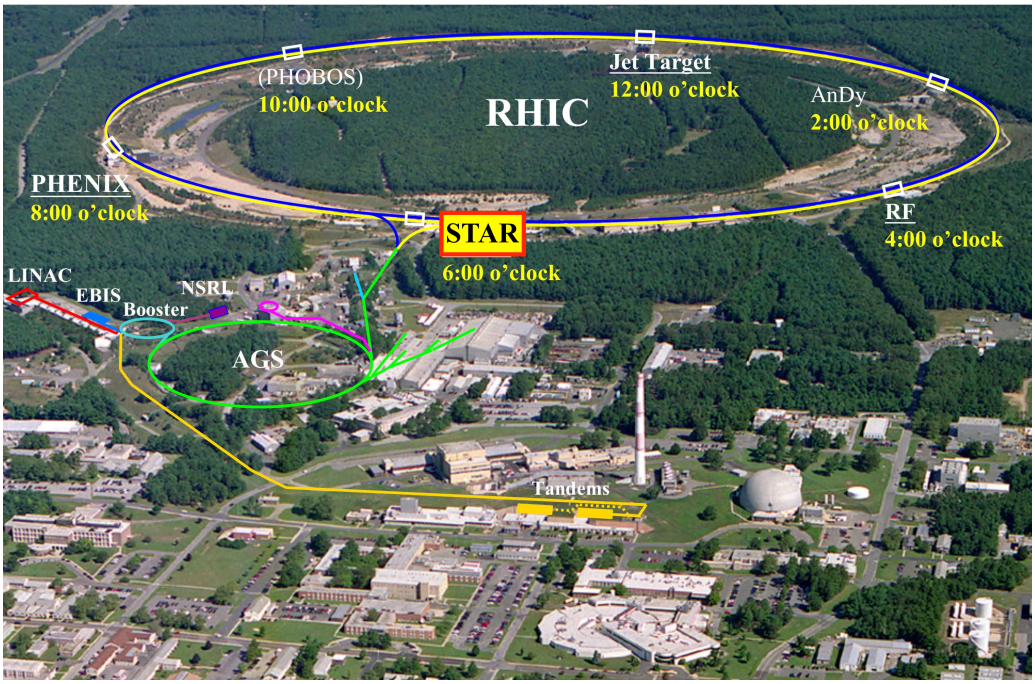

Figure 2.1: Areal view of RHIC accelerator and different experiments associated with the collider [12].

2.2 Solenoidal Tracker At RHIC (STAR) detector system

The STAR detector system consists of several sub detectors and a cross sectional view of the detector complex is shown in Figure 2.2. Weighing over 1200 tons, STAR is a massive detector system which has been updated by adding many features over the past two decades of its operating time. In the following sections, only the most important features of the STAR detector system are discussed. For guidance, the Cartesian coordinate system used at STAR is shown in the top left hand corner of Figure 2.2. In the STAR coordinate system, z-axis points along west, x-axis along south, and y-axis upwards. The beam line is shown in red and it enters the detector system along the z-axis. STAR consists of a magnet of length 6.85 m which produces

a 0.5 Tesla magnetic field along the beam line direction (z-direction).

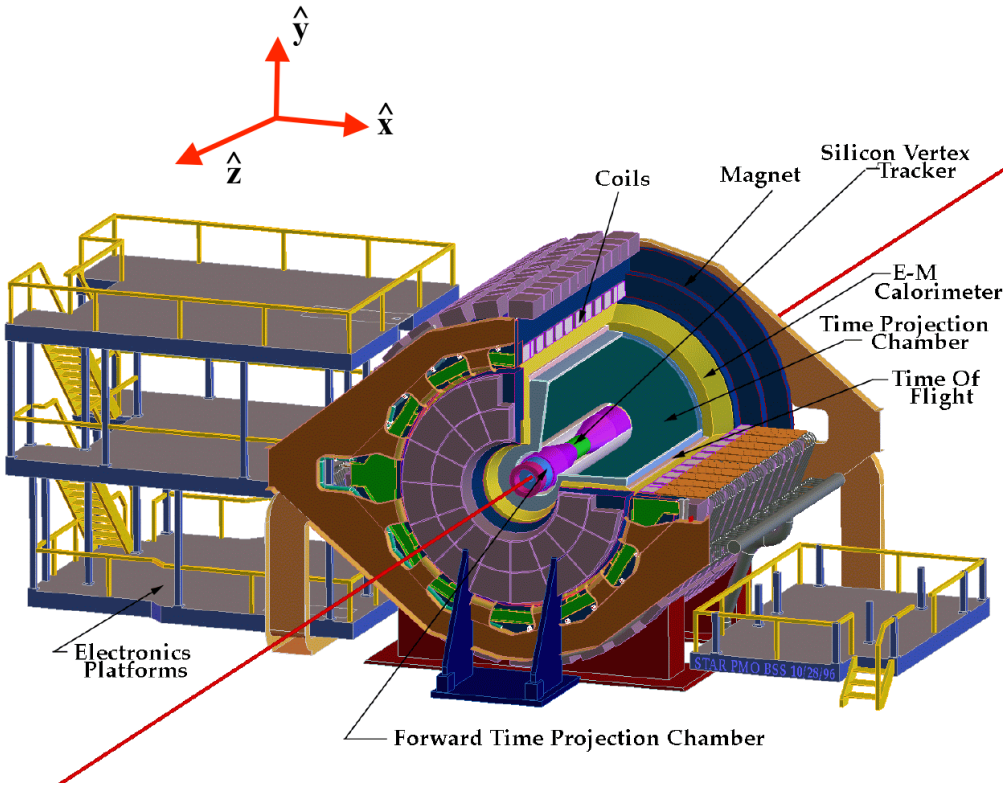

Figure 2.2: Cross sectional view and the detector components of the STAR detector.

Two accelerated beams collide near the center of the detector and produce electrically charged or neutral particles. Charged particles will move in helical tracks in the transverse plane (x-y plane) due to the presence of magnetic field. These tracks can be reconstructed by the STAR tracking system which consists of several detectors as shown in Figure 2.2. Time projection chamber (TPC), time of flight (TOF) detector, vertical position detector (VPD), silicon vertex tracker (SVT), and electro-magnetic caloriemeter (EMC) are some of the main tracking devices in the STAR detector system. The operation of these tracking devices will be briefly discussed in the next sections of this chapter.

2.2.1 Time Projection Chamber

Time Projection Chamber is the main tracking device in the STAR detector system. The TPC is located inside the full magnetic field of the STAR magnets. It is filled with a gas mixture of 90% Argon (Ar) and 10% Methane (CH_4) within a cylinder of 4 m in diameter and 4.2 m in length. The beam pipe has been built so that it passes through the center of the TPC (x = y = 0). In this geometry, the TPC is built so that it covers the full azimuthal angle ϕ ($0 < \phi < 2\pi$). Coverage of the TPC along the z direction is expressed by units of pseudo-rapidity (η) and it covers a range of, $-1 < \eta < 1$. A detailed description and introduction to η is presented in Section 2.5. Schematic view of the TPC is given in Figure 2.3.

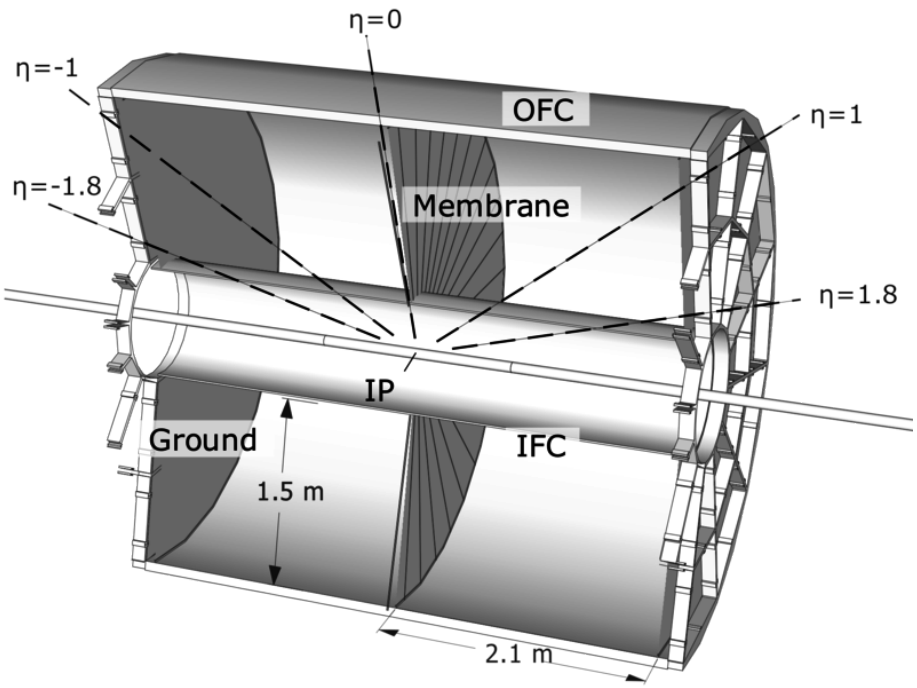

Figure 2.3: Cross sectional view of the STAR time projection chamber (TPC). Schematic shows the center membrane, inner field cage (IFC), outer field cage (OFC) and interaction point (IP). Ground stands for the ground-zero voltage. Dashed lines show the pseudo-rapidity coverage.

The TPC is divided into two halves by a central membrane at z = 0 as shown in Figure 2.3. A ground-zero electric potential is maintained at the side walls of the TPC while the center membrane is at a negative potential with respect to the side walls. As a result, a strong electric field of 130 V/cm is acting from the side walls towards the center membrane, along the z-axis. Each half of the TPC is divided into 12 equal sized sectors azimuthally, and they consist of 136,608 read-out pads in total for the precise measurement of charged-particle tracks.

2.2.1.1 Track and vertex reconstruction in TPC

When an electrically charged-particle traverses through the TPC gas, it strips out electrons from the gas molecules along the trajectory. These secondary electrons will be accelerated towards the side walls (end-caps) due to the strong electric field. Read-out pads at the end-caps record the signal from secondary electrons for the reconstruction of charged-particle tracks with the help of software. The curvature of the reconstructed helical path of a track is used to calculate the momentum of particles while the direction of the revolution of the particle is used to determine the sign of electric charge associated with the particle. With these options, the STAR TPC is capable of measuring the momentum of charged particles over a range of 0.1 to 30 GeV/c.

Reconstruction of the charged particle tracks is done using STAR tracking software. Readout pads in each sector register hits in time buckets during a collision (event). Thousands of tracks can be formed during an event. The reconstruction software looks for a set of hits that can be fitted to form a helical track. Once a track is identified, the software is capable of assigning the momentum and charge of the

particle. These identified tracks are called "global tracks". For a given event, once all the possible global tracks are identified, these trajectories are extrapolated on to the beam axis to find the position of the primary vertex (PV) where all the trajectories originated from. In an event, if the software found more than one primary vertex, then the primary vertex with highest probability (rank) is used. Global tracks that have a distance of closest approach (gDCA) less than 3 cm are labeled as primary particles and the rest as secondary particles.

Particle identification (PID) is another utility of the TPC. For PID, the ionization-energy loss per unit length of charged particles in the TPC gas is used. The amount of energy lost when a charged particle moves through the TPC gas depends on the parameters such as mass, velocity, and the electric charge of the particle. A complete description of average dE/dx for a charged particle travelling in a medium is given by the Bethe formula:

$$-\left\langle \frac{dE}{dx} \right\rangle = \frac{4\pi}{m_e c^2} \cdot \frac{nz^2}{\beta^2} \cdot \left(\frac{e^2}{4\pi\varepsilon_0} \right)^2 \cdot \left[\ln \left(\frac{2m_e c^2 \beta^2}{I \cdot (1-\beta^2)} \right) - \beta^2 \right] \tag{2.1}$$

Here, m_e and e stand for rest mass and charge of electron or any other charged particle of interest, z for charge (multiples of electron charge), n for electron number density of the medium, l for mean excitation potential, c for speed of light, ε_0 for vacuum permittivity, and $\beta = \frac{v}{c}$. By considering the dE/dx dependency on the momentum of a charged particle, the Bethe formula can be fitted to experimentally measured dE/dx and extract the information needed for the direct PID. The TPC can identify kaons, pions, and protons in a momentum range from 0.1 to 0.7 GeV/c while, protons can be directly identified against kaons and pions up to a momentum of $\sim$1 GeV/c.

As discussed earlier, the TPC helps tracking quite important physical information

of charged particles produced after the collision. They are, momentum, charge, path length, and ionization energy loss per unit length (dE/dx). In addition, each track carries information needed for the quality assurance (QA). Track and event QA is done mainly based on the number of hits associated with a certain track as identified by TPC. For instance, the number of hits assigned to a track, number of hits possible for the trajectory, and number of hits used for the dE/dx calculation can be used to identify quality tracks measured with high precision. In addition, track quality cuts are also used to further constrain the presence of impurities and increase the purity of identified particles. In addition to the cut parameters used in general QA procedure at STAR, special track cuts need to be imposed depending upon the goals of the analysis. All general and specific cut parameters used in this analysis are described in Chapter 3 of this dissertation. More information about STAR TPC and its functioning can be found in [13].

For the extended particle tracking in the very forward direction, the forward time projection chamber (FTPC) has been established. This plays an important role in tracking the charged particles produced at high track density events in Au + Au collisions. The FTPc is located in the pseudorapidity range of $2.5 < |\eta| < 4.0$ and more information about the detector geometry and functions can be found in [14].

2.2.2 Time of flight detector

Although the TPC is capable of measuring the momenta of charged-particle tracks up to 30 GeV/c, it has limited particle identification capabilities when the particle momenta is larger ($>$ 1 GeV/c). Therefore, for the particle identification at higher momenta, the STAR time of flight (TOF) detector is used. The TOF has the ability

to identify particles even at a momentum of 3 GeV/c which is about three times the upper momentum limit for PID in TPC. The TOF detector system surrounds the TPC in full azimuthal angle ϕ ($0 < \phi < 2\pi$) and covers a pseudo-rapidity range of $-0.94 < \eta < 0.94$.

The TOF consists of a trigger detector called pseudo vertex position detector (pVPD) and time-of-flight patch (TOFp) detector. There are two pVPDs located in the very forward direction ($4.43 < \eta < 5.1$) in the east and west side of STAR. A schematic of the pVPDs and TOFp in relation to the STAR TPC is shown in Figure 2.4. During a collision, photons are emitted and pVPDs are used to detect photons that travel very close to the beam pipe. The time at which these photons reach east or west pVPDs (t_{east} and t_{west}, respectively) is used to evaluate the start time (t_0) of tracks originated from a certain event. Equations 2.2 - 2.4 show the estimation of t_0 where L is the distance from pVPD to the center of the detector (z = 0), z_{vertex} is the z-coordinate of the primary vertex and c stands for the speed of light. Using the same set of equations, the z-coordinate of the primary vertex (PV_z) can also be calculated. This measurement is used to compare to the vertex position obtained from TPC for the removal of bad events.

$$t_{east} = t_0 + \frac{L + z_{\text{vertex}}}{c} \tag{2.2}$$

$$t_{\text{ west}} = t_0 + \frac{L - z_{vertex}}{c} \tag{2.3}$$

$$t_0 = \frac{t_{east} + t_{west}}{2} - \frac{L}{c} \tag{2.4}$$

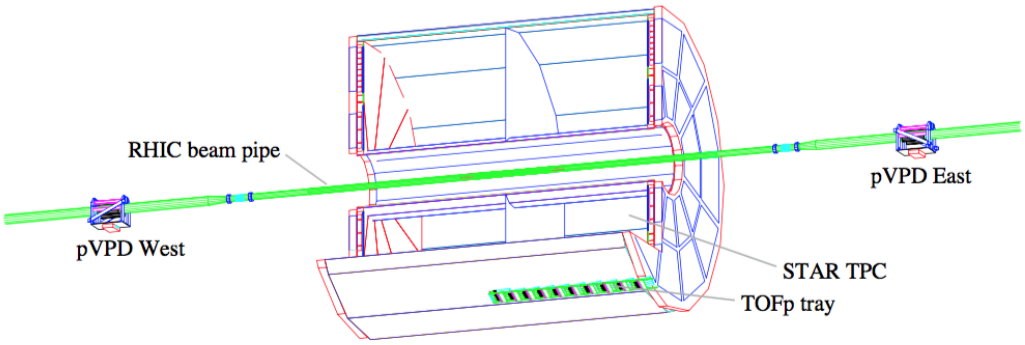

Figure 2.4: Drawing of pseudo vertex position detector (pVPD) and time-of-flight patch (TOFp) detector in relation to the STAR time projection chamber (TPC).

To measure the "stop time" (t_s), associated with a certain track, Multi-gap Resistive Plate Chambers (MRPC) are used. There are 3840 MRPCs in total which are located at the exterior of the TPC but inside the STAR magnetic field. MRPCs are capable of tracking down the signals from traversing charged particles with the help of precise fast-timing electronics. In each event, MRPCs record the stop time for tracks as well as the y-coordinate which is related to the azimuthal position ($\sim \phi$) of a certain track. With this information, time-of-flight (Δt) for a certain track can be calculated as given in Equation 2.5.

$$\Delta t = t_{\,\mathrm{s}} - t_{\,0} \tag{2.5}$$

Then the inverse velocity ($1/\beta$) of a charged particle can be calculated as

$$\frac{1}{\beta} = \frac{c\Delta t}{S} \tag{2.6}$$

Here, S is the path length of the particle which can be measured by TPC and c stands for the speed of light. Finally, the mass-squared (M^2) associated with the particle is calculated as

$$\mathrm{M}^2 = \mathrm{p}^2 \left(\frac{1}{\beta^2} - 1 \right) \tag{2.7}$$

Here, p is the momentum of the particle which can be measured in the TPC. The calculated M^2 can be used to directly identify the particle species associated with the track. The STAR TOF is capable of identifying pions and kaons up to the momentum $\sim$ 1.8 GeV and protons up to the momentum $\sim$ 3.0 GeV. More details about the operation and design of STAR TOF and pVPD can be found in [15].

2.2.3 Electro-Magnetic Calorimeter (EMC)

The STAR detector system consists of two electro-magnetic calorimeters named, barrel electro-magnetic calorimeter (BEMC) and end-cap electro-magnetic calorimeter (EEMC). Both of these detectors record the energy of the incident particles that interact via electro-magnetic interaction.

The BEMC is located outside the STAR TPC and inside the solenoidal magnet. It covers a pseudo-rapidity range of $-1.0 < \eta < 1.0$. The BEMC is capable of tracking photons, electrons, π^0, and η mesons in a large acceptance range. In addition, the BEMC contributes as a trigger detector for the high p_T physics at STAR. The BEMC is supplemented by the EEMC which covers the forward direction in the STAR detector system. The EEMC is located in the very forward rapidity range $1.0 < \eta < 2.0$ and covers the full azimuthal direction. It also plays an important role in the detection of photons, π^0, and η mesons while serving as a trigger detector for high p_T triggering system similar to the BEMC. The EEMC is capable of recording energy in the range of 10 - 40 GeV. More information about the STAR EMC system

can be found in [16].

2.2.4 Silicon Vertex Tracker (SVT)

As described in the earlier sections, The TPC and TOF both are capable of tracking only charged particles. But, the SVT uses secondary vertexing for the reconstruction of short-lived particles. Primarily strange and multi-strange baryons which decay very close to the interaction zone can be reconstructed through the SVT. Some charged particles do not reach the active volume of TPC due to the presence of the magnetic field and due to their low momentum. In these cases, the SVT helps extending the kinematic acceptance of the STAR detector system by providing capabilities for tracking of these low-momentum particles. It also improves the STAR capabilities on two-track resolution and particle identification through energy loss. More details about detector design and functioning can be found in [17].

The relative positions of TPC, TOF, EEMC, BEMC, and SVT in the STAR detector system are shown in Figure 2.5.

2.3 Rapidity and pseudo-rapidity

A special set of measurement units has been introduced in accelerator physics mainly when a measurement is taken along the direction of the beam line (z-axis). The beams travel very close to the speed of light. Therefore, the system is Lorentz boosted along the z-axis, with respect to the lab frame. As a result, measurements done should either be invariant of the frame of reference or, although they are not invariant, have transformation properties that are easy to handle. In this section,

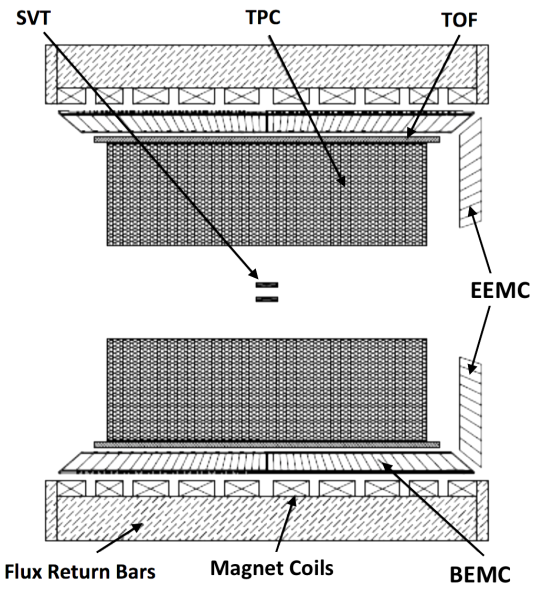

Figure 2.5: Configuration of TOF, EEMC, BEMC, and SVT in relation to the TPC in STAR detector system.

longitudinal variables called rapidity ($\mathbf{y}$[1]) and pseudo-rapidity (η) are introduced and discussed.

First, the energy-momentum relationship for a particle whose rest mass is M can be written as:

$$E^2 = p_x^2c^2 + p_y^2c^2 + p_z^2c^2 + M^2c^4 \tag{2.8}$$

Here, p_x, p_y, and p_z stand for the momentum along x, y, and z directions, respectively. c stands for the speed of light. As usual, the beam-line direction is chosen to be the z-axis. Therefore, it is assumed that the Lorentz boost occurs only with respect to the z-axis, but not with respect to x or y-axis. Now, the Lorentz transformations for the 4-displacements can be written as

[1] $\mathbf{y}$ represents rapidity and y represents y-coordinate in Cartesian coordinates.

$$ct' = \gamma(ct - \beta z) \tag{2.9}$$

$$x' = x \tag{2.10}$$

$$y' = y \tag{2.11}$$

$$z' = \gamma(z - \beta ct) \tag{2.12}$$

Here, t stands for time, $\gamma = \frac{1}{\sqrt{1-\frac{v^2}{c^2}}}$ and $\beta = \frac{v}{c}$ and x', y', z', t' stand for Lorentz transformed quantities. Similarly, for the components of the 4-momentum, the transformations can be written as

$$E'/c = \gamma\left(E/c - \beta p_z\right) \tag{2.13}$$

$$p'_x = p_x \tag{2.14}$$

$$p'_y = p_y \tag{2.15}$$

$$p'_z = \gamma\left(p_z - \beta E/c\right) \tag{2.16}$$

Here, E stands for energy and p'_x, p'_y, p'_z, and E' stands for Lorentz transformed quantities. Then, a quantity called transverse mass (M_T) is defined by considering only the collection of Lorentz-invariant momentum components and the mass component from the energy-momentum relationship associated with a particle as

$$M_T^2c^4 = p_x^2c^2 + p_y^2c^2 + M^2c^4 \tag{2.17}$$

Now, the rapidity ($\mathbf{y}$) is defined as,

$$\mathbf{y} = \frac{1}{2}\ln\left(\frac{E + p_zc}{E - p_zc}\right) \tag{2.18}$$

Rapidity is defined so that it approaches zero when the particle has no contribution to the motion along the z-axis. On the other hand, when a particle moves only along the z axis with no contributions to transverse momentum, then rapidity of that particle approaches ∞. Therefore, rapidity is related to the angle between the direction of emission of the particle and the beam axis (z-axis). Now, by considering the Equations 2.17 - 2.18, the rapidity can be re-written in terms of M_T as

$$y = \ln\left(\frac{E + p_z c}{\sqrt{E^2 - p_z^2 c^2}}\right) = \ln\left(\frac{E + p_z c}{M_T c^2}\right) \tag{2.19}$$

There are many different ways of expressing rapidity. The following description shows one other way of introducing rapidity using hyperbolic tangents

$$\tanh\theta = \left(e^{\theta} - e^{-\theta}\right) / \left(e^{\theta} + e^{-\theta}\right) \tag{2.20}$$

Now, Rapidity can be re-written as

$$\mathbf{y} = \tanh^{-1}\left(\tanh\left(\ln\left(\frac{E + p_z c}{M_T c^2}\right)\right)\right) \tag{2.21}$$

$$\mathbf{y} = \tanh^{-1}\left(\frac{\exp\left(\ln\frac{E+p_z c}{M_T c^2}\right) - \exp\left(-\ln\frac{E+p_z c}{M_T c^2}\right)}{\exp\left(\ln\frac{E+p_z c}{M_T c^2}\right) + \exp\left(-\ln\frac{E+p_z c}{M_T c^2}\right)}\right) \tag{2.22}$$

Finally it simplifies to a neat expression

$$\mathbf{y} = \tanh^{-1}\left(\frac{p_z c}{E}\right) \tag{2.23}$$

Now, for the understanding of the transformation of rapidity under the Lorentz boosting parallel to z-axis, Lorentz transformation is applied to Equation 2.18 where, $\gamma = \frac{1}{\sqrt{1-\frac{v^2}{c^2}}}$ and $\beta = \frac{v}{c}$.

$$\mathbf{y}' = \frac{1}{2}\ln\left(\frac{\gamma E/c - \beta\gamma p_z + \gamma p_z - \beta\gamma E/c}{\gamma E/c - \beta\gamma p_z - \gamma p_z + \beta\gamma E/c}\right) \tag{2.24}$$

$$\mathbf{y}' = \frac{1}{2}\ln\left(\frac{\gamma\left(E/c + p_z\right) - \beta\gamma\left(E/c + p_z\right)}{\gamma\left(E/c - p_z\right) + \beta\gamma\left(E/c - p_z\right)}\right) \tag{2.25}$$

$$\mathbf{y}' = \frac{1}{2}\ln\left(\frac{E/c + p_z}{E/c - p_z}\right)\left(\frac{\gamma - \beta\gamma}{\gamma + \beta\gamma}\right) \tag{2.26}$$

$$\mathbf{y}' = \frac{1}{2}\ln\left(\frac{E + p_z c}{E - p_z c}\right) + \ln\sqrt{\frac{1-\beta}{1+\beta}} \tag{2.27}$$

Now, $\mathbf{y}'$ can be expressed in term of $\mathbf{y}$ as

$$\mathbf{y}' = \mathbf{y} + \ln\sqrt{\frac{1-\beta}{1+\beta}} \tag{2.28}$$

Equation 2.27 can further be simplified using the following relationship

$$\ln\sqrt{\frac{1-\beta}{1+\beta}} = -\tanh^{-1}\beta \tag{2.29}$$

This proves the fact that Lorentz transformation of rapidity parallel to the z-axis gives a simple relationship as

$$\mathbf{y}' = \mathbf{y} - \tanh^{-1}\beta \tag{2.30}$$

This simple relation has an important consequence. Assume that two particles ejected after a collision have rapidity, y_1, and y_2 according to an observer. Then, suppose that another observer also measures the rapidity of the same two particles and they read as y_1' and y_2', respectively. Now, as shown in Equation 2.31 below, we can see that the difference of rapidities of two particles is independent of the Lorentz boost along the z-axis.

$$\mathbf{y}'_1 - \mathbf{y}'_2 = \left(\mathbf{y}_1 - \tanh^{-1}\beta - \left(\mathbf{y}_2 - \tanh^{-1}\beta\right)\right) = \mathbf{y}_1 - \mathbf{y}_2 \tag{2.31}$$

Therefore, in accelerator physics, rapidity plays a vital role in the measurements along the beam line direction since the difference of rapidity ($\Delta\mathbf{y}$) is not affected by the Lorentz boost of the system along the z-axis. However, when the kinematics of the particles become highly relativistic, rapidity can not be easily measured. Therefore, in such cases where the center of mass energy of the collisions are large, an approximation for the rapidity is done. This definition of rapidity at a high-momentum regime is called pseudo-rapidity (η) and it is given by:

$$\eta = -\ln\tan\frac{\theta}{2} \tag{2.32}$$

Here, θ is the angle made by the particle trajectory with the beam pipe where, $\cos\theta = p_z/p$. Pesudo-rapidity is used in most experiments based on LHC due to the extremely high collision energies they use. However, for this analysis, since the collision energies are in the range from 19.6 to 200 GeV, rapidity ($\mathbf{y}$) was used as a longitudinal position measurement of particles. Furthermore, for the determination of rapidity, it required the mass of the particle whereas pseudo-rapidity just required the emission angle.

2.4 Collision centrality

When two accelerated nuclei travel at a speed very close to the speed of light, according to the theory of relativity, it is known that the length along the direction of the motion is contracted. Therefore, the shape of two nuclei just before the collision

looks similar to two "pancakes". This can be visualized as in the schematic shown in Figure 2.6.

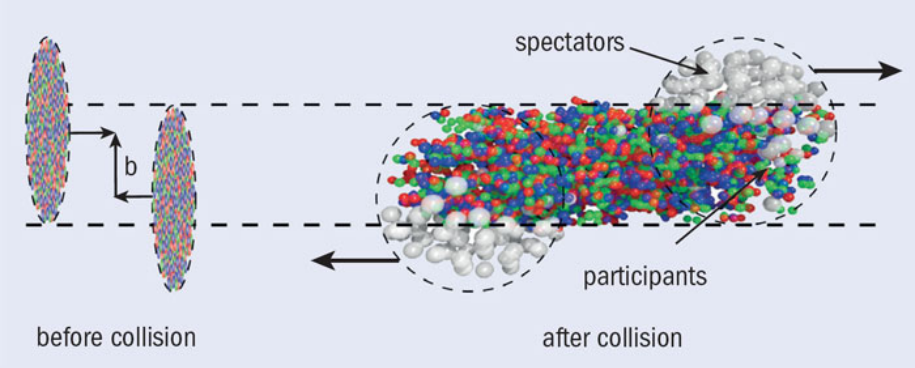

Figure 2.6: Visualization of a heavy-ion collision and the amount of overlap between two nuclei before and after the collision.

Several geometrical and experimental measurements can be introduced for the evaluation of collision centrality in heavy-ion collisions. One of them is the impact parameter (b) which is the distance between the centers of two colliding nuclei as shown in Figure 2.6. The impact parameter approaches zero as the collision centrality increases. One other parameter which can be used to represent the collision centrality is the average number of participant nucleons ($\langle N_{part} \rangle$). However, N_{part} can not be measured directly during a heavy ion collision. Therefore, alternative measurements are used for the classification of collision centrality. The total number of charged particles produced (N_{ch}) in a certain event is one of them. N_{ch} is larger in most central collisions while in peripheral collisions it becomes small. Figure 2.7 shows a histogram of the number of events occurring with a certain N_{ch} in heavy ion collisions.

For an unbiased measurement of collision centrality, the observed total number of charged particles, N_{ch}, would not be an ideal candidate due to possible auto-correlations which will be discussed in Section 3.7. Therefore, in STAR, multiplicities based on different selection criteria known as *reference multiplicities* (RefMult) are used depending on the nature of the analysis and to avoid possible auto-correlations. The selection of reference multiplicity for this analysis is discussed in Section 3.7 in detail. Finally, for the classification of centrality classes, Monte Carlo Glauber model simulations [18] are used. The Glauber model can be used to find boundaries of multiplicities for a given centrality in experimental data since the collision centrality is known via collision geometry. This analysis is done in nine centrality classes; 0-5% (most central), 5-10%, 10-20%, 20-30%, 30-40%, 40-50%, 50-60%, 60-70%, and 70-80% (most peripheral). Once the centrality classification is done, $\langle N_{part} \rangle$ is used for the representation of each centrality class. Details on the reference multiplicity definition, reference multiplicity boundaries, and $\langle N_{part} \rangle$ for each centrality class used

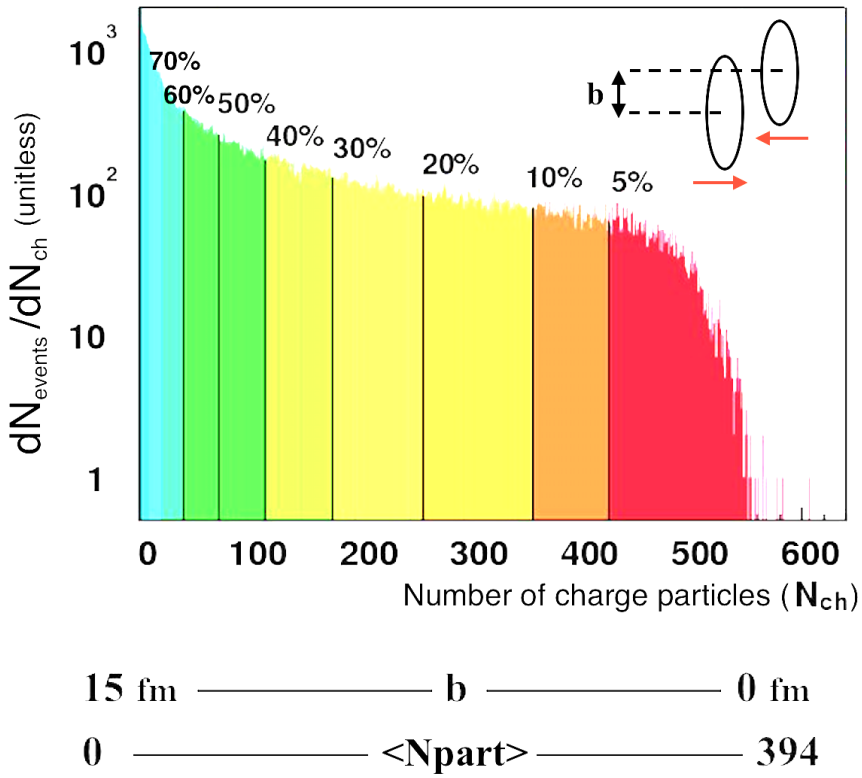

Figure 2.7: Number of events occurred (N_{events}) per number of charged particles produced in an event (N_{ch}) in Au + Au collisions and the visualization of different centrality classes with respect to N_{ch}, b, and $\langle N_{part} \rangle$.

in this analysis are given in Appendix A.1.

Chapter 3

Analysis method

Experimental techniques and analytic tools play a vital role in making precise measurements. In this chapter, all important techniques and tests done in order to achieve the aims mentioned in Chapter 1 are explained and discussed in detail. Specially, moment-calculation methods based on central moments and factorial moments are discussed together with statistical and systematic uncertainty estimation techniques. Corrections done on the results for the reconstruction efficiencies and to avoid the presence of impurities are also discussed as a part of obtaining a precise measurement of net Λ fluctuations at the STAR experiment.

3.1 Moments calculation method for net-multiplicity distributions.

This analysis is based on a counting exercise where the event-by-event net-Λ (number of Λ particles - number of $\bar{\Lambda}$ particles) value was measured and moments

of these measured net particle distributions were calculated. The moments of probability distributions are basic parameters used to describe the shape of a probability distribution. The moment and cumulant calculations are explained in this section. In this description, $N_{\Delta\Lambda}$ was used to represent the net-Λ value in a given event. The average of the net Λ value over all events is denoted by $\langle N_{\Delta\Lambda}\rangle$ and the deviation of $N_{\Delta\Lambda}$ from $\langle N_{\Delta\Lambda}\rangle$ is denoted by δN.

The well known first four moments of probability distributions are, mean (M), variance (σ^2), skewness (S), and kurtosis (κ). Cumulants of probability distributions are alternatives to moments where both are closely related. For instance, the 1^{st} order cumulant (C_1) is equal to the mean and the 2^{nd} order cumulant (C_2) is the variance (σ^2). Relationship between cumulants and moments of a probability distribution are shown in Equations 3.5 - 3.8. Cumulants up to the 4^{th} were calculated as

$$C_1 = \langle N_{\Delta\Lambda}\rangle \tag{3.1}$$

$$C_2 = \langle (\delta N)^2\rangle \tag{3.2}$$

$$C_3 = \langle (\delta N)^3\rangle \tag{3.3}$$

$$C_4 = \langle (\delta N)^4\rangle - 3\langle (\delta N)^2\rangle \tag{3.4}$$

Relationships between cumulants and moments are

$$M(Mean) = C_1 \tag{3.5}$$

$$\sigma^2(Variance) = C_2 \tag{3.6}$$

$$S(Skewness) = \frac{C_3}{C_2^{\frac{3}{2}}} \tag{3.7}$$

$$\kappa(Kurtosis) = \frac{C_4}{C_2^2} \tag{3.8}$$

With the above definitions, in this analysis, net-Λ cumulants (C_1, C_2, and C_3) and cumulant ratios ($C_2/C_1 = \sigma^2/M$ and $C_3/C_2 = S\sigma$) were calculated. Results are presented as a function of collision centrality, rapidity, and energy. In addition, factorial moments were calculated as shown in Equation 3.9 and they were used in both efficiency corrections and statistical error estimations. Factorial moments can also be used to calculate cumulants as shown in Equations 3.11 - 3.15.

$$f_{i,k}\left(n_p, n_{\overline{p}}\right) = \left\langle \frac{n_p!}{(n_p - i)!} \frac{n_{\overline{p}}!}{(n_{\overline{p}} - k)!} \right\rangle = \sum_{n_p=i}^{\infty} \sum_{n_{\bar{p}}=k}^{\infty} p\left(n_p, n_{\overline{p}}\right) \frac{n_p!}{(n_p - i)!} \frac{n_{\overline{p}}!}{(n_{\overline{p}} - k)!} \tag{3.9}$$

$$F_{i,k}\left(N_p, N_{\overline{p}}\right) = \frac{f_{i,k}\left(n_p, n_{\overline{p}}\right)}{\left(\varepsilon_p\right)^i \left(\varepsilon_{\overline{p}}\right)^k} \tag{3.10}$$

Equation 3.9 shows the expression for the calculation of raw factorial moments $f_{i,k}\left(n_p, n_{\overline{p}}\right)$ where n_p and $n_{\bar{p}}$ stand for number of observed particles (p) and anti particles ($\bar{p}$), respectively. Indices i and k stand for different indices in factorial moments. $p(n_p, n_{\overline{p}})$ represents the probability of an event with n_p number of particles and $n_{\overline{p}}$ number of anti-particles.

The lowest order factorial moments, $f_{1,0}$ and $f_{0,1}$, represent the means of particle ($\langle n_p \rangle$) and anti-particle ($\langle n_{\overline{p}} \rangle$) distributions, respectively. Equation 3.10 shows the relationship between efficiency corrected and uncorrected factorial moments where ε_p and $\varepsilon_{\overline{p}}$ stand for particle and anti-particle reconstruction efficiencies, respectively. The cumulants of net multiplicity distributions can be calculated using factorial moments as

$$N = \langle N_p \rangle + \langle N_{\overline{p}} \rangle = \frac{\langle n_p \rangle}{\varepsilon_p} + \frac{\langle n_{\overline{p}} \rangle}{\varepsilon_{\overline{p}}} \tag{3.11}$$

$$C_1 \equiv K_1 = \langle N_p \rangle - \langle N_{\overline{p}} \rangle \tag{3.12}$$

$$C_2 \equiv K_2 = N - K_1^2 + F_{02} - 2F_{11} + F_{20} \tag{3.13}$$

$$\begin{aligned} C_3 \equiv K_3 = {} & K_1 + 2K_1^3 - F_{03} - 3F_{02} + 3F_{12} + 3F_{20} - 3F_{21} + F_{30} \\ & -3K_1 \left(N + F_{02} - 2F_{11} + F_{20}\right) \end{aligned} \tag{3.14}$$

$$\begin{aligned} C_4 \equiv K_4 = {} & N - 6K_1^4 + F_{04} + 6F_{03} + 7F_{02} - 2F_{11} - 6F_{12} - 4F_{13} \\ & +7F_{20} - 6F_{21} + 6F_{22} + 6F_{30} - 4F_{31} + F_{40} \\ & +12K_1^2 \left(N + F_{02} - 2F_{11} + F_{20}\right) \\ & -3 \left(N + F_{02} - 2F_{11} + F_{30}\right) \\ & -4K_1 \left(K_1 - F_{03} - 3F_{02} + 3F_{12} + 3F_{20} - 3F_{21} + F_{30}\right) \end{aligned} \tag{3.15}$$

3.2 Data sets

Particle data produced in heavy ion (Au + Au) collisions from five different beam energies ($\sqrt{S_{NN}}$ =19.6 GeV, 27 GeV, 39 GeV, 62.4 GeV, and 200 GeV) were used in this analysis. These data belong to the 1^{st} phase of the STAR beam energy scan program (BES - I) which occurred during the years 2010 and 2011. Basic information about the data sets are given in Table 3.1 and Table 3.2.

Good run numbers were selected by looking at the distribution of average values of event and track information in each run. Run numbers outside a window of $\pm$ 3 standard deviations from the averages of track and event parameters were rejected in

Table 3.1: Data sets used in the analysis from Beam Energy Scan Phase - I (BES-I) with their statistics, year of the production and corresponding baryon-chemical potentials (μ_B) extracted from HRG model [19].

$\sqrt{s_{NN}}$ (GeV)	Statistics (M)	Year	μ_B (MeV)
19.6	$\sim$ 34	2011	205
27	$\sim$ 71	2011	155
39	$\sim$ 114	2010	115
62.4	$\sim$ 40	2010	70
200	$\sim$ 221	2011	20

the analysis. Visualization of the bad run-number identification is shown in Figure 3.1. Bad run-number percentage was highest in the 62.4 GeV data set and lowest in 39 GeV data set.

3.3 Event selection

Event-quality cuts were used for the selection of good events for the analysis. For all five energies, events with reconstructed primary vertex of less than 30 cm ($V_z < 30$ cm) were chosen for the analysis. Only the events with a radial distance to the origin (x = y = z = 0) of less than 2 cm ($V_r < 2cm$) were permitted in the analysis. At higher energies, luminosity increases and as a result, some particles from previous events could still be traversing while the detector read-out system gets triggered by a new event. To avoid these pile-up events in the analysis, the vertical position detector (VPD) was used in addition to the time-projection chamber (TPC) to locate the primary vertex. Then, events with the difference between V_z measurements from TPC and VPD less than 3 cm ($|V_z(vpd) - V_z| < 3$ cm) were used in the analysis. This additional condition was only applied to the three highest energies (39, 62.4,

Table 3.2: Production names of data produced in Au + Au collisions from 19.6 to 200 GeV beam energies in BES-I with trigger names and IDs used in the analysis.

$\sqrt{s_{NN}}$ (GeV)	Production	Trigger Name	Trigger IDs
19.6	AuAu19_Production	P11ik	340001, 340011 340021
27	AuAu27_Production_2011	P11id	360001
39	AuAu39_Production	P10ik	280001
62.4	AuAu62_Production	P10id	270001, 270011 270021
200	AuAu200_production_2011	P11id	350001, 350011 350003, 350023 350033, 350043

and 200 GeV). Some of the important event selection cuts and number of events chosen for the analysis are shown in Figures 3.2, 3.3, 3.4, and 3.5.

3.4 Track selection

The reconstruction of the primary Λ ($\bar{\Lambda}$) particles should be done using secondary protons - p ($\bar{p}$) and pions - π^- (π^+). For the identification of the possible secondary daughter particles, the STAR TPC was used. Ionization-energy loss in the TPC gas was used to identify these charged particles as explained in Section 2.2.1.1. To maintain a higher purity in the particle identification procedure, several important cuts were imposed. Only the tracks that had at least 15 hit points out of a maximum of 45 were permitted in the analysis as shown in Figure 3.6(a). To avoid the multiple counting of split tracks, the number of reconstructed hits was requied to be at least

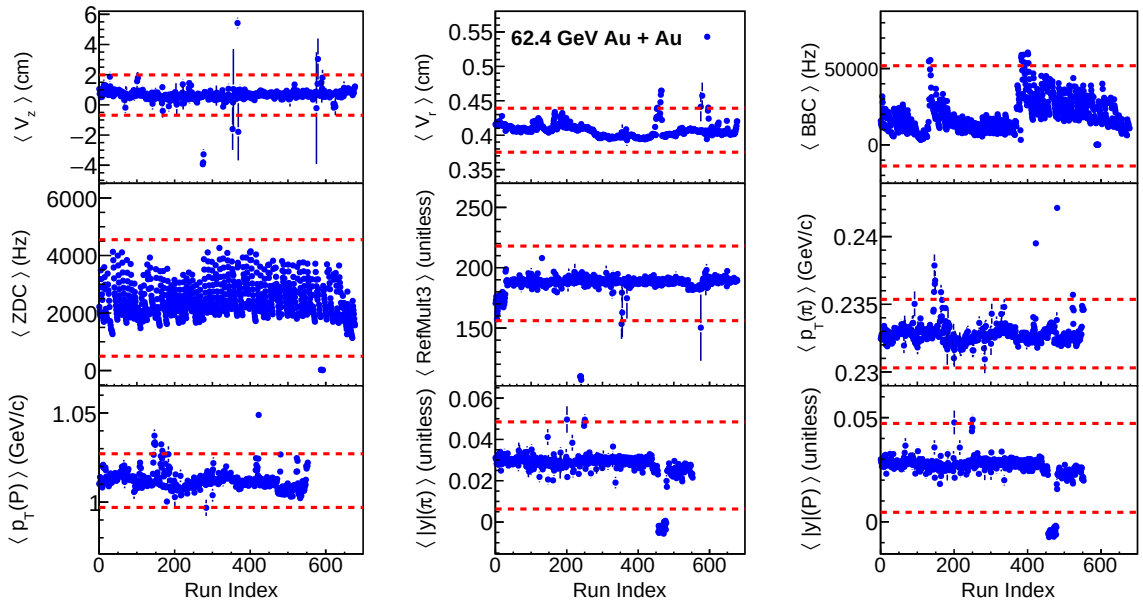

Figure 3.1: Visualization of run index outliers in 62.4 GeV Au + Au data set. Blue points shows the calculated average of each parameter in each run index. Red dashed lines show the 3 standard deviations (3σ) boundaries.

52% of the total possible fit points (nHitsFit/NFitPoss $>$ 0.52). The minimum number of points required to derive the corresponding ionization energy loss per unit length (dE/dx) was limited to 5. In Figure 3.6(b), dE/dx of charged particles (protons - p, pions - π, kaons - k and deuterium - d) are shown as a function of momentum in 200 GeV Au + Au collisions.

The global distance of closest approach (gDCA) is one of the important parameters used to distinguish between primary and secondary particles. Since the reconstructed trajectories of secondary particles should not point to the primary vertex, a lower limit for the gDCA cut was imposed on both protons and pions. These cuts are further explained in the next section (V^0 reconstruction) and all the track quality cuts used are listed in Table 3.4.

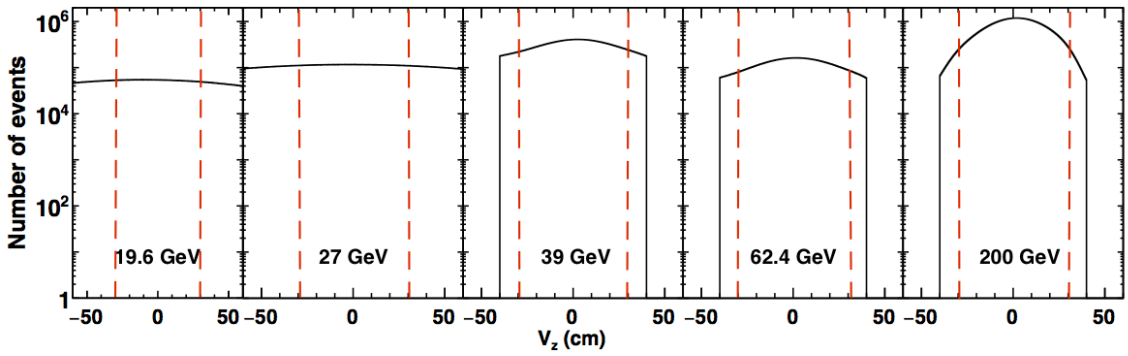

Figure 3.2: Number of events per z-coordinate of the primary vertex (V_z) for five beam energies from 19.6 to 200 GeV Au + Au collisions at STAR. Red dashed lines show the V_z cuts ($|V_z| < 30$ cm) used in the analysis.

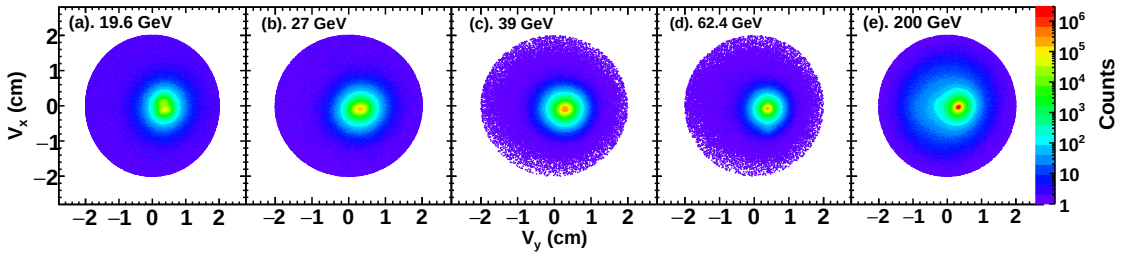

Figure 3.3: Distribution of the x and y coordinates of the primary vertices (V_x and V_y) for five beam energies from 19.6 to 200 GeV Au + Au collisions at STAR. $\sqrt{V_x^2 + V_y^2}$ (V_r) < 2 cm cut was used in the analysis.

3.5 V^0 reconstruction

Neutral particles such as the Λ baryon can not be identified directly in the TPC since they do not deflect in the presence of an external magnetic field. Therefore, extraction of Λ yields was done by reconstructing the decay vertex (V^0). Λ ($\bar{\Lambda}$) baryon has a decay channel, Λ ($\bar{\Lambda}$) $\rightarrow p$ ($\bar{p}$) + π^- (π^+) , with a branching ratio of (63.9 $\pm$ 0.5) % [20]. Both the decay daughters, protons, and pions, were identified using the TPC and the decay topology is shown in Figure 3.8.

Equations 3.17 - 3.19 show the calculation of invariant mass, (M_{P,π^-}) of the mother particle from the properties of identified daughter particles by considering the

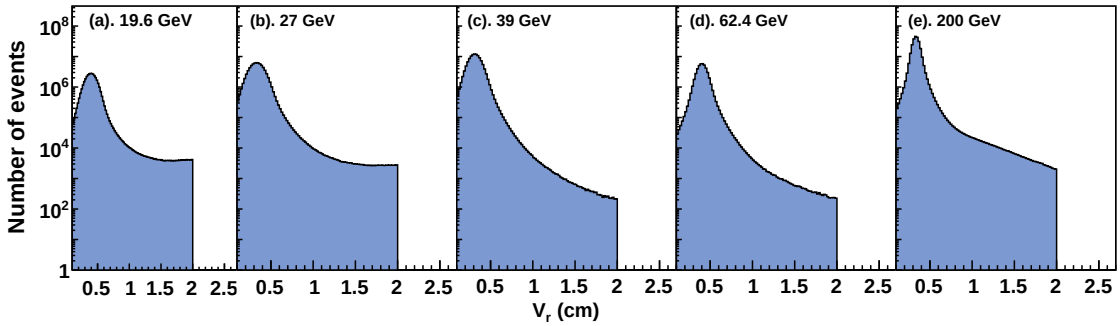

Figure 3.4: Number of events per radial coordinate of the primary vertex (V_r) for five beam energies from 19.6 to 200 GeV Au + Au collisions at STAR. $|V_r| < 2$ cm cut was used in the analysis.

conservation of 4-momentum. Here, $E_{p(\pi^-)}$ and $p_{p(\pi^-)}$ are the energy and momentum of proton (pion), respectively. Note, for a given particle species x, $\overrightarrow{p}_x$ represents the three-momentum and p_x represents four-momentum. The speed of light is considered to be equal to unity.

$$\Lambda \rightarrow p + \pi^- \tag{3.16}$$

$$p_\Lambda = p_p + p_{\pi^-} \tag{3.17}$$

$$-M^2_{p,\pi^-} = (p_p + p_{\pi^-})^2 \tag{3.18}$$

$$-M^2_{p,\pi^-} = M^2_p + M^2_{\pi^-} + 2(E_p E_{\pi^-} - \overrightarrow{p}_p . \overrightarrow{p}_{\pi^-}) \tag{3.19}$$

The calculated invariant mass distribution from all measured proton and pion pairs from 39 GeV Au + Au collisions is shown in Figure 3.7. Initially, all identified proton and pion pairs were considered for calculation of invariant mass, independent of whether they come from a primary Λ decay or not. This histogram should be peaked at the rest mass of Λ baryon which is 1115.68 $\pm$ 0.006 MeV/c^2 [20] due to the conservation of energy and momentum. Protons and pions which did not come from a Λ decay reconstruct in to a mass different than the Λ rest mass. Therefore, a large background can be seen in Figure 3.7.

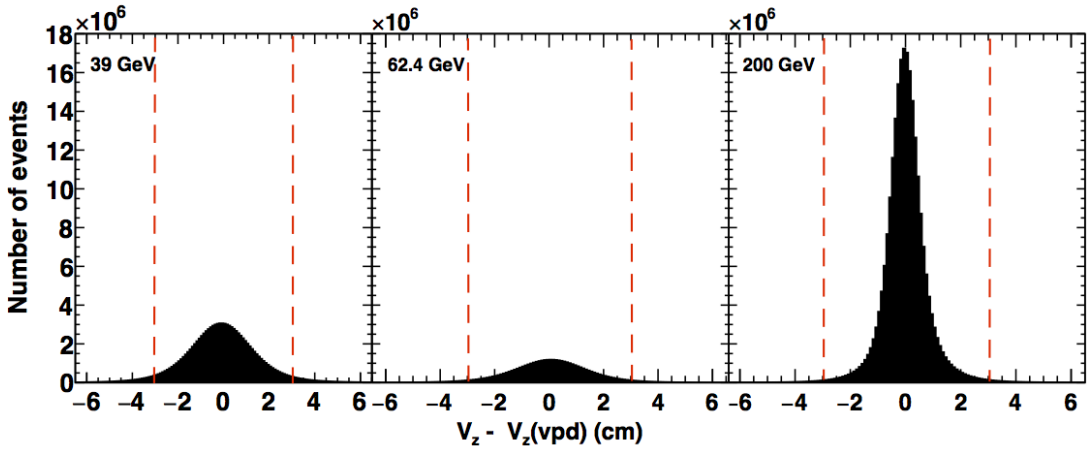

Figure 3.5: Number of events per difference between z-coordinate of the reconstructed primary vertex (V_z) from TPC and the z-coordinate of the primary vertex from VPD ($V_{z(vpd)}$), for five beam energies from 19.6 to 200 GeV Au + Au collisions at STAR. Red dashed lines show the cut boundary ($|V_z - V_{z(vpd)}| < 3$ cm)

For the net-Λ fluctuation measurement, counting of Λ and $\bar{\Lambda}$ should be done on an event-by-event basis. The number of Λs or $\bar{\Lambda}$s in all events can be counted by integrating the peaked area above the background as shown in Figure 3.7. In order to enhance the purity of the analyzed sample, first, most of the background was eliminated by applying a mass cut considering the invariant mass of the Λ baryon. In each event, an invariant mass cut of $1.11 < m^{inv}_{p,\pi^-}\ (GeV/c^2) < 1.12$ was imposed. But inside this mass window, there is no established technique to distinguish between signal and background on an event-by-event basis. Therefore, topological parameters associated with the decay geometry were optimized in order to extract a signal with high purity.

There are several geometrical measurements associated with the V^0 decay, as shown in Figure 3.8. When a charged particle traverses in the presence of an applied magnetic field, it follows a helical path in the transverse plane (x-y plane). The curvature of these tracks depends on how much momentum is carried by the

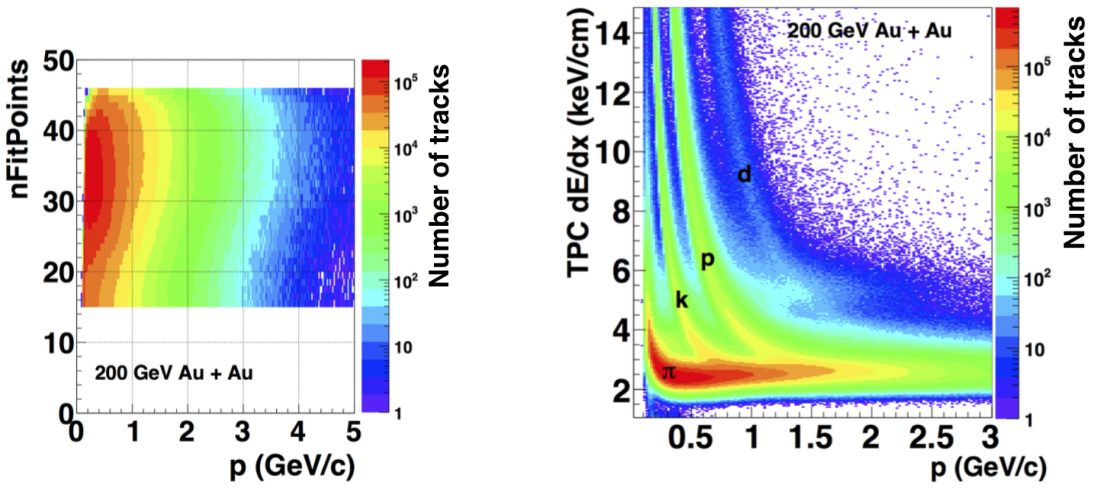

(a) (b)

Figure 3.6: (a): Visualization of nFitPionts in TPC as a function of momentum for 200 GeV Au + Au data set. Color palette represents the number of tracks. (b): Ionization energy loss per unit length (dE/dx) for different particle species (π - pions, k - kaons, p - protons, d - deuterium) as a function of momentum in 200 GeV Au + Au collisions as measured by the STAR TPC. Color palette represents the number of tracks.

corresponding particle. Once the tracks are reconstructed using TPC, geometrical parameters associated with the decay topology were calculated. These geometrical parameters are listed below and illustrated in Figure 3.8.

1. **Distance of closest approach (DCA) of V^0 to the primary vertex (PV)**. This distance should be zero for the ideal case but it is given an upper bound to account for the experimental resolution.

2. **DCA of proton to PV**. Since the reconstruction of the V^0 is done using the secondary protons, this distance should be large enough to prevent the presence of primaries. Therefore a lower bound was imposed on this measurement.

3. **DCA of pion to PV**. Similar to the DCA of proton to PV, a lower bound was imposed on this distance to prevent the contamination from primary pions.

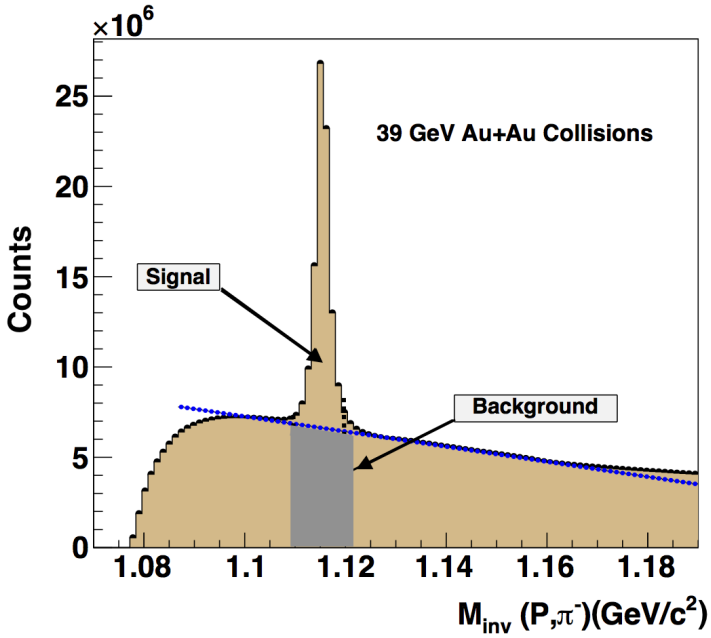

Figure 3.7: Signal and background in the reconstructed invariant mass distribution using proton (p) and pion (π^-) pairs from 39 GeV Au + Au collisions. The blue dashed line shows the fitted first order polynomial to the background surface.

4. DCA of proton to pion. In the ideal situation, this distance should be zero since the decay product should emit from the same decay vertex. But it was given a window with an upper bound, to account for the possible experimental uncertainties.

5. Decay length (L). The mean-path length ($c\tau$) for Λ baryon is 7.86 cm, which means that about 50% of the Λs have decayed after that distance assuming they travel at the speed of light (c). Therefore, a lower bound was imposed on the decay length.

Exact topological cuts imposed on the V^0s and on the decay daughters are listed in Table 3.4.

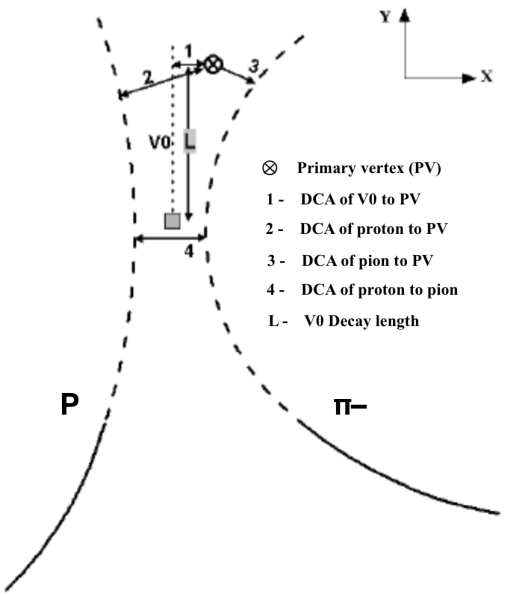

Figure 3.8: Cross section of V^0 decay topology in x-y plane. All the topological parameters used in the analysis are marked by numbers from 1 to 4 and V_0 decay length is represented by L.

3.6 Purity of V^0 samples

As mentioned in the previous section, various topological cuts can be used to refine the most probable V^0 candidates in the sample. Optimization of the topological cuts was done by using variations of different topological cut combinations and calculating the purity of the resulting V^0 samples.

For the extraction of the signal, firstly, the number of entries in the signal and background areas of the invariant mass distribution were counted. A first order polynomial fit was used to identify the background shape as shown by the blue dashed line in Figure 3.7. With the help of the background fit function, the area below the signal was estimated. Then the calculated signal to background and signal ratio (Equation 3.21) was used as the measure of the purity of the sample. Five sets of different topological cut sets were used in this analysis as shown in Table 3.3.

These cut-set variations were done starting with wide topological cuts (cut set - 5) and making them narrower and finally ending with the most strict cut set (cut set - 1). In each step, measures of purity were calculated as

$$\frac{S}{B} = \frac{Signal}{Background} \tag{3.20}$$

$$Purity = \frac{Signal}{(Signal + Background)} \times 100\% \tag{3.21}$$

Table 3.3: Purity of the V^0 candidates in different topological cut selections for 39 GeV Au + Au collisions. These results are based on 1 million minimum-biased events.

Parameter	cut set - 1	cut set - 2	cut set - 3	cut set - 4	cut set - 5
DCA (V^0 to PV)	< 0.35	< 0.5	< 0.65	< 0.8	< 0.95
DCA (p to PV)	> 0.6	> 0.5	> 0.4	> 0.3	> 0.2
DCA (π to PV)	> 1.75	> 1.5	> 1.25	> 1.0	> 0.75
DCA (p to π)	< 0.5	< 0.6	< 0.7	< 0.8	< 0.9
Background	3196	8608	22908	34184	82161
Signal	108654	160737	196537	213468	253431
S/B	33.00	18.67	8.58	6.24	3.08
Purity	97.14%	94.92%	89.56%	86.20%	75.52%

As seen in the Table 3.3 and Figure 3.9, the purity of the sample heavily depends on the topological cuts used. When a strict cut set (cut set -1) was used, the purity of the sample dramatically increased. But a portion of the signal was also lost at the same time. Corrections for this loss of the signal was addressed in the analysis during the efficiency correction and will be explained in Section 3.11. For this analysis, "cut set - 2" was selected which has a purity level of greater than 90%. The selection of this topological cut set was done by considering not only the purity but also the resulting reconstruction efficiency. The requirement that the efficiency should not

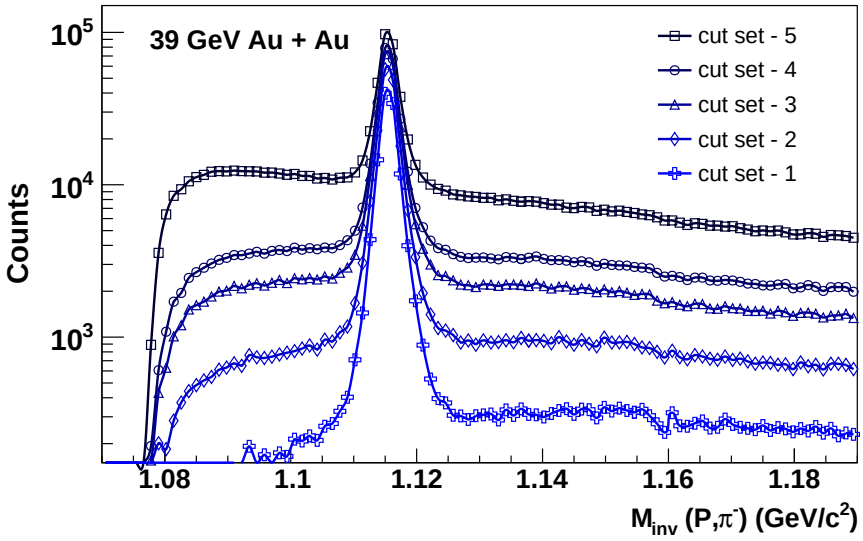

Figure 3.9: Number of reconstructed V^0s (from p, π^-) in each invariant mass bin for five cut set variations as explained in Table 3.3. These results are based on 1 million minimum bias events of 39 GeV Au + Au collisions.

drop below the 10% level to prevent the efficiency corrected distributions becoming totally Poisson was considered in the cut optimization. All the track-cut sets used in this analysis are listed in Table 3.4. Invariant mass distributions obtained with the optimized cut sets are shown in Figure 3.10 for all energies from 19.6 to 200 GeV. The transverse momentum and rapidity of reconstructed V^0s in the 200 GeV Au + Au collisions are shown in Figure 3.11.

3.7 Selection of collision centrality

Collision centrality is an important parameter in analyzing the medium produced in heavy ion collisions. Centrality can be represented by different parameters such as number of participating nuclei (N_{part}), number of binary collisions (N_{col}), and impact parameter (b). But these parameters can not be directly measured. So, the collision

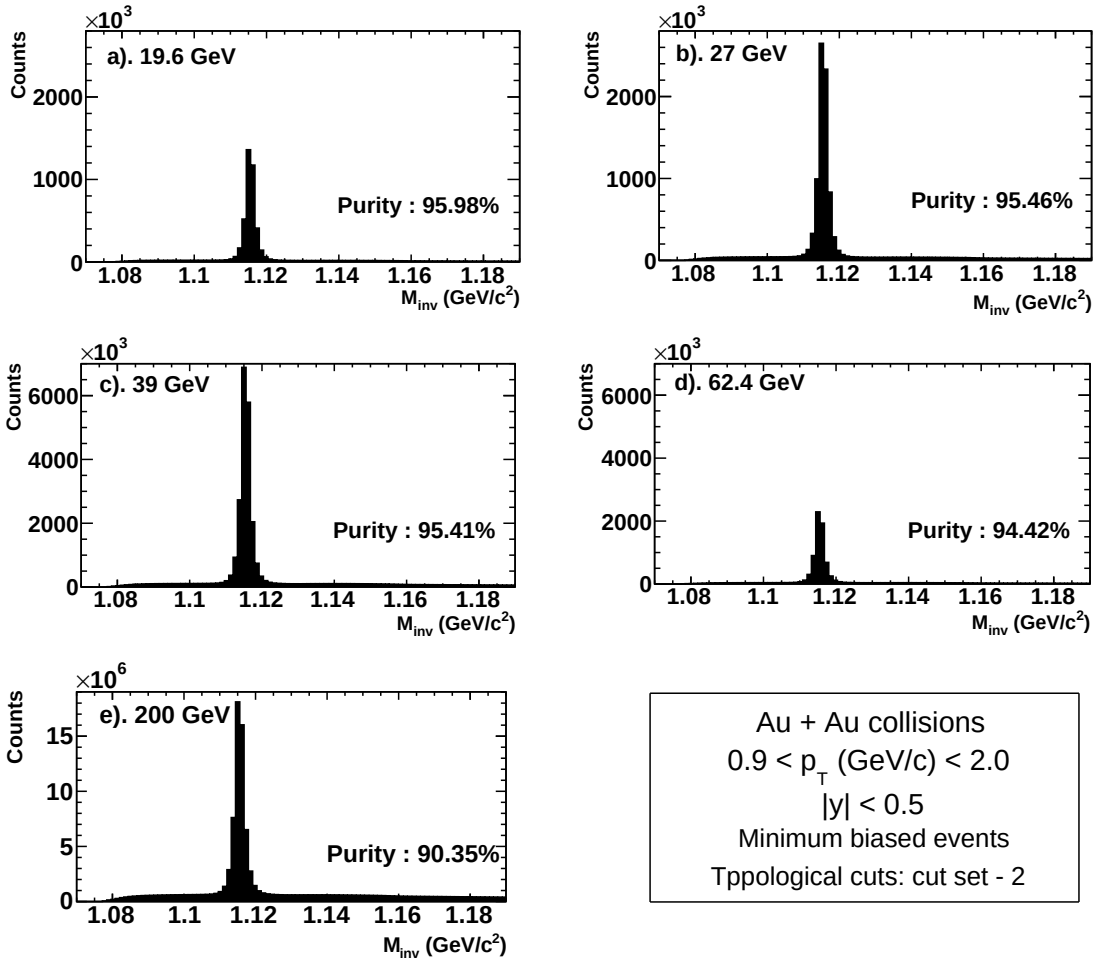

Figure 3.10: Invariant mass distributions of reconstructed V^0 for five collision energies from 19.6 to 200 GeV after the optimized cut sets were used in order to achieve a purity greater than 90%.

centrality is deduced by using a combination of experimental measurements and Monte-Carlo simulations. As explained in Section 2.4 of this dissertation, in STAR experiment, charged particle multiplicity measured by TPC and TOF detectors which is also known as reference multiplicity were used for the centrality determination.

There are different types of reference multiplicities available from the previous fluctuation analysis. These existing definitions were examined for any possibility of using one of them in this analysis. When selecting a proper centrality definition, it is

Table 3.4: Track and V^0 selection criteria used in this analysis.

Particle	Cut parameter	Cut boundary
Proton	Transverse momentum	$p_T\ (GeV/c) > 0.05$
	Rapidity	$\|y\| < 1.0$
	nFitPoints	> 15
	nHitsFit/NFitPoss	> 0.52
	PID	$n\sigma < 2.0$
	DCA to PV	> 0.5cm
	DCA to π	< 0.6cm
Pion	Transverse momentum	$p_T\ (GeV/c) > 0.05$
	Rapidity	$\|y\| < 1.0$
	nFitPoints	> 15
	nHitsFit/NFitPoss	> 0.52
	PID	$n\sigma < 2.0$
	DCA to PV	> 1.5cm
	DCA to P	< 0.6cm
V^0	Transeverse momentum	$0.9 < p_T\ (GeV/c) < 2.0$
	Rapidity	$\|y\| < 0.5$
	DCA to PV	< 0.5cm
	Decay length	> 3.0cm
	Pointing away from PV	$(\mathbf{r}_{v0} - \mathbf{r}_{pv})\,.\mathbf{p}_{v0} > 0$

important to make sure that it does not include secondary protons or pions to avoid possible auto-correlations. To partially fulfill this requirement, the reference multiplicity definition used in the net-proton analysis (RefMult3) was selected which does not include protons [21]. However, RefMult3 used primary pions in the definition and it was necessary to determine the effect of the presence of pions in this centrality definition.

For this test, first the number of pions used in the reconstruction of Λ baryon was counted in each event and the number of pions used in the RefMult3 centrality definition was counted. In the RefMult3 definition, pions with global distance of closest approach less than 3 cm (gDCA < 3.0 cm) were used. Pions used in this analysis

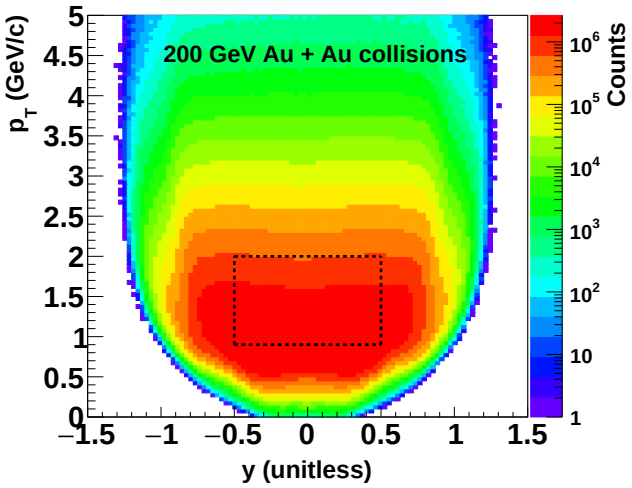

Figure 3.11: Transverse momentum (p_T) and rapidity (y) distributions of reconstructed V^0s for 200 GeV Au + Au collisions. A transverse momentum cut of $0.9 < p_T(GeV/c) < 2.0$ and a rapidity cut of $|y| < 0.5$ was used and cut boundaries are represented by dashed lines.

have a gDCA $>$ 1.5 cm and they also have an additional DCA to proton cut ($<$ 0.6 cm). These cuts limit the number of primary pions used for reconstruction of V^0s. This makes the number of pions used in the reconstruction of V^0s and also used for the centrality definition (RefMult3) small. To investigate this effect in detail, RefMult3A distributions were examined for all five energies from 19.6 to 200 GeV. The RefMult3A quantity was calculated by subtracting one count from RefMult3 whenever there was a pion which agrees with the conditions used in RefMult3 classification and also passed all the track cuts used in this analysis. In Figure 3.12, it is clear that reference multiplicities (RefMult3 and RefMult3A) are almost identical. This justifies the use of ReMult3 for the centrality determination in this analysis. Net-Λ distributions were studied in nine collision centralities and more details about the centrality classification was explained in Section 2.4 of this dissertation.

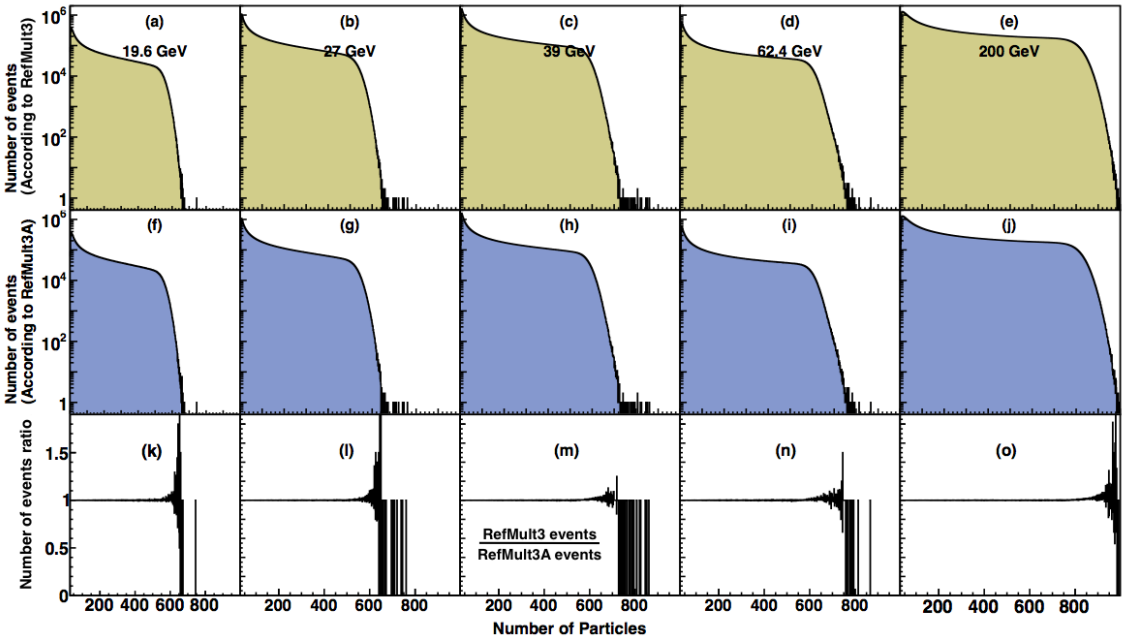

Figure 3.12: Number of events with RefMult3 condition, RefMult3A condition and their ratio for five beam energies from 19.6 to 200 GeV.

3.8 Net-Λ distributions.

After the V^0 reconstruction was done and the centrality definition was established, transverse momentum (p_T) spectra for Λ and $\bar{\Lambda}$ were obtained. Figure 3.13 shows the p_T spectra of Λ and $\bar{\Lambda}$ in nine centrality bins from 39 GeV Au + Au collisions at STAR. These results were not corrected for reconstruction efficiency or feed-down contributions. In most central collisions, V^0 production was enhanced compared to peripheral collisions. For any given centrality, p_T spectrum peaked near $\sim$ 1 GeV/c and fell as a function of increasing p_T. Based on the p_T spectra, a p_T range of 0.9 GeV/c to 2.0 GeV/c was selected for the analysis where the spectrum is approximately exponential and also reconstruction efficiency is greater than $\sim$ 10%.

After the V^0 reconstruction, the event-by-event net-Λ value was found. Net-Λ distributions for five beam energies at RHIC, as measured by STAR detector, are

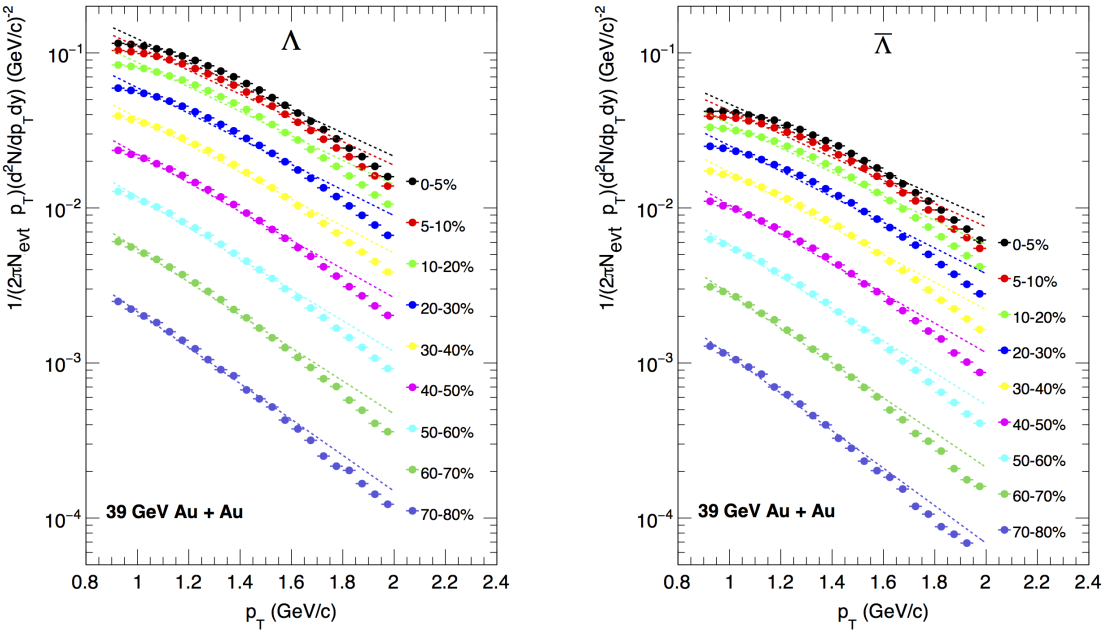

(a) (b)

Figure 3.13: Normalized p_T spectra of (a).Λ and (b).$\bar{\Lambda}$ in different collision centralities and in rapidity window, $|y| < 0.5$ from 39 GeV Au + Au collisions at STAR. Dashed lines represent an exponential fit ($p_0 e^{-1/p_T}$, where p_0 is a free parameter). Results were not corrected for reconstruction efficiency or feed-down contribution. N_{evt} represents the number of events.

shown in Figure 3.14. These results were not corrected for reconstruction efficiency or feed-down contribution. The results are presented in two collision centralities, 0-5% most central collisions and 60-70% peripheral collisions. In all energies, the width of the net-Λ distributions for most central collisions was larger than that of peripheral collisions. When going from low energy to higher energy, specifically, the distributions in most central collisions tended to be symmetric near zero.

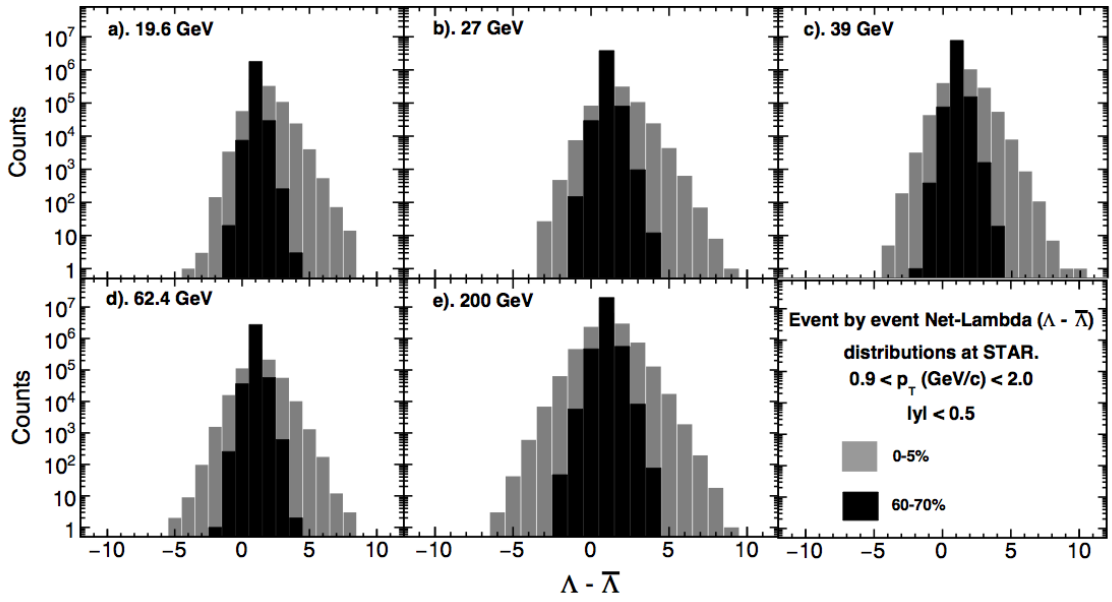

Figure 3.14: Event-by-event net-Λ distributions (Λ - $\overline{\Lambda}$) for five beam energies from 19.6 GeV to 200 GeV as measured by the STAR detector in most central (0-5%) and peripheral (60-70%) collisions. Results were not corrected for reconstruction efficiency.

3.9 Statistical uncertainty estimation.

The statistical uncertainty estimation for this analysis was done by using the error propagation explained in [22] following the Delta theorem [23]. The Delta theorem is a well known theorem in statistics, which was used to approximate the distribution of a transformation of a statistic in large samples if we can approximate the distribution of the statistic itself. Error propagation was implemented by using the co-variance matrix for Λ and $\bar{\Lambda}$ and also by taking the reconstruction efficiency into account. The co-variance matrix was calculated as shown in Equation 3.22.

$$Cov\left(f_{r,s},f_{u,v}\right)=\frac{1}{n}\Bigg[\sum_{i=0}^{r}\sum_{j=0}^{s}\sum_{k=0}^{u}\sum_{h=0}^{v}\sum_{\alpha=0}^{i+k}\sum_{\beta=0}^{i+k}\sum_{\beta=0}^{i+k}s_1(r,i)s_1(s,j)$$
$$\times s_1(u,k)s_1(v,h)s_2(i+k,\alpha)s_2(j+h,\beta)f_{\alpha,\beta}-f_{r,s}f_{u,v}\Bigg] \tag{3.22}$$

In Equation 3.22, $s_1(n,i)$ and $s_2(n,i)$ represent the Stirling numbers of first and second kind and they were calculated as in Equations 3.23 and 3.24.

$$s_1(n,i)=s_1(n-1,i-1)-(n-1)\times s_1(n-1,i) \tag{3.23}$$

with the conditions, $s_1\left(n,i\right)\big|_{n<i}=0,\quad s_1\left(n,i\right)\big|_{n=i}=1,\quad s_1\left(n,0\right)\big|_{n>0}=0$

$$s_2(n,i)=s_2(n-1,i-1)+i\times s_2(n-1,i) \tag{3.24}$$

with the conditions, $s_2\left(n,i\right)\big|_{n<i}=0,\quad s_2\left(n,i\right)\big|_{n=i}=1,\quad s_2\left(n,0\right)\big|_{n>0}=0$

The variance of a statistic quantity $\Phi\left(N_p-N_{\overline{p}}\right)$ of an event-by-event net particle distribution, $V\left(\Phi\left(N_p-N_{\overline{p}}\right)\right)$ can be expressed in terms of the co-variance, $\mathrm{Cov}(f_{i,j},f_{u,v})$ as:

$$V\left(\Phi\left(N_p-N_{\overline{p}}\right)\right)=\frac{1}{n}\sum_{i,j=0}^{H}\sum_{u,v=0}^{H}\frac{D_{i,j}D_{u,v}}{\varepsilon_p^{i+u}\varepsilon_{\overline{p}}^{j+v}}\left(f_{(i,u),(j,v)}-f_{i,j}f_{u,v}\right) \tag{3.25}$$

Here, n is the number of events and $D_{i,j},\ D_{u,v}$ are the differential coefficients which can be calculated as

$$D_{i,j}=\sum_{r=1}^{H}\sum_{s,t=0}^{H}\left(\frac{\partial\Phi}{\partial\mu_r}\frac{\partial\mu_r}{\partial m_{s,t}}\frac{\partial m_{s,t}}{\partial F_{i,j}}\right) \tag{3.26}$$

$$D_{u,v}=\sum_{r=1}^{H}\sum_{s,t=0}^{H}\left(\frac{\partial\Phi}{\partial\mu_r}\frac{\partial\mu_r}{\partial m_{s,t}}\frac{\partial m_{s,t}}{\partial F_{u,v}}\right) \tag{3.27}$$

Here, m_r and μ_r represent the multivariate and central moments, respectively. For a multivariate random vector X = (X_1, X_2, ... , X_k) and set of numbers r = (r_1, r_2, ... , r_k), these quantities were calculated as

$$m_r(\boldsymbol{X}) = E\left[\prod_{i=1}^{k} X_i^{r_i}\right] \tag{3.28}$$

$$\mu_r(\boldsymbol{X}) = E\left[\prod_{i=1}^{k} \left(X_i - E\left[X_i\right]\right)^{r_i}\right] \tag{3.29}$$

Here, E denotes the expectation value operator. With these definitions, the statistical uncertainty in the mean was calculated as

$$\sigma\left(M = \langle N_p - N_{\overline{p}}\rangle\right) = \sqrt{V(M)} = \frac{1}{\varepsilon}\frac{\sqrt{V\left(n_p - n_{\overline{p}}\right)}}{\sqrt{n}} = \frac{1}{\varepsilon}\frac{\sigma\left(n_p - n_{\overline{p}}\right)}{\sqrt{n}} \tag{3.30}$$

The statistical uncertainty in the variance was calculated as

$$\sigma\left(\sigma^2\left(N_p - N_{\overline{p}}\right)\right) = \frac{1}{\sqrt{n}}\sqrt{\left(\frac{A}{\varepsilon^4} + \frac{B}{\varepsilon^3} + \frac{C}{\varepsilon^2}\right)} \tag{3.31}$$

A, B, and C were calculated as

$$\begin{aligned} A = {} & 2f_{0,2} - f_{0,2}^2 - f_{2,0}^2 + 4f_{0,3} + f_{0,4} - 4\left(-f_{0,2}f_{1,1} + 2f_{1,2} + f_{1,3}\right) \\ & +2f_{2,0} + 2\left(f_{2,2} - f_{0,2}f_{2,0}\right) + 4\left(-f_{1,1}^2 + f_{1,2} + f_{1,2} + f_{2,1} + f_{2,2}\right) \\ & +4f_{3,0} - 4\left(-f_{1,1}f_{2,0} + 2f_{2,1} + f_{3,1}\right) + f_{4,0} \end{aligned} \tag{3.32}$$

$$\begin{aligned} B = {} & 2(2M+1)\left(-f_{0,1}f_{0,2} + 2f_{0,2} + f_{0,3}\right) + 2(1-2M)\left(f_{1,2} - f_{0,2}f_{1,0}\right) \\ & -4(2M+1)\left(-f_{0,1}f_{1,1} + f_{1,1} + f_{1,2}\right) + 2(2M+1)\left(f_{2,1} - f_{0,1}f_{2,0}\right) \\ & -4(1-2M)\left(-f_{1,0}f_{1,1} + f_{1,1} + f_{2,1}\right) + 2(1-2M)\left(-f_{1,0}f_{2,0} + 2f_{2,0} + f_{3,0}\right) \end{aligned} \tag{3.33}$$

$$C = (2M+1)^2\left(-f_{0,1}^2 + f_{0,1} + f_{0,2}\right) + 2(1-2M)(2M+1)\left(f_{1,1} - f_{0,1}f_{1,0}\right) + (1-2M)^2\left(-f_{1,0}^2 + f_{1,0} + f_{2,0}\right) \tag{3.34}$$

The statistical uncertainty in C_3 was calculated as

$$\sigma\left(C_3\left(N_p - N_{\overline{p}}\right)\right) = \sqrt{\sum_{r,s=0}^{3}\sum_{u,v=0}^{3}\frac{D_{r,s}}{\varepsilon_p^{r+s}}\frac{D_{u,v}}{\varepsilon_{\overline{p}}^{u+v}}\,\mathrm{Cov}\left(f_{r,s}, f_{u,v}\right)} \tag{3.35}$$

and, the differential coefficients can be calculated as

$$D_{i,j} = \frac{d\mu_3}{dF_{i,j}} \tag{3.36}$$

The statistical uncertainty in C_2/C_1 (σ^2/M) was calculated assuming no correlations between C_2 and C_1. But for C_3/C_2 $(S\sigma)$, correlations between C_3 and C_2 were taken into account and the statistical uncertainty was calculated as

$$\sigma\left(S\sigma\left(N_p - N_{\overline{p}}\right)\right) = \sqrt{\sum_{r,s=0}^{3}\sum_{u,v=0}^{3}\frac{D_{r,s}}{\varepsilon_p^{r+s}}\frac{D_{u,v}}{\varepsilon_{\overline{p}}^{u+v}}\,\mathrm{Cov}\left(f_{r,s}, f_{u,v}\right)} \tag{3.37}$$

and, the differential coefficients can be calculated as

$$D_{i,j} = \frac{d\left(\mu_4 - 3\mu_2^2\right)}{dF_{i,j}} = \frac{d\mu_4}{dF_{i,j}} - 6\mu_2\frac{d\mu_2}{dF_{i,j}} \tag{3.38}$$

All simplified differential coefficients $(D_{i,j})$ needed in the statistical error estimation of cumulants and cumulant ratios up to the 4^{th} order can be found in [22] and they were used in these calculations. Absolute statistical uncertainties of net-Λ cumulants and cumulant ratios are presented in Appendix A.2 - A.6.

3.10 Volume fluctuation effects.

In heavy ion collisions at STAR, collision centrality can not be measured directly, thus, it is determined by comparing the produced particle multiplicities to Glauber model simulations. This approach potentially can cause two known effects; a centrality bin-width effect (CBWE) and a centrality-resolution effect (CRE).

When presenting the higher order cumulants of net particle multiplicity distributions, wider centrality bins were used such as, 0-5%, 5-10%, 10-20% up to 70-80% for better statistical accuracy. But the variations in finite centrality bin width can cause effects on the final results. To eliminate the CBWE, centrality bin-with correction (CBWC) was used in the calculation of various cumulants of net particle multiplicity distributions as shown in the Equation 3.39, where X represents a given moment, index i runs over each fine centrality bin, n_i is the number of events in the i^{th}, bin and $\sum n_i$ is the total number of events in a given centrality bin.

$$X = \frac{\sum_i n_i X_i}{\sum_i n_i} \tag{3.39}$$

Figure 3.15 shows the effect of CBWC tested on different finite centrality bin widths. Results were tested on four different bin widths and there was no significant effect of the variations on the cumulants except for small deviations in most central collisions (*d, h,* and *j* sub plots of Figure 3.15). However, these deviations are consistent within the statistical uncertainties.

The centrality resolution effect is related to the initial geometry of the system after heavy-ion collisions. This arises because produced particle multiplicities and the impact parameter do not necessarily correspond one-to-one. Therefore, there

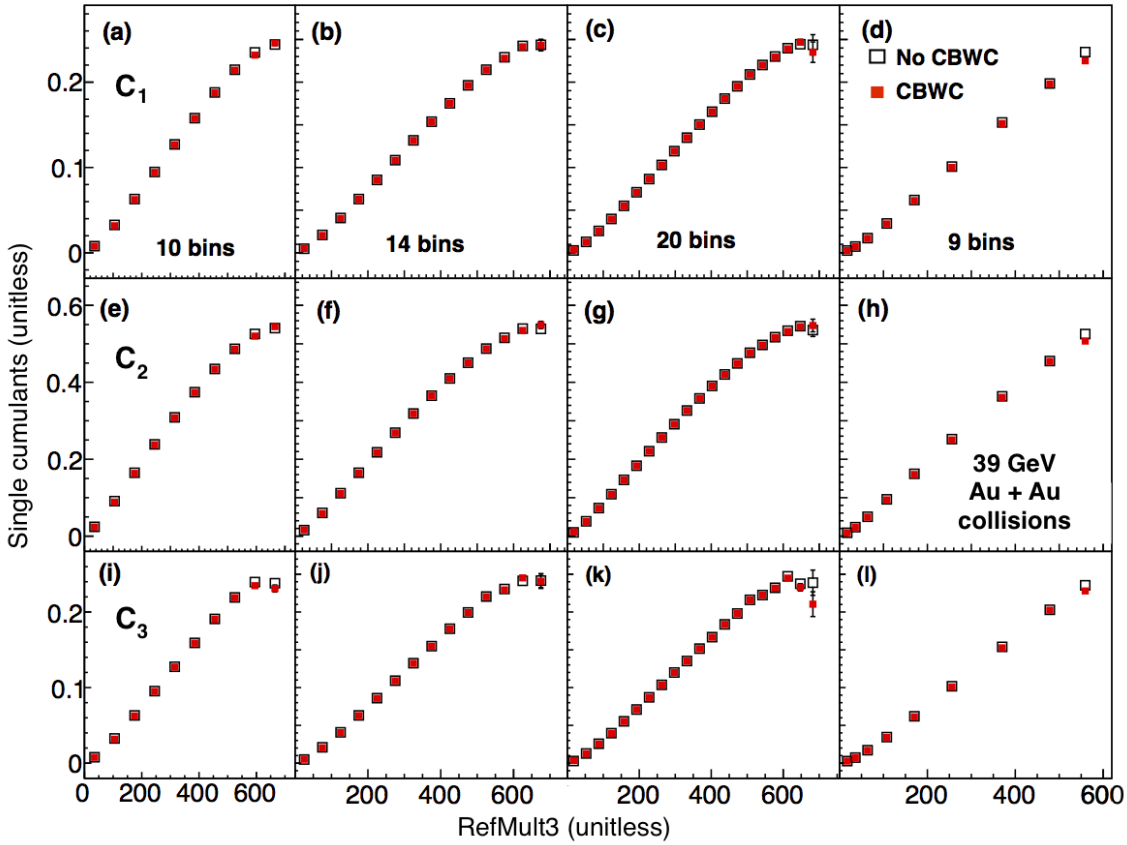

Figure 3.15: Effect of centrality bin-width correction (CBWC) on net-Λ cumulants (C_1, C_2, and C_3) from 39 GeV Au + Au collisions. Only the statistical uncertainties are shown. Bin centers of Refmult3 axis in *d, h,* and *l* sub-plots were weighted by the number of particles in each RefMult3 bin.

could be differences of results depending on the different centrality definitions. This effect is shown in Figure 3.16 [24] where the ultra relativistic molecular-dynamics (UrQMD) model was used to calculate the net-proton cumulant ratios C_3/C_2 ($S\sigma$) and C_4/C_2 ($\kappa\sigma^2$) in centrality definitions which use particles with different acceptance ($|y| < 0.5, 1.0, 1.5$, and 2.0). In RefMult3, a wider acceptance coverage ($|y| < 1.0$) was used for the acceptance of the particles (primary kaons and pions) in order to account for the CRE.

The results presented in this analysis were corrected for CBWE and accounted

for the effects of CRE. Centrality-dependence results are presented in nine centrality bins from 0-5% (most central collisions) to 70-80% (most peripheral collisions). For the representation of the centrality dependence in this analysis, the average number of participant nucleons ($\langle N_{part} \rangle$) was used.

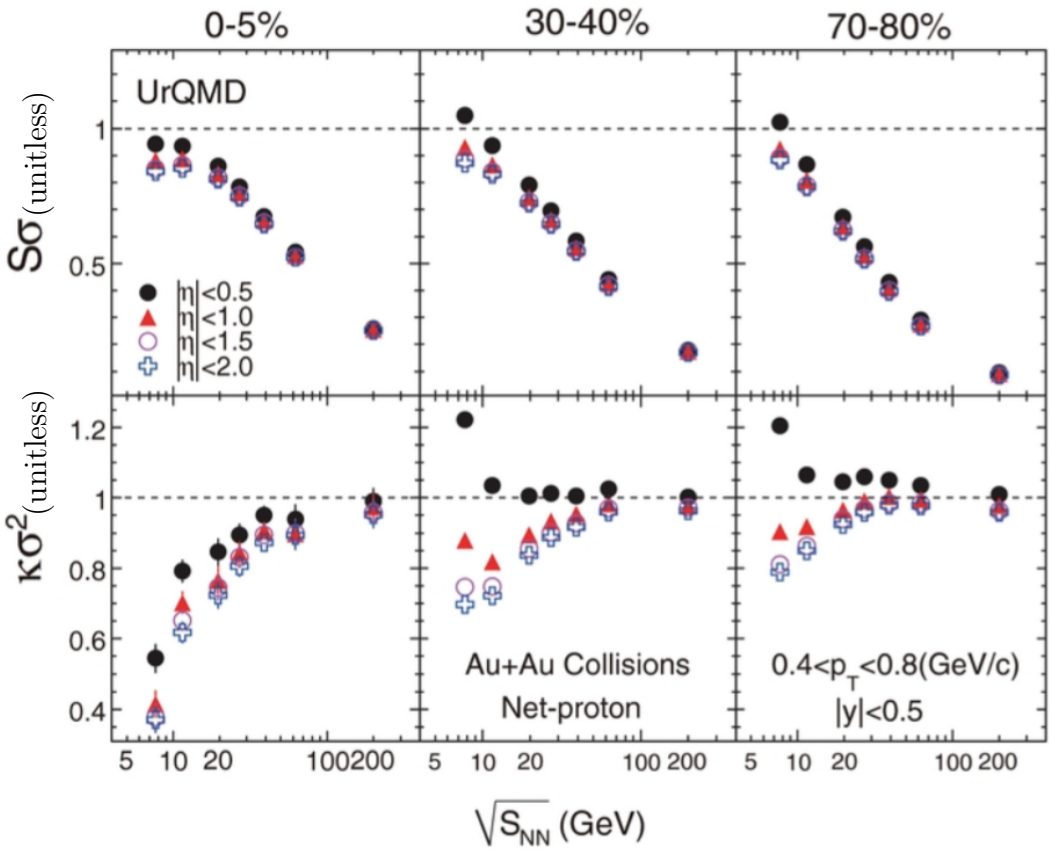

Figure 3.16: The energy dependence of the moments products ($S\sigma$, $\kappa\sigma^2$) of net-proton multiplicity distributions for Au+Au collisions at $\sqrt{s_{NN}}$ = 7.7, 11.5, 19.6, 27, 39, 62.4, and 200 GeV in the UrQMD model with different centrality definitions [24].

3.11 V^0 reconstruction efficiency and efficiency correction methods.

In real world experiments, we do not observe 100% detector efficiency. On top of that, there is finite acceptance and also several geometrical cuts need to be imposed in order to arrive at a required purity. Therefore, we always identify less particles than the actual number present in the system after the collision. To account for this loss, the V^0 reconstruction efficiency should be calculated and corrections must be applied accordingly. For this purpose, specific detector response functions defined in GEANT and real events with known number of embedded particles were used and V^0 reconstruction efficiency was calculated as in Equation 3.40. Here, $\varepsilon(p_T)$ is the reconstruction efficiency as a function of transeverse momentum (p_T), $f_{GEN}(p_T)$ is the generated p_T spectrum of V^0s and $f_{REC}(p_T)$ is the reconstructed p_T spectrum of V^0s.

$$\varepsilon(p_T) = \frac{f_{REC}(p_T)}{f_{GEN}(p_T)} \tag{3.40}$$

In the process of calculating the efficiency in STAR, first, a known number of particles are thrown into a real event environment which is called embedding. The purpose of embedding is to provide users with Monte Carlo tracks with known particle types and their kinematics. The way these particles are reconstructed provides a base line which can be used to correct for the acceptance effects.

Embedding of V^0s can be done independent of transverse momentum (embedded flat in p_T) or by including a dependency of transverse momentum (embedded exponentially in p_T). Selecting one of these types of embedding depends on the need

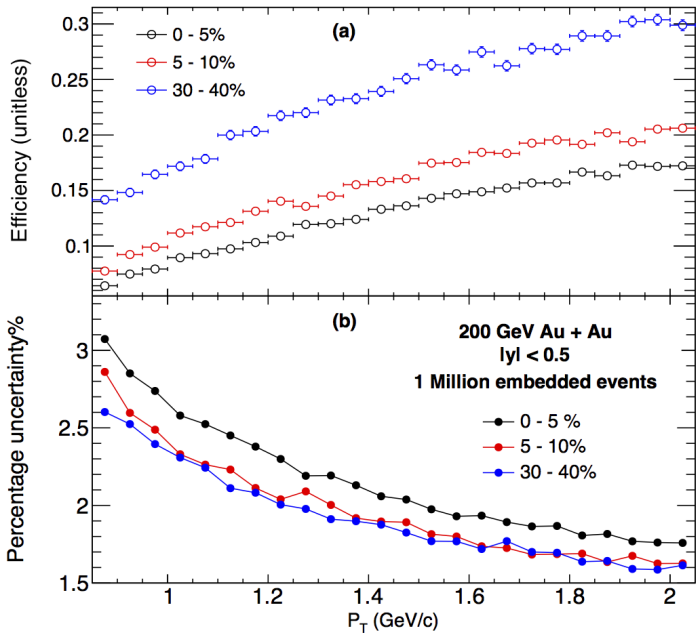

Figure 3.17: (a). Centrality dependence of reconstruction efficiency calculated from 1 million embedded events in 200 GeV Au + Au collisions. (b). Percentage uncertainty estimated for reconstruction efficiency. [25].

and the type of analysis. For this analysis, samples of V^0s embedded flat in p_T were used since the need was to find the number of V^0s recovered after the vertex reconstruction and also after imposing strict topological cuts.

The calculated V^0 reconstruction efficiency could depend on many factors like transverse momentum, rapidity, and collision-centrality. Transverse momentum and centrality dependence of the V^0 reconstruction efficiency are shown in Figure 3.17 (a). The centrality-dependence of efficiency has been taken into account since the corrections for the analysis was done separately in each centrality bin. Transverse momentum dependency of efficiency should also be taken into account and is described in Section 3.11.2 (p_T dependent efficiency correction). In most STAR past fluctuation measurement analyses, efficiency corrections were done by considering the p_T averaged efficiency as described in Section 3.11.1 (p_T independent efficiency

correction). In this analysis, different approaches were tested and final results were corrected for efficiency using p_T dependent efficiency correction.

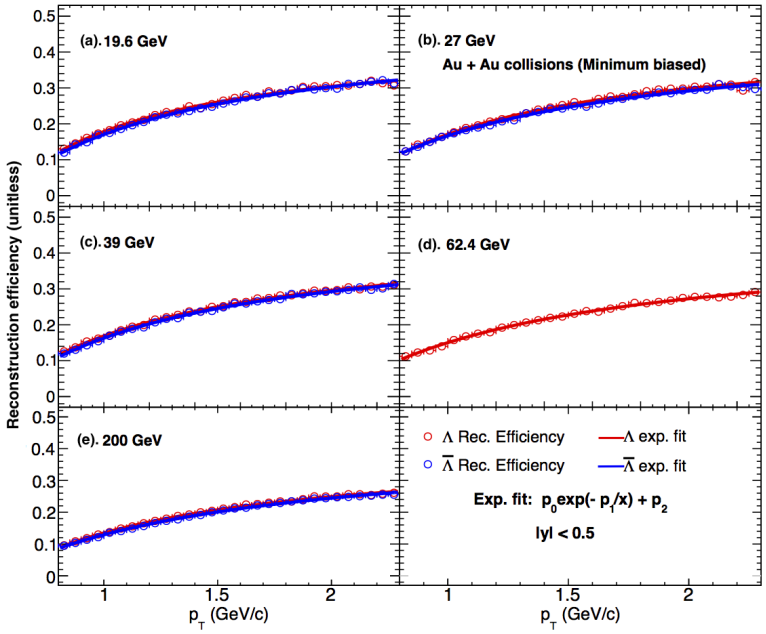

Figure 3.18: V^0 reconstruction efficiency of Λ and $\overline{\Lambda}$ as a function of transverse momentum for five collision energies from 19.6 to 200 GeV Au + Au collisions. Solid lines are the fit ($p_0 \exp(-p_1/x) + p_2$ where, p_0, p_1 and p_2 are free parameters) to the data points. For 62.4 GeV, only Λ-reconstruction efficiency is presented.

The uncertainty in reconstruction efficiency was calculated according to the procedure explained in [25]. The calculated percentage uncertainty on the efficiency is shown in Figure 3.17 (b) and was also used to determine the variation of efficiency in the estimation of systematic uncertainty. As seen in Figure 3.18, within the uncertainties, Λ and $\overline{\Lambda}$ efficiencies show no differences for all collision energies. Therefore, in the efficiency corrections, Λs and $\overline{\Lambda}$s were treated equally.

3.11.1 p_T-independent efficiency correction.

As mentioned in the previous section, in most fluctuation measurements analysis in STAR, efficiency corrections were done using the p_T averaged efficiency which was calculated using Equation 3.41. This calculation was done in each individual centrality bin by using the efficiency corrected p_T spectra of Λ ($f(p_T)$) and momentum dependent reconstruction efficiency $\varepsilon(p_T)$. Integration was done over the entire p_T range of the analysis (0.9 GeV/c $< p_T <$ 2.0 GeV/c).

$$\varepsilon = \frac{\int_{0.9}^{2.0} \varepsilon\left(p_T\right) f\left(p_T\right) p_T dp_T}{\int_{0.9}^{2.0} f\left(p_T\right) p_T dp_T} \tag{3.41}$$

$$\varepsilon C_1 = c_1 \tag{3.42}$$

$$\varepsilon^2 C_2 = c_2 - n(1-\varepsilon) \tag{3.43}$$

$$\varepsilon^3 C_3 = c_3 - c_1\left(1-\varepsilon^2\right) - 3(1-\varepsilon)\left(f_{20} - f_{02} - nc_1\right) \tag{3.44}$$

$$n \equiv \langle n_1 \rangle + \langle n_2 \rangle = f_{10} + f_{01} \tag{3.45}$$

Once the p_T averaged efficiency was calculated, efficiency corrections were done for the cumulants as described in Equations 3.42 - 3.45 where c_m represents uncorrected cumulants and C_m represents corrected cumulants [26]. The cumulants separately were corrected for efficiency in each centrality bin. The correction becomes more sensitive in higher order cumulants. The p_T-averaged efficiency calculated with the topological cuts used in this analysis was in the $\sim$ 15% level and higher order cumulants become difficult to interpret. Therefore, in this analysis, only the first three efficiency corrected cumulants (C_1, C_2, C_3) and cumulant ratios (C_2/C_1, C_3/C_2) are presented.

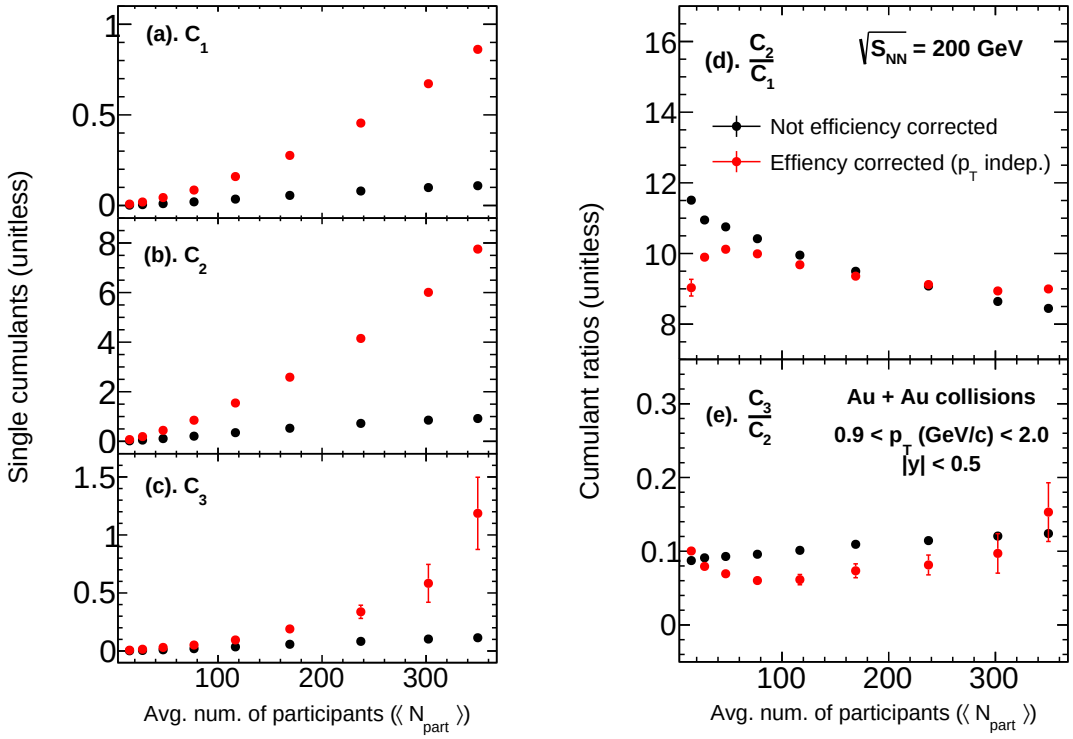

Figure 3.19: Comparison between efficiency corrected and un-corrected net Λ single cumulants: C_1, C_2, and C_3 (a, b, c) and cumulant ratios: C_2/C_1, C_3/C_2 (d, e) as a function of average number of participant nucleons ($\langle N_{part} \rangle$) for 200 GeV Au + Au collisions. Results were corrected for CBWE and p_T-independent efficiency correction was used. Only statistical errors are presented.

As shown in Figure 3.19 (a, b, c), the efficiency correction increased all three cumulants C_1, C_2, and C_3 by a large factor. However, the effect of efficiency correction on the cumulant ratios (C_2/C_1, C_3/C_2) was relatively small compared to the single cumulants as seen in Figure 3.19 (d, e). The statistical uncertainties of C_3 and C_3/C_2 in most central collisions become large due to higher order correction factors and due to low-reconstruction efficiency. In peripheral collisions, corrected C_2/C_1 deviates (significantly lower) from the uncorrected values. This observation is possible due to the use of p_T-independent efficiency correction and this matter was then addressed in the p_T-dependent efficiency correction as explained in the next section.

3.11.2 p_T-dependent efficiency correction

Reconstruction efficiency depends on various factors and one of them is the momentum of produced particles. For instance, low momentum particles may not traverse all the way through to the detector. Therefore, in most cases, the reconstruction efficiency becomes relatively small in low momentum region. For Λ and $\overline{\Lambda}$ reconstruction efficiency, this effect is visible at all energies as shown in Figure 3.18. Doing the efficiency correction using p_T-averaged efficiency as explained in the previous section will not completely take this dependency into account. Therefore, in this section, important steps used for the p_T-dependent efficiency correction are shown in Equations 3.46 - 3.56 as explained in [27] and the correction was done using three p_T bins as shown in Figure 3.19 ($0.9 < p_T(GeV/c) < 1.2$, $1.2 < p_T(GeV/c) < 1.6$ and $1.6 < p_T(GeV/c) < 2.0$).

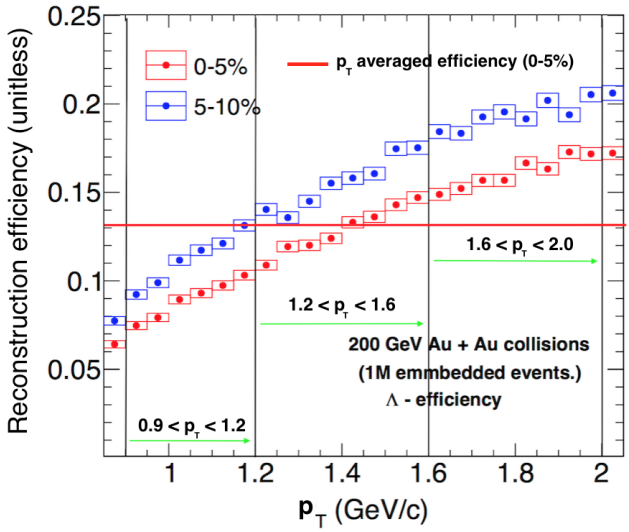

Figure 3.20: p_T dependence of reconstruction efficiency for 0-5% central and 5-10% central 200 GeV Au + Au collisions. Black vertical lines are the boundaries for three acceptance regions used in the corrections. Red horizontal line shows the equivalent p_T-averaged efficiency.

This efficiency correction is done by considering the binomial model. Suppose

the multiplicity distribution of a particle number N is given by P(N). Suppose that individual particles are observed with a probability, p, which is independent for different particles. If the number of observed particles is denoted as n, and the distribution of n as $P(n)$, then it is related to $P(N)$ using the binomial distribution function as

$$P(n) = \sum_N P(N) B_{p,N}(n) \tag{3.46}$$

Here the binomial distribution $B_{p,N}(n)$ is given by

$$B_{p,N}(n) = \frac{N!}{n!(N-n)!} p^n (1-p)^{N-n} \tag{3.47}$$

According to the method described in [27], for the multivariate case, consider the probability distribution function

$$P(N) = P\left(N_1, N_2, \ldots, N_M\right) \tag{3.48}$$

For M stochastic variables $N_1, N_2, ..., N_M$ where N_i with different i represent particle numbers entering detectors which cover different acceptances. Then the cumulant generation function $K(\theta)$ is defined as

$$K(\boldsymbol{\theta}) = \ln \left[\sum_N e^{\theta_1 N_1 + \ldots + \theta_M N_M} P(\boldsymbol{N}) \right] \tag{3.49}$$

Then the $Q_{(a)}$ is defined as the linear combination of N_i

$$Q_{(a)} = \sum_{i=1}^{M} a_i N_i \tag{3.50}$$

The m^{th} order cumulant can be expressed as

$$\left\langle Q_{(a)}^m \right\rangle_c = \partial_{(a)}^m K\left(\theta\right)|_{\boldsymbol{\theta}=0} \tag{3.51}$$

where

$$\partial_{(a)} = \sum_{i=1}^{M} a_i \frac{\partial}{\partial \theta_i} \tag{3.52}$$

Here, $a = 1$ for baryons and $a = -1$ for anti-baryons and M represents the different acceptance regions. Explicit results up to the 3^{rd} order are shown below as described in [27]. In this analysis, three acceptance (p_T) regions were used. Ideally the number of p_T bins should be maximized, but the required computing time for the calculation grows considerable with more p_T bins. Therefore, a test was performed using the finer p_T segmentation with 6 p_T bins which yield the same results than the results from the analysis done with 3 p_T bins. Therefore, the analysis was performed in the three acceptance regions as illustrated in Figure 3.20.

$$\langle Q \rangle_{\mathrm{c}} = \left\langle q_{(1,1)} \right\rangle_{\mathrm{c}} \tag{3.53}$$

$$\left\langle Q^2 \right\rangle_{\mathrm{c}} = \left\langle q_{(1,1)}^2 \right\rangle_{\mathrm{c}} + \left\langle q_{(2,1)} \right\rangle_{\mathrm{c}} - \left\langle q_{(2,2)} \right\rangle_{\mathrm{c}} \tag{3.54}$$

$$\begin{aligned} \langle Q^3 \rangle_{\mathrm{c}} = \langle q_{(1,1)}^3 \rangle_{\mathrm{c}} + 3 \left\langle q_{(1,1)} q_{(2,1)} \right\rangle_{\mathrm{c}} - 3 \left\langle q_{(1,1)} q_{(2,2)} \right\rangle_{\mathrm{c}} \\ + \left\langle q_{(3,1)} \right\rangle_{\mathrm{c}} - 3 \left\langle q_{(3,2)} \right\rangle_{\mathrm{c}} + 2 \left\langle q_{(3,3)} \right\rangle_{c} \end{aligned} \tag{3.55}$$

$$q_{(r,s)} = q_{(a^r/\varepsilon^s)} = \sum_{i=1}^{M} \left(a_i^r / \varepsilon_i^s \right) n_i \tag{3.56}$$

The corrected results using the p_T-dependent efficiency correction method are shown in Figure 3.21 with a comparison to the results corrected using p_T-independent efficiency correction method for 200 GeV Au + Au collisions. The single cumulants and cumulant ratios in most central collisions are independent of the efficiency correction method. The important observation here is that, in most peripheral collisions (60-70% and 70-80%), C_2/C_1 calculated with p_T-dependent efficiency correction became larger than p_T-independently corrected C_2/C_1. The corrected C_2/C_1 using a

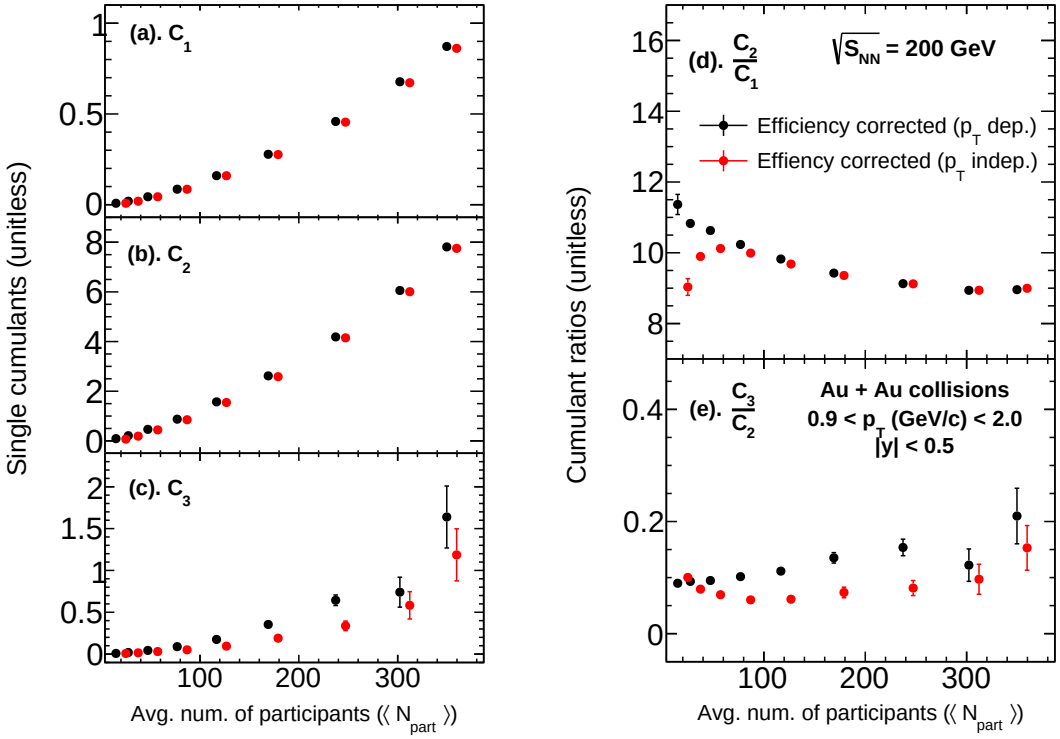

Figure 3.21: Comparison between different efficiency correction methods, p_T-independent and p_T-dependent for net-Λ single cumulants: C_1, C_2, and C_3 (a, b, c) and cumulant ratios: C_2/C_1, C_3/C_2 (d, e) as a function of average number of participant nucleons ($\langle N_{part} \rangle$) for 200 GeV Au + Au collisions. Results were corrected for CBWE. Only statistical uncertainties are presented.

p_T-dependent efficiency correction is in accordance with the baseline expectations and therefore the issue in peripheral collision when C_2/C_1 was calculated using p_T-independent correction was resolved. All the centrality and energy dependence of net-Λ cumulants presented in this analysis were corrected for the reconstruction efficiency using p_T-dependent efficiency correction as explained in this section.

3.11.3 Feed-down correction

There may be contamination in the Λ and $\overline{\Lambda}$ yields due to the weak decays of multi-strange baryons like Ξ and Ω. These weak decays take place in the very proximity of the primary vertex and therefore Λs or $\overline{\Lambda}$s coming from Ξ and Ω weak decays could mistakenly be identified as primary particles. To correct for this contamination, feed-down contribution from Ξ and Ω should be estimated and subtracted from the raw yields. In this analysis, a feed-down contribution of 15% is considered [28] and the correction was done according to the Equation 3.57 where, ε is the reconstruction efficiency without feed-down correction, $\varepsilon^{'}$ is the reconstruction efficiency with feed-down correction included, and δ is the feed-down contribution level.

$$\varepsilon^{'} = \frac{\varepsilon}{(1-\delta)} \tag{3.57}$$

The feed-down corrected and efficiency corrected p_T spectra for Λ and $\bar{\Lambda}$ from 39 GeV Au + Au collisions at STAR are presented in Figure 3.22. Comparison of feed-down corrected and uncorrected net Λ single cumulants and cumulant ratios are shown in Figure 3.23. As expected, the single cumulants (C_1, C_2 and C_3) have smaller values when the feed-down correction was applied. But in cumulant ratios, there was no significant difference between the feed-down corrected and uncorrected results.

The estimation of the feed-down contribution should be done as a function of momentum, collision energy, and centrality. In the narrow p_T range used in this analysis, the feed-down contribution was assumed to be independent of p_T. A test was performed to estimate the feed-down contribution as a function of collision energy. The efficiency corrected p_T spectra from this analysis without the feed-down

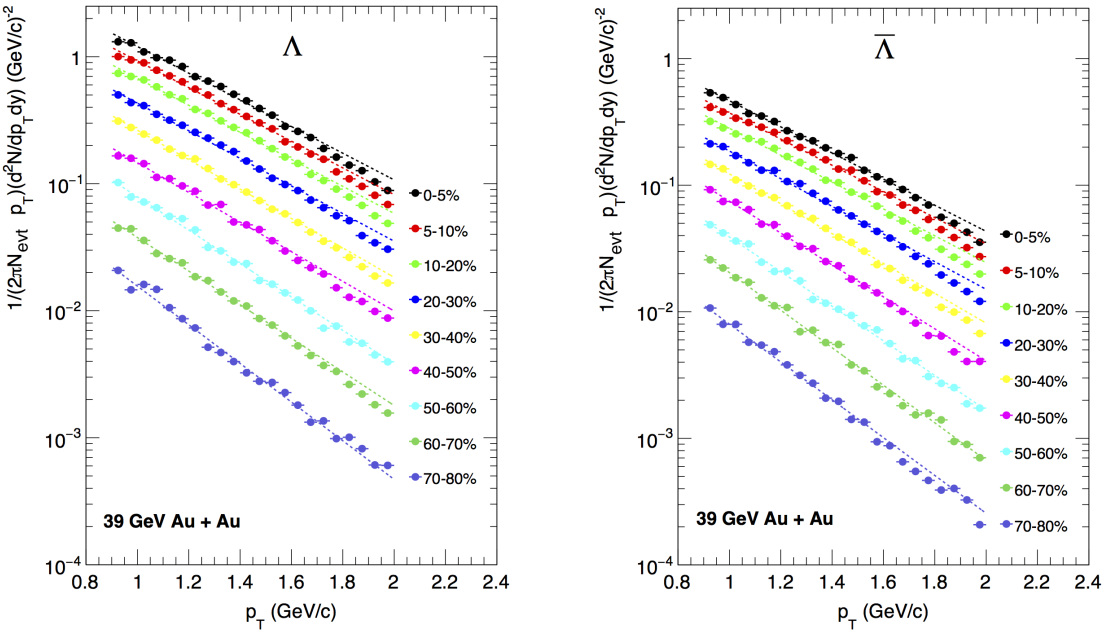

(a) (b)

Figure 3.22: Normalized p_T spectra of (a). Λ and (b). $\bar{\Lambda}$ in different collision centralities and in rapidity window, $|y|_{V^0} < 0.5$ for 39 GeV Au + Au collisions at STAR. Dashed line represents an exponential fit ($p_0 e^{-1/p_T}$, where p_0 is a free parameter). Results were corrected for reconstruction efficiency and feed-down contribution. N_{evt} represents the number of events.

contribution were compared with efficiency corrected and feed-down corrected p_T spectra from the analysis presented in [29] at STAR. It was found that the feed-down contribution is in a level of ∼15% from 19.6 to 200 GeV. One of the reasons for the weak dependence of feed-down contributions in this analysis as a function of collision energy could possibly be due to very strict topological cuts used in the reconstruction of V^0s. For instance, the DCA of V^0 primary vertex cut used in this analysis has a much higher purity than the cuts used in other analysis where the V^0 signal extraction was done by the background subtraction methods.

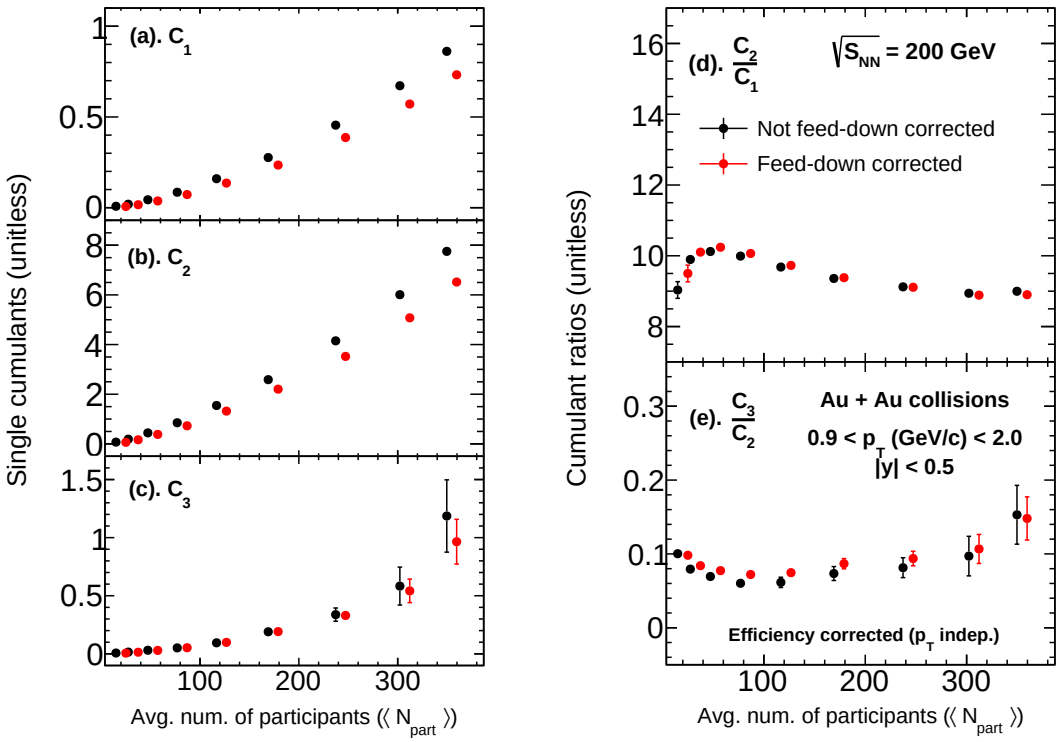

Figure 3.23: Comparison between feed-down corrected and uncorrected net-Λ single cumulants: C_1, C_2, and C_3 (a, b, c) and cumulant ratios: C_2/C_1, C_3/C_2 (d, e) as a function of average number of participant nucleons ($\langle N_{part} \rangle$) for 200 GeV Au + Au collisions. Results are corrected for CBWE. Only statistical uncertainties are presented.

3.12 Estimation of systematic uncertainties

Systematic uncertainties can arise due to various sources such as imperfect calibration of the measuring instruments, or imperfect methods of observations. Detector imperfections can be addressed up to some level in the efficiency corrections using simulated environments as explained in previous sections (3.11.1 and 3.11.2). But there are other sources of systematic uncertainties which need to be addressed in detail. One of them is the uncertainty associated with the selection process used for the identification of charged particles in STAR TPC. Ionization energy loss was

used to identify charged particles in TPC and the purity of the samples depends on the conditions applied such as particle identification (PID) cuts. Boundaries for cut variables were decided by considering factors such as expected purity. Therefore, the influence of the variations of charged particle identification criteria on the final results was examined and included as one of the sources for systematic uncertainty.

Different topological cuts were used for the reconstruction of V^0s as explained in Section 3.6. These cuts also affect the purity of the sample and the reconstruction efficiency as well. Therefore, variations of these topological cuts were also included as another source for systematic uncertainty estimation. In addition, uncertainties in the reconstruction efficiency were also included as a source for systematic uncertainties. Estimation of the uncertainty associated with the reconstruction efficiency is explained under the Section 3.11 and is at 2.25%. All the sources and their variation are listed in Table 3.5. The root mean square (RMS) value for each cut variations are shown in Figure 3.24 and 3.25 for C_2/C_1 and C_3/C_2, respectively. The calculation of systematic uncertainty was done as shown in Equations 3.58 and 3.59 by taking the contributions from all potential sources mentioned above.

Table 3.5 shows the sets of different PID and topological cut variations performed to estimate systematic uncertainty. For each cut-set variation, results are corrected for the reconstruction efficiency. Then, the point by point difference between the results from each cut selection and the default results was calculated. The RMS value for each cut was calculated from Equation 3.58 where N stands for the number of different cuts used in a certain cut variation, X_i stands for the results from a certain cut set, and Y stands for the default results. Finally the systematic uncertainty was calculated as shown in Equation 3.59 where j stands for the number of sources used in the error estimation.

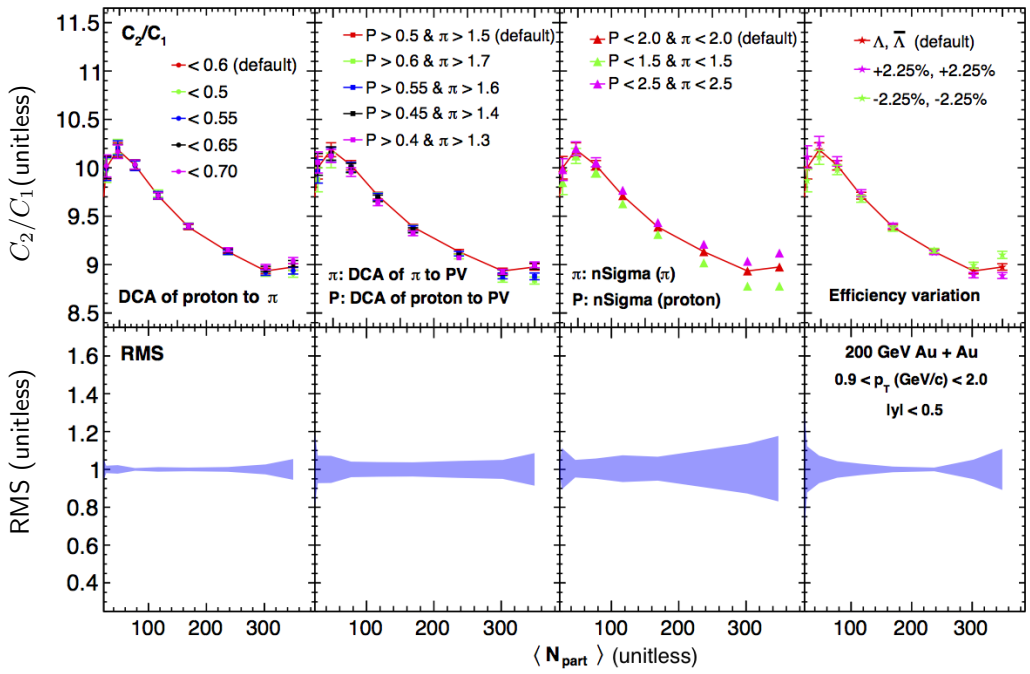

Figure 3.24: Effect of cut parameter and efficiency variations on the efficiency corrected net-Λ C_2/C_1 for the estimation of systematic uncertainties in 200 GeV Au + Au collisions.

$$RMS = \sqrt{\frac{1}{N}\Sigma_{i-1}^{N}\left(X_i - Y\right)^2} \tag{3.58}$$

$$SysErr. = \sqrt{\Sigma_j RMS_j^2} \tag{3.59}$$

The main source of the systematic uncertainty is the selection criteria used in the identification of protons and pions. It has a relative contribution of 44.9% to the systematic uncertainty in C_2/C_1 for 0-5% central collisions at 200 GeV. The second largest contribution comes form the efficiency variations. The contribution of the topological cut variations on the systematic error was relatively small as seen in Figure 3.24. Similarly, as seen in Figure 3.25, cut variations done on PID for proton and pion had the largest contribution in the RMS calculation for C_3/C_2.

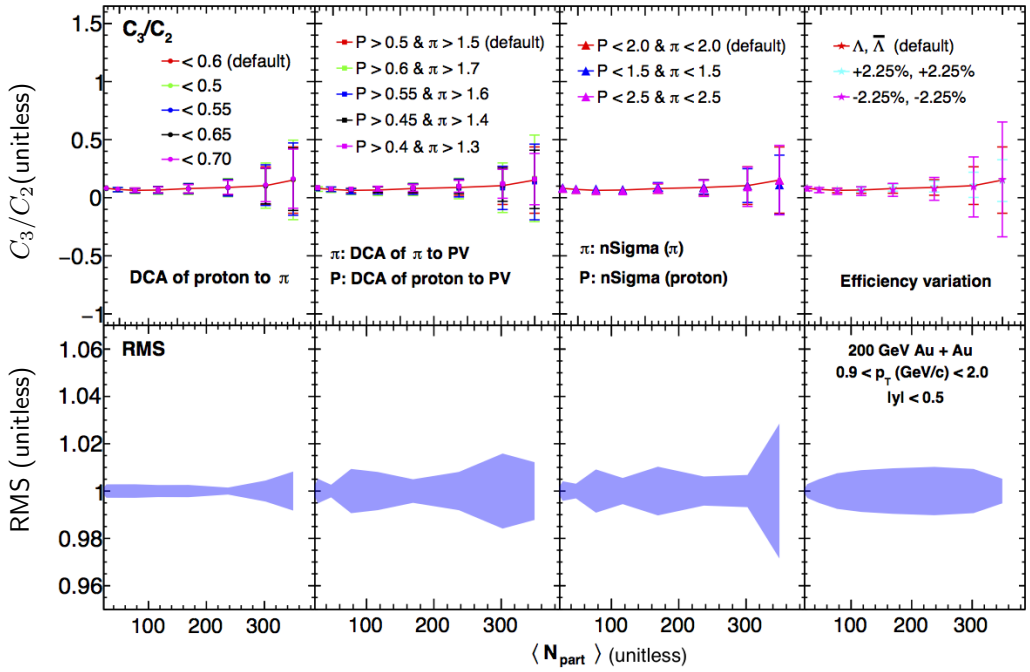

Figure 3.25: Effect of cut parameter and efficiency variations on the efficiency corrected net-Λ C_3/C_2 for the estimation of systematic uncertainties in 200 GeV Au + Au collisions.

The absolute systematic uncertainties of net-Λ cumulants and cumulant ratios are presented in Appendix A.2 - A.6.

3.13 Baselines for the net-Λ distributions.

A study of different baselines and model expectations was done in order to understand the underlying physics interpretation to the experimentally measured data and also to keep track of any possible deviations of data from baselines. In the following sections, several baselines and model calculations used in this analysis are discussed.

Table 3.5: Different sources of the systematic uncertainty, their variations and the contribution for the systematic error. Relative contributions are calculated in the most central collisions (0-5%) of C_2/C_1 in 200 GeV Au + Au collisions.

Source	Variations	Contribution
DCA of p to π	< 0.6 (default) < 0.5 < 0.55 < 0.65 < 0.70	11.2%
DCA of π to PV & p to PV	> 0.5 & > 1.5 (default) > 0.6 & > 1.7 > 0.55 & > 1.6 > 0.45 & > 1.4 > 0.4 & > 1.3	20.3%
$n\sigma$ (π) & $n\sigma$ (P)	< 2.0 & < 2.0 (default) < 2.5 & < 2.5 < 1.5 & < 1.5	44.9%
Eff (Λ) & Eff ($\overline{\Lambda}$)	ε & ε (default) $\varepsilon \times (1 + 2.25\%)$ & $\varepsilon \times (1 + 2.25\%)$ $\varepsilon \times (1 - 2.25\%)$ & $\varepsilon \times (1 - 2.25\%)$	23.6%

3.13.1 Central Limit Theorem (CLT).

In probability theory, the central limit theorem says that, when random variables are added, their properly normalized sum tends towards a normal distribution. For instance, take a sample obtained with a large number of observations so that these observations do not depend on each other. Then if the arithmetic average of this sample is calculated, CLT says that if this process is done many times, these computed averages of samples will be distributed according to a normal distribution.

In heavy ion collisions, the centrality dependence of moments of net-particle multiplicity distributions can be understood in the by the CLT. Moments show dependence of averaged number of participant nucleons (N_{part}). In the context of CLT,

N_{part} can be considered as sources of independent emission of particles. With this description, the first four moments of net particle multiplicity distributions can be expressed in terms of N_{part} as

$$M \propto < N_{\rm part} > \tag{3.60}$$

$$\sigma \propto \sqrt{< N_{\rm part} >} \tag{3.61}$$

$$S \propto \frac{1}{\sqrt{< N_{\rm part} >}} \tag{3.62}$$

$$\text{and}\, \kappa \propto \frac{1}{< N_{\rm part} >} \tag{3.63}$$

The central limit theorem expectations for the first four moments of net-Λ are shown in Figure 4.1 for five Au + Au collision energies from 19.6 to 200 GeV as a function of collision centrality in next chapter.

3.13.2 Poisson baseline.

In this approach, individual particle distributions are assumed to be Poissonian. Then, the baseline for net particle multiplicity distributions would be the difference of two independent Poisson distributions which is called a Skellam distribution. The probability mass function for Skellam distribution is

$$P(N) = \left(\frac{\mu_1}{\mu_2}\right) (N/2) I_N \left(2\sqrt{\mu_1 \mu_2}\right) e^{-(\mu_1+\mu_2)} \tag{3.64}$$

Here, μ_1 and μ_2 are the means of individual Λ and anti-Λ particle distributions (μ_Λ and $\mu_{\overline{\Lambda}}$, respectively). I_N are the modified Bessel functions of the first kind. Then, the baselines for cumulants of the net-Λ distribution can be calculated as

$$C_{2n} = \mu_{\Lambda} + \mu_{\overline{\Lambda}}, (n = 1, 2, 3, \dots) \tag{3.65}$$

$$C_{2n-1} = \mu_{\Lambda} - \mu_{\overline{\Lambda}}, (n = 1, 2, 3, \dots\dots) \tag{3.66}$$

$$\frac{C_2}{C_1} = \frac{\mu_{\Lambda} + \mu_{\overline{\Lambda}}}{\mu_{\Lambda} - \mu_{\overline{\Lambda}}} \tag{3.67}$$

$$\frac{C_3}{C_2} = \frac{\mu_{\Lambda} - \mu_{\overline{\Lambda}}}{\mu_{\Lambda} + \mu_{\overline{\Lambda}}} \tag{3.68}$$

The collision centrality, collision energy, and rapidity dependence of net-Λ cumulants and cumulant ratios are presented using Poisson expectations as one of the baselines and possible deviations from the baselines. This is discussed in the next chapter.

3.13.3 Negative binomial expectations.

In probability theory, if we consider a sequence of independent and identically distributed Bernoulli trials, then the number of successes before a specified number of failures occurred can be described by a negative binomial distribution (NBD). NBD is a discrete probability distribution and the probability mass function is:

$$NB(k; r, p) = \begin{pmatrix} k + r - 1 \\ k \end{pmatrix} p^r (1 - p)^k \tag{3.69}$$

where p is the probability of success, r stands for the number of failures before the experiment is stopped (stopping parameter), and k is the number of successes.

The NBD is valid if the mean (M) of a distribution is less than the variance (σ^2) of the distribution. The NBD expectations for the cumulants can be written as

$$C_2 = \sigma^2 = r\mu \tag{3.70}$$

$$C_3 = S\sigma^3 = r\mu(2r-1) \tag{3.71}$$

$$C_4 = \kappa\sigma^4 = r\mu\left(6r^2 - 6r + 1\right) \tag{3.72}$$

where, μ is the mean, and $r = \frac{\sigma^2}{\mu}$. Finally the NBD expectation for net-Λ cumulants can be calculated considering the cumulants of individual particle distributions as

$$C_n = C_n^+ + (-1)^n C_n^- \tag{3.73}$$

3.13.4 UrQMD simulation study.

The ultra relativistic molecular dynamics (UrQMD) model is a fully integrated Monte Carlo simulation package which can be used to study the evolution of the system after heavy-ion collisions [30]. This package has the ability to simulate p + p, p + Au and Au + Au collisions at both RHIC and LHC energies which provides base lines for the experimentally measured quantities.

The dynamics of UrQMD are based on co-variant propagation of color strings, constituent quarks, and di-quarks accompanied by mesonic and baryonic degrees of freedom. In addition, it includes re-scattering of particles, the excitation and fragmentation of color strings, and the formation and decay of hadronic resonances. In this analysis, UrQMD expectations for net-Λ single cumulants (C_1, C_2, and C_3) and cumulant ratios (C_2/C_1 and C_3/C_2) were calculated as a function of collision

centrality and collision energy. For these UrQMD calculations, same event, track, V^0 cuts, and the same centrality definition (RefMult3) were used as in the real analysis.

3.13.5 Hadron Resonance Gas model.

The hadron resonance gas (HRG) model has been very successful in fitting particle yields and ratios for the extraction of freeze-out parameters [19]. In the HRG, interacting hadronic matter in the ground state is approximated by a non-interacting resonance gas. Information of particle species included in the calculations come from the most recent version of the particle data booklet [20]. The pressure from the grand canonical partition function can be written as,

$$p^{HRG}/T^4 = \frac{1}{VT^3} \sum_{i\in \text{ mesons}} \ln \mathcal{Z}^M_{m_i}\left(T, V, \mu_{X^a}\right) + \frac{1}{VT^3} \sum_{i\in \text{ baryons}} \ln \mathcal{Z}^B_{m_i}\left(T, V, \mu_{X^a}\right) \tag{3.74}$$

where, m_i stands for mass of the i^{th} particle, M stands for mesons, and B stands for baryons. X^a stands for all possible conserved charges including baryon number (B), electric charge (Q), and strangeness (S). The grand canonical partition function can be written as

$$\ln \mathcal{Z}^{M/B}_{m_i} = \mp \frac{V d_i}{2\pi^2} \int_0^\infty dk k^2 \ln\left(1 \mp z_i e^{-\varepsilon_i/T}\right) \tag{3.75}$$

Here, energy $\varepsilon_i = \sqrt{k^2 + m_i^2}$, fugacity $z_i = \exp^{\frac{\mu_{X_a}}{T}}$ and d_i stands for degeneracy factor. Finally, the susceptibilities of conserved charges can be calculated as

$$\chi^{BSQ}_{lmn} = \frac{\partial^{l+m+n} p/T^4}{\partial\left(\mu_B/T\right)^l \partial\left(\mu_S/T\right)^m \partial\left(\mu_Q/T\right)^n} \tag{3.76}$$

Here, *l, m, and n* stand for the different orders in the susceptibility.

The net Λ fluctuation results were compared to the HRG calculations done following the methods described in [9].

Chapter 4

Results and discussion

In this chapter, net-Λ fluctuation measurements are presented as a function of collision energy, collision centrality, and rapidity. The net Λ distributions were measured for five different Au + Au collision energies from 19.6 to 200 GeV. The cumulant calculations were done according to the procedures described in Chapter 3 of this dissertation. The results presented for centrality and energy dependence of net-Λ fluctuations were corrected for reconstruction efficiency using p_T-dependent efficiency correction as described in Section 3.11.2. For the rapidity dependence of net-Λ fluctuations, results were corrected for the reconstruction efficiency using p_T-independent efficiency correction as explained in Section 3.11.1. The statistical and systematic uncertainties were estimated and are presented separately using vertical error-bars and error-caps, respectively. The results were corrected for the feed-down contributions and for the centrality bin-width effect (CBWE). The results are presented with NBD and Poisson baselines which were calculated as explained in Section 3.13. The predictions from the UrQMD model are presented as a function of collision centrality and energy. The centrality dependence of net-Λ results are presented as

a function of averaged number of participant nucleons ($\langle N_{part} \rangle$). In this chapter, results are presented with a follow-up discussion where the deviations of data from baselines (NBD, Poisson) and model predictions (UrQMD, HRG) are addressed in detail. The rapidity dependence of net-Λ fluctuations is presented as a measure of the sensitivity of the results to baryon-number conservation and discussed in the last two sections of this chapter.

4.1 Centrality dependence of uncorrected net-Λ moments.

The collision centrality is a measure of the degree of overlap between two colliding nuclei. A detailed explanation of the determination of collision centrality in the STAR experiment is given in Section 2.4 of this dissertation. As mentioned earlier, for the representation of collision centrality, the average number of participant nucleons ($\langle N_{part} \rangle$) was used. Figure 4.1 shows the centrality dependence of the first four uncorrected moments (mean - M, standard deviation - σ, skewness - S, and kurtosis - κ) of net-Λ multiplicity distributions for five Au + Au collisions energies (19.6, 27, 39, 62.4, and 200 GeV). Here, "uncorrected moments" means results which were not corrected for reconstruction efficiency or feed-down contribution.

As seen in Figure 4.1, both mean and standard deviation of net-Λ multiplicity distributions increased as a function of increasing collision centrality while skewness and kurtosis decreased. This behaviour of the first four moments as function of collision centrality is mainly because the number of nucleons participating in a given collision increased as a function of increasing collision centrality. This trend in the

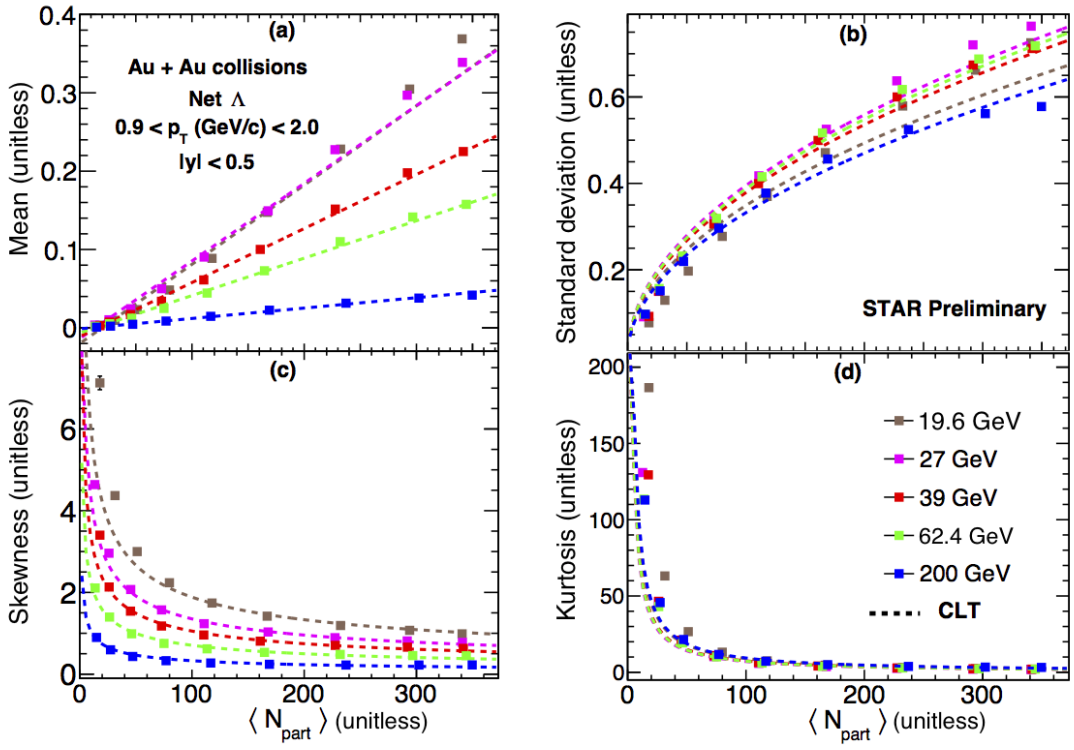

Figure 4.1: Centrality dependence of first four moments (mean-M, standard deviation-σ, skewness-S, and kurtosis- κ) of net-Λ multiplicity distributions at Au + Au collision energies 19.6, 27, 39, 62.4, and 200 GeV. Results are not corrected for reconstruction efficiency or feed-down contribution. Only statistical uncertainties are presented. Dashed lines represent the CLT expectations. CBWC was applied.

data can be approximated by calculated CLT expectations which are represented using dashed lines in Figure 4.1 . For the mean and standard deviation, the CLT has better agreement in peripheral collisions, but deviates in most central collisions. On the other hand, the CLT expectations for both skewness and kurtosis deviate more in peripheral collisions than in central collisions. However, the CLT roughly represent the trends of the centrality dependence for net-Λ moments. Specifically, at 200 GeV, all four measured moments (M, σ, S, and κ) show good agreement with CLT expectations.

4.2 Centrality dependence of net-Λ single cumulants (C_1, C_2, and C_3)

The results of measured net-Λ single cumulats up to the 3^{rd} order are presented with the calculated NBD and Poisson baselines together with UrQMD model expectations. Values of C_1, C_2, and C_3 increase as a function of increasing collision centrality at all energies due to the increase of the number of participant nucleons in most central collisions compared to peripheral collisions. For C_3, small fluctuations can be seen in most central collisions, but they are within the statistical uncertainties and in agreement with both the NBD and Poisson baselines.

The particles observed at the highest collision energies are mostly produced particles, i.e. particles formed in the fireball. That means, the probability of observing primordial particles, i.e. particles that did not participate in the collisions, is low at highest collision energies compared to low energy collisions. Therefore, when the collision energy increases, the probability of finding equal numbers of Λs and $\overline{\Lambda}$s in an event is also increased. As a result, net-Λ C_1 and C_3 for a given centrality class decrease as a function of increasing collision energy. However, the variance of a distribution mostly depends on the variance of the individual particle distributions and the degree of correlations between particles and anti-particles. As seen in Figure 4.2, for a given centrality, net-Λ C_2 shows similar values in 19.6, 27, and 39 GeV collisions but relatively larger at 62.4 and 200 GeV collisions.

The statistical uncertainties are relatively small for C_1 and C_2 but significant in most central collisions for C_3. This is mainly due to the higher order correction factors associated with reconstruction efficiency as explained under the statistical

error estimation in Section 3.9. The systematic uncertainties are dominant in C_2 and increase as a function of increasing collision energy and centrality. Both NBD and Poisson baselines show reasonable agreement with the measured cumulants. For C_2, both baselines behave similarly and agree with data except in the most central collisions at 200 GeV, where there is a visible deviation of the Poisson baseline from the data. The NBD expectations show better agreement with data in C_3 than the Poisson baseline. In the calculation of the NBD expectations, both the mean and variance of individual particle distributions were taken into account. Therefore, it is possible that NBD is capable of reproducing the effects due to particle and anti-particle correlations. The UrQMD model calculations show a better agreement with C_1 and C_3 except at 27 GeV. The measured C_2 deviates from UrQMD at all energies and the deviation increases as a function of increasing collision energy.

In this analysis, only the efficiency corrected net-Λ cumulants up to the 3^{rd} order are presented. It was found that the net-Λ 4^{th} order cumulant (C_4) measurement was not sensitive to centrality or collision energy due to the presence of large statistical uncertainties and it is therefore not presented in this work.

4.3 Centrality dependence of net-Λ cumulant ratios C_2/C_1 and C_3/C_2

The centrality dependence of the net-Λ cumulant ratio C_2/C_1 is presented in Figure 4.3 for 19.6, 27, 39, 62.4, and 200 GeV Au + Au collisions. The results are presented with NBD, Poisson baselines and UrQMD predictions. Both the statistical and systematic uncertainties stay significantly small. Both the NBD and

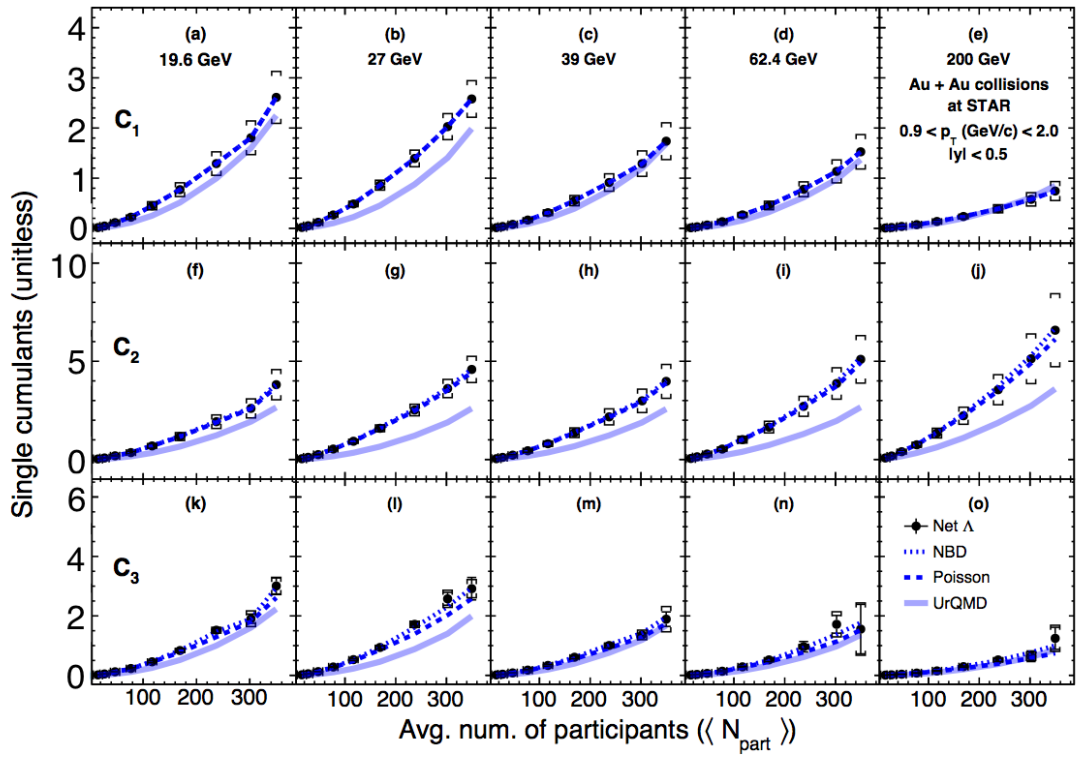

Figure 4.2: Centrality dependence of first three single cumulants, C_1, C_2, and C_3 of net-Λ multiplicity distributions at Au + Au collisions energies, 19.6, 27, 39, 62.4, and 200 GeV. NBD and Poisson baselines are presented by dashed lines. UrQMD predictions are shown in solid lines. Black vertical lines represent the statistical uncertainties and caps represent the systematic uncertainties. Results were corrected for feed-down contribution and reconstruction efficiency. CBWC was applied.

Poisson expectations show better agreement with data except in 200 GeV most central collisions, where a slight deviation from the Poisson baseline is visible. The UrQMD predictions show notable deviations at all energies. This is mainly due to the deviations of UrQMD expectations seen in C_2. This deviation stays constant as a function of centrality in the range of mid-central to most-central collisions at all collision energies.

As described in Chapter 3, the reason for choosing cumulant ratios for the comparison of the fluctuation measurements with theory is they are independent of the

volume of the system. Therefore, the measured net-Λ C_2/C_1 values show a weak dependency on the collision centrality, as expected. The NBD expectations agree with data better than the Poisson baseline at 200 GeV most central collisions (0-5% and 5-10%). This observation explains the importance of including both mean and variance of individual particle multiplicity distributions for the baseline calculations. The agreement of NBD with data is possibly an indication of less intra-event correlation between particles and anti-particles. As observed in Figure 4.3, there are no non monotonic fluctuations present in the net-Λ C_2/C_1 measurement as a function of collision centrality.

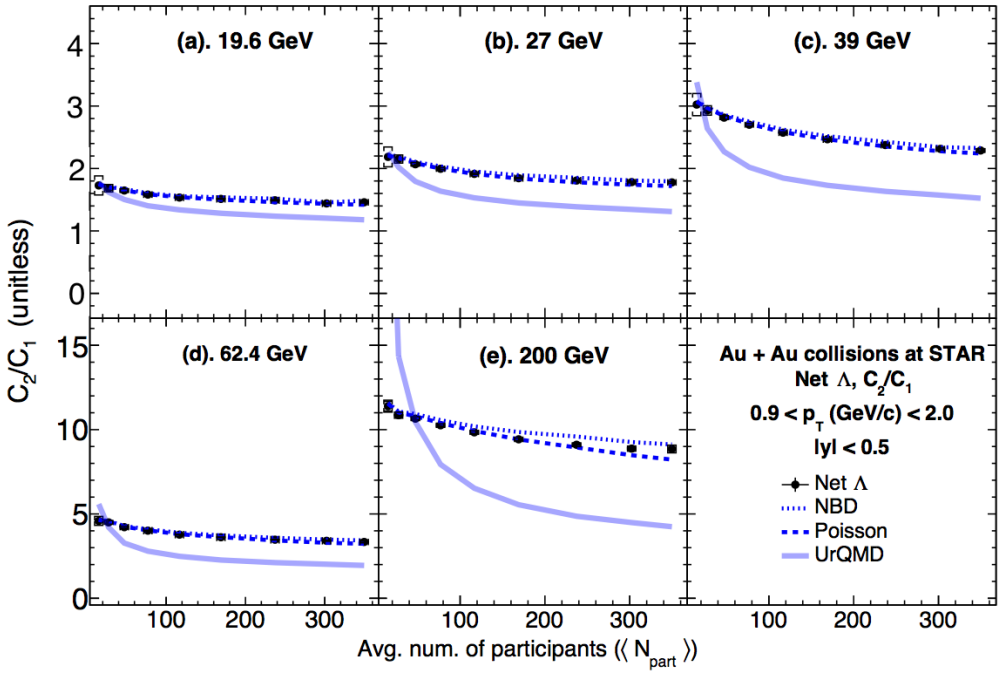

Figure 4.3: Centrality dependence of the lowest order net-Λ cumulant ratio, C_2/C_1 for 19.6, 27, 39, 62.4, and 200 GeV Au + Au collisions. NBD and Poisson baselines are presented by dashed lines. UrQMD predictions are shown in solid lines. Black vertical lines represent the statistical uncertainties and caps represent the systematic uncertainties. Results were corrected for feed-down contribution and reconstruction efficiency. CBWC was applied.

The centrality dependence of the net-Λ cumulant ratio C_3/C_2 for 19.6, 27, 39,

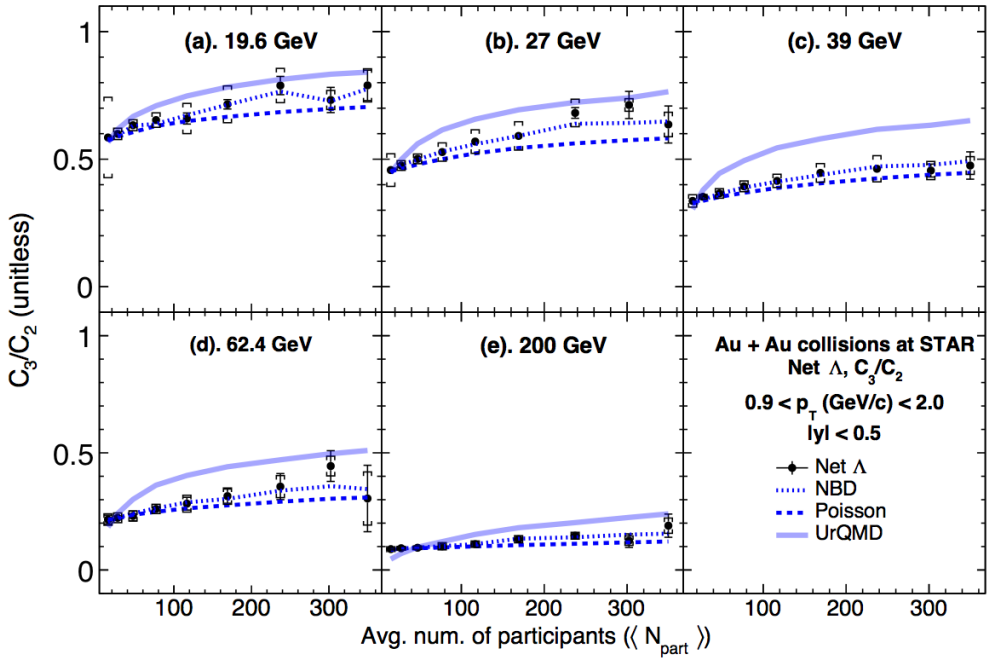

Figure 4.4: Centrality dependence of the net-Λ cumulant ratio, C_3/C_2 for 19.6, 27, 39, 62.4, and 200 GeV Au + Au collisions. NBD and Poisson baselines are presented by dashed lines. UrQMD predictions are shown in solid lines. Black vertical lines represent the statistical uncertainties and caps represent the systematic uncertainties. Results were corrected for feed-down contribution and reconstruction efficiency. CBWC was applied.

62.4, and 200 GeV Au + Au collisions is shown in Figure 4.4. The results are presented with the NBD and Poisson baselines together with UrQMD model predictions. The statistical uncertainties dominate most central collisions at all collision energies due to the effect of low-reconstruction efficiency on the higher-order corrections. However, in mid-central and peripheral collisions, the statistical uncertainties were suppressed and systematic uncertainties dominate. This effect is largest at low energies. Also, systematic uncertainties grew as the collision centrality increased. Both the NBD and Poisson baselines showed reasonable agreement with data within the uncertainties. However, the NBD expectations described the data better than the Poisson baseline, especially in the most central collisions. UrQMD describes the

data in 19.6, 27, and 200 GeV collisions within the uncertainties. However, there are deviations of data from UrQMD in 39, 62.4, and 200 GeV collision energies. The net-Λ C_3/C_2 values are nearly independent of collision centrality which is possibly due to the volume independence. According to Figure 4.4, there are no non monotonic fluctuations present in the net-Λ C_3/C_2 measurements as a function of collision centrality.

4.4 Beam-energy dependence of net-Λ cumulant ratios, C_2/C_1 and C_3/C_2

Figure 4.5 shows the beam-energy dependence of net-Λ cumulant ratios, (a) C_2/C_1 and (b) C_3/C_2 in most central (0-5%) and peripheral (50-60%) collisions with NBD, Poisson baselines, and UrQMD model predictions. As seen in Figure 4.5 (a), C_2/C_1 increases monotonically as a function of increasing collision energy in most central and peripheral collisions. The measured C_2/C_1 value in peripheral collisions is larger than that of most central collisions for all collisions energies. The statistical and systematic uncertainties associated with C_2/C_1 are small in most central and peripheral collisions. In 19.6, 27, 39, and 62.4 GeV collisions, the net-Λ C_2/C_1 values showed better agreement with both the NBD and Poisson baselines. However, at 200 GeV, the NBD expectation showed better agreement with the measured C_2/C_1 values within the systematic uncertainties than the Poisson baseline. The Poisson baselines stayed below the NBD expectations at all energies. The UrQMD predictions deviated by a large amount at all collision energies and the deviation increased

as a function of increasing collision energy. This behaviour mainly due to the deviations of UrQMD from data seen in C_2 calculations (Figure 4.2). The increased net-Λ C_2/C_1 ratio as a function of increasing collision energy was mainly driven by C_1 as seen in Figure 4.2. The agreement of the C_2/C_1 ratio with the NBD expectations as a function of collision energy is an indication of less intra-event correlations between particles and anti-particles.

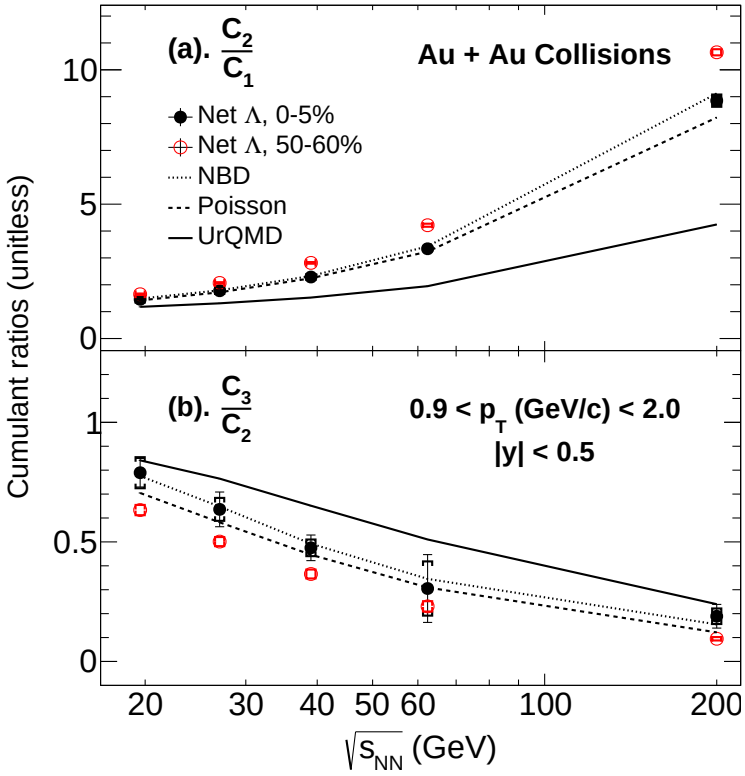

Figure 4.5: Beam-energy dependence of 0-5% and 50-60% central net-Λ cumulant ratios, C_2/C_1 and C_3/C_2 for Au + Au collisions. NBD and Poisson baselines are presented by dashed lines. UrQMD predictions are shown in solid lines. Black vertical lines represent the statistical uncertainties and caps represent the systematic uncertainties. Results were corrected for feed-down contribution and reconstruction efficiency. CBWC was applied.

In Figure 4.5 (b), net-Λ C_3/C_2 in most central (0-5%) and peripheral (50-60%) Au + Au collisions is presented for five collision energies from 19.6 to 200 GeV. The

measured C_3/C_2 values in most central and peripheral collisions decreased monotonically as a function of increasing collision energy and approached zero at 200 GeV. At all collision energies, the C_3/C_2 ratio measured in peripheral collisions stayed below the most central collision measurement. However, the difference of the measured C_3/C_2 ratio in most central collisions and peripheral collisions become small at the highest collision energies (62.4 and 200 GeV). Large statistical uncertainties seen in measured C_3/C_2 were due to the propagation of statistical uncertainties from C_3 and C_2 as explained in Section 3.9. A significantly large statistical uncertainty were seen at 62.4 GeV due to the small sample size. On the other hand, the smallest statistical uncertainties were seen in the C_3/C_2 ratio calculated at 39 and 200 GeV collisions due to the large sample size. The systematic uncertainties were small compared to the statistical uncertainties at all energies and became largest at 62.4 GeV. In the most central collisions, systematic uncertainties became significant relative to the peripheral collisions at all energies.

Both the NBD and Poisson expectations decreased as a function of increasing collision energy and follow the trend in the data. The poisson baseline showed small deviations from data especially at 19.6 and 200 GeV. The NBD expectations stayed closer to the data points at all energies. The Poisson baseline stayed below the NBD expectations at all energies. The NBD expectations can be considered a better approximation for the measured net-Λ C_3/C_2 ratio. Better agreement of the data with NBD could possibly be due to less intra-event correlations between particles and anti-particles. The UrQMD predictions for the C_3/C_2 also followed the same trend as in the data and decreased as a function of increasing collision energy. The UrQMD predictions agreeed with the measured C_3/C_2 ratio at 19.6 and 200 GeV but deviated from data at other energies.

4.5 Comparison of measured net-Λ fluctuations with net-kaon and net-proton results at STAR

The higher order cumulants of net-proton and net-kaon multiplicity distributions have been measured at STAR [21] [31] as proxies for the measurement of net-baryon number and net-strangeness fluctuations, respectively. The measurement of net-Λ cumulant ratios is presented in this analysis in the context of both net-strangeness and net-baryon quantum number fluctuations. Figure 4.6 shows a comparison between the measured net-proton, net-kaon, and net-Λ cumulant ratios C_2/C_1 and C_3/C_2 as a function of collision energy from 19.6 to 200 GeV Au + Au collisions in STAR. The results from the most central collisions (0-5%) are presented. The Poisson baselines are shown for the net-proton and net-kaon measurements while both Poisson and NBD expectations are presented for the net-Λ measurements together with systematic and statistical uncertainties.

As seen in Figure 4.6(a), in the comparison of C_2/C_1 ratio from different fluctuation analyses, all three measurements (net-kaon, net-proton, and net-Λ) followed the same trend and increased as a function of the increasing collision energy. For all collision energies, the net-Λ C_2/C_1 measurement stayed below the net-kaon measurement and above the net-proton measurement. The measured net-Λ C_2/C_1 ratio stayed closer to the net-proton measurement than to the net-kaon measurement. Deviations of the net-kaon and net-proton C_2/C_1 measurements from net-Λ increased as a function of increasing collision energy.

A comparison of C_3/C_2 measurements from the three fluctuation measurement (net-kaon, net-proton and net-Λ) analyses is presented in Figure 4.6(b). Both the

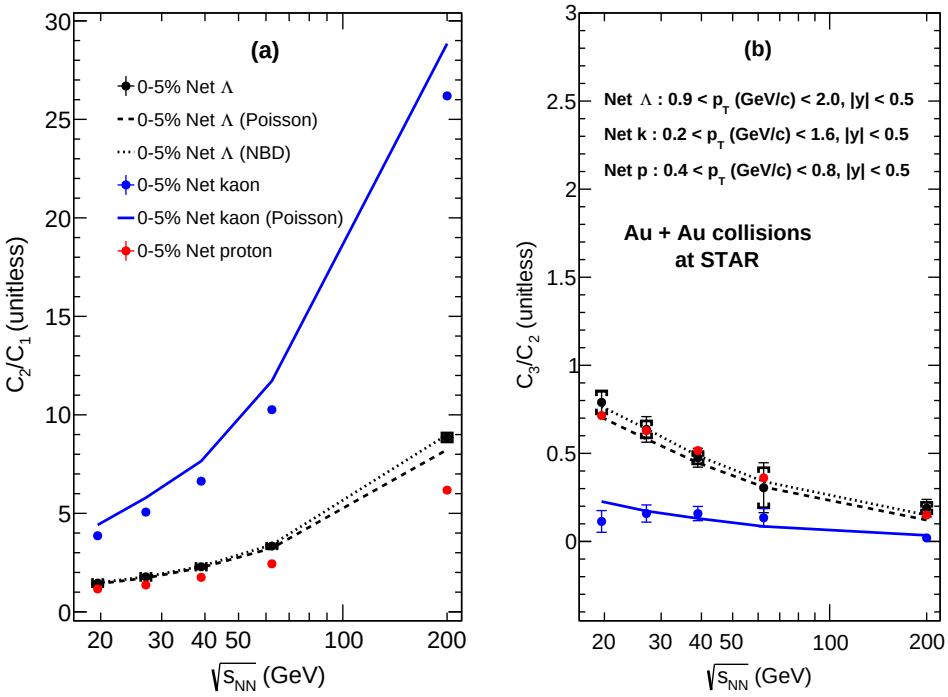

Figure 4.6: Beam-energy dependence of 0-5% central, net-proton [21], net-kaon [31], and net-Λ cumulant ratios, (a). C_2/C_1 and (b). C_3/C_2 from Au + Au collisions. Net-kaon results are presented with Poisson baseline (blue solid line) and net-Λ results are presented with both NBD and Poisson baselines (black dashed lines). Black vertical lines represent the statistical uncertainties and caps represent the systematic uncertainties. Results were corrected for the reconstruction efficiency. CBWC was applied.

Poisson and NBD expectations were shown for the net-Λ measurement, but only the Poisson baseline is shown for the net-proton and net-kaon measurements. The net-Λ C_3/C_2 ratio was consistent with the net proton measurement in all collision centralities within the statistical and systematic uncertainties. Both the net-proton and net-Λ C_3/C_2 ratio decreased monotonically as a function of increasing collision energy while the net-kaon C_3/C_2 ratio showed no dependency on the collision energy. At the highest collision energies (62.4 and 200 GeV) the deviation of net-kaon C_3/C_2 from net-proton and net-Λ measurements become small relative to the measurements at the lowest collision energies.

From the comparisons shown in Figure 4.6, it is observed that the net-Λ results show more consistency with net-proton results than with the net-kaon results. However, only by comparing the experimentally measured values, one can not arrive at a conclusion about the freeze-out conditions associated with them. For a better understanding of the freeze-out process, a comparison between net-Λ fluctuation measurements and HRG predictions are presented and discussed in the next section.

4.6 Comparison of net-Λ fluctuations with predictions form HRG model

Figure 4.7 shows the comparison of measured net-Λ (a); C_2/C_1 and (b); C_3/C_2 ratios for 0-5% central collisions, as a function of collision energy with HRG predictions. The magenta bands show the HRG predictions for net-Λ cumulant ratios calculated at the values of freeze-out temperatures (T_f) and chemical potentials (μ_f) extracted from the fit of net-kaon χ_2/χ_1. The purple bands show the HRG predictions for net-Λ cumulant ratios calculated at the values of T_f and μ_f extracted from the combined fit of net-charge and net-proton χ_2/χ_1 ratios. More details about the HRG calculation can be found in [9] and in Section 3.13.5 of this dissertation.

In the comparison of measured net-Λ C_2/C_1 ratios with HRG predictions in Figure 4.5 (a), it is clear that the measured net-Λ C_2/C_1 ratio is closer to the C_2/C_1 ratio calculated assuming the kaon freeze-out conditions than the proton/charge freeze-out conditions. That is, the deviation of HRG calculations from measured C_2/C_1 ratios become small when the freeze-out conditions extracted considering strange particle fluctuations were used in the prediction. This observation was not trivial to

interpret but one possible explanation is that the strangeness number in Λ baryon plays a more prominent role at the freeze-out than the baryon number. For a complete understanding of this observation, further investigations, both theoretically and experimentally, are necessary.

On the other hand, the measured C_3/C_2 ratios, shown in Fig.4.7(b), seem to indicate less sensitivity to the separate freeze-out conditions. Both HRG curves are very similar over the full range of collision energies and describe the decrease in the cumulant ratio with increasing energy reasonably well. The curve based on the charge/proton freeze-out conditions is insignificantly closer to the data, but as was shown already in [32], ratios that contain higher order moments are prone to be more impacted by dynamical effects and thus lead to more unreliable results when freeze-out parameters are extracted. We therefore focused on the high resolution C_2/C_1 measurement for our conclusions on the chemical T and μ_B at all collision energies.

4.7 Rapidity dependence of net-Λ cumulant ratios

The selection of the appropriate rapidity window is important in fluctuation measurement analysis because it determined the number of particles accepted in the analysis. In general, a full 4π measurement of a conserved quantum number should lead to zero fluctuations, whereas a very small acceptance will always lead to Poisson-like distributions, which means the measurement looses its sensitivity to any kind of non-Poissonian or non-NBD contributions to the fluctuations (see the next section for details). Therefore, it is important to find a rapidity window where a.) the deviation from baselines becomes visible and b.) the effect of the baryon number conservation in the measured distribution can be properly determined and potentially subtracted.

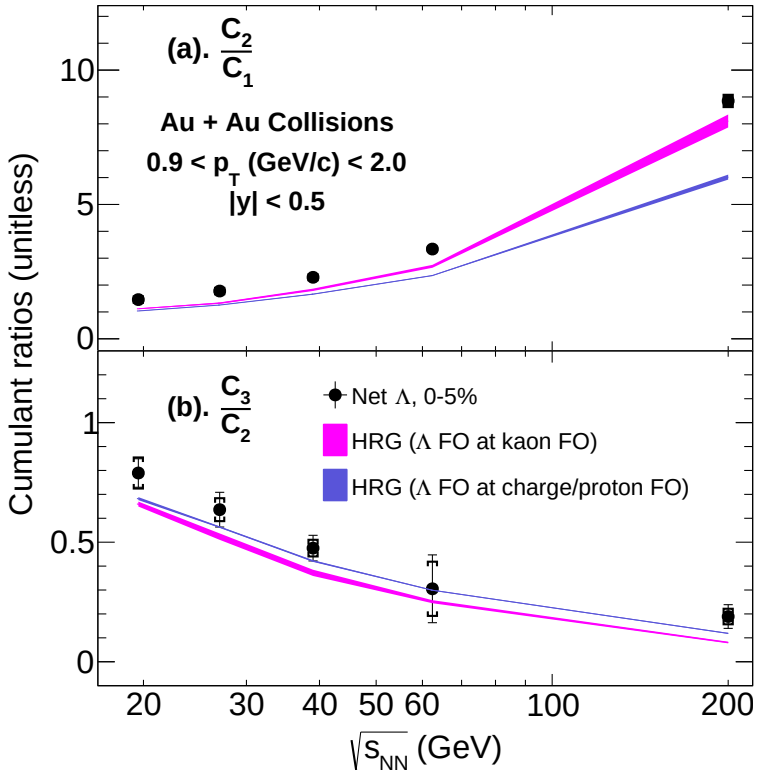

Figure 4.7: Black markers show the beam-energy dependence of measured 0-5% central net-Λ cumulant ratios, (a). C_2/C_1 and (b). C_3/C_2 from Au + Au collisions. Magenta lines show the net-Λ cumulant ratios calculated in HRG [9] assuming Λ Freezes-out (FO) at the same freeze-out conditions as for the kaons. Pink lines show the net-Λ cumulant ratios calculated in HRG [9] assuming Λ freezes-out at the same freeze-out conditions as for the charge/proton freeze-out.

The number of accepted particles also impacts the uncertainty in the measurement. Low statistics lead to large statistical uncertainties and make the interpretation of results difficult. On the other hand, allowing more particles in the analysis may increase the risk of having more impurities and as a result, efficiency could becomes low. In past fluctuation-measurement analyses, a rapidity window of $|y| < 0.5$ was used [21][31] and in the net-Λ fluctuation analysis, the same rapidity window was used for accepting V^0s. With this common rapidity window, the comparison of net-Λ results with net-proton and net-kaon results was done and the results were discussed

in the previous section. The effect of the selected rapidity window on the net-Λ cumulant ratios, C_2/C_1 and C_3/C_2, was studied and results are presented in Figure 4.8. These results are based on 0-5% and 30-40% central collisions at 200 GeV collision energy.

As shown in Figure 4.8 (a), the net-Λ C_2/C_1 ratio decreased as a function of increasing rapidity coverage in both collision centralities. But in 0-5% central C_2/C_1 ratio, the rapidity dependence was negligible within the systematic uncertainties. The deviation of measured net-Λ C_2/C_1 ratios from the NBD baseline increased as a function of increasing rapidity coverage in both centralities. This deviation was mainly due to the deviations of C_2 from NBD expectations and will be discussed in next section. Figure 4.8 (b) shows net-Λ C_3/C_2 dependency on the selected rapidity window. The statistical uncertainty dominates in most central collisions at all rapidity windows. The C_3/C_2 results do not show dependency on the rapidity coverage in both most central and peripheral collisions. The statistical uncertainties associated with the net-Λ C_3/C_2 ratio increased as the rapidity coverage increased. This is because, when the number of particles accepted in the analysis increased, the uncertainty of the cumulants of net particle distributions increased as seen in the statistical uncertainties associated with energy and centrality dependence of net-Λ cumulant ratios. The NBD expectations for C_3/C_2 agree with data in all rapidity windows in the most central collisions while there is a notable deviation from NBD expectations by the data in peripheral collisions (especially at larger rapidity windows).

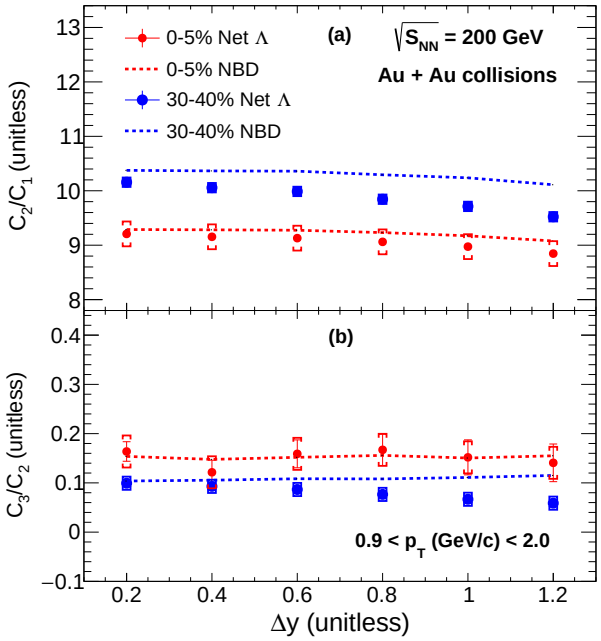

Figure 4.8: Rapidity dependence of 0-5% (in red) and 30-40% (in blue) central net-Λ cumulant ratios, (a). C_2/C_1 and (b). C_3/C_2 from 200 GeV Au + Au collisions. Dashed lines show the NBD expectations. Vertical error bars represent the statistical uncertainties and caps represent the systematic uncertainties. Results are corrected for reconstruction efficiency and CBWC is applied.

4.8 Rapidity dependence of $C_{2(\Lambda-\bar{\Lambda})}/C_{2(NBD)}$ ratio

Net-particle multiplicity fluctuations are predicted in HRG and LQCD models according to the grand canonical ensemble (GCE) formulation in thermodynamics. In the GCE formulation, net quantum numbers such as the net-baryon number and the net-strangeness are not conserved in each micro state which makes conserved quantum numbers fluctuate. In experiments, conserved quantum numbers fluctuate in-and-out of a certain acceptance window. Acceptance windows such as finite rapidity and transverse momentum (p_T) of the detected particles mirror the requirements of GCE in the experiment. This allows the comparison between the experimentally measured cumulant ratios and their theoretical predictions.

However, if the acceptance window is too small, then statistical fluctuations will be dominant, but important dynamical fluctuations may possibly be suppressed [33]. That is, at smaller-acceptance windows, net-particle multiplicity distributions will be equal to the difference of individual particle distributions, which is known as the Skellam distribution. On the other hand, if the experiment has a large enough acceptance, dynamical fluctuations will be dominant over the statistical fluctuations as long as the effect of baryon number conservation can be subtracted in order to observe important correlations because of baryon-number conservation.

A quantitative determination of the optimal acceptance window can be done by considering the acceptance factor α_{acc} and by modeling the finite acceptance following a binomial distribution. The acceptance factor, α_{acc} is defined as

$$\alpha_{acc} = \frac{\langle N_B^{acc} \rangle}{\langle N_B^{4\pi} \rangle} \tag{4.1}$$

Here, $\langle N_B^{acc} \rangle$ represents the number of detected baryons and $\langle N_B^{4\pi} \rangle$ is the number of baryons in the full-phase space. The binomial-distribution function is

$$B\left(n_B; N_B, \alpha_{acc}\right) = \frac{N_B!}{n_B!\left(N_B - n_B\right)!} \alpha_{acc}^{n_B} (1 - \alpha_{acc})^{N_B - n_B} \tag{4.2}$$

If the number of baryons are distributed according to a probability $P(N_B)$ across the whole 4π space, then the corresponding multiplicity distribution in a given acceptance $P(n_B)$ can be expressed as

$$P\left(n_B\right) = \sum_{N_B} B\left(n_B; N_B, \alpha_{acc}\right) P\left(N_B\right) \tag{4.3}$$

Following the formulation in Equation 4.3, moments of measured multiplicity distributions can be calculated. According to the method described in [34] the second

order measured cumulant with respect to the Skellam expectation for the second order cumulant is given by

$$\frac{C_2\left(n_B - n_{\overline{B}}\right)}{C_2(Skellam)} = 1 - \alpha_{acc} \tag{4.4}$$

The sensitivity of the net-Λ fluctuation measurements to the dynamical fluctuations can be addressed using the relationship in Equation 4.4. The NBD expectations showed a better agreement with the net-Λ fluctuation measurements as discussed in the previous sections of this chapter. Therefore, the NBD expectations were used, instead of the Skellam baseline, for the estimation of deviations of measured net-Λ C_2 from the baseline as a function of rapidity. Net-Λ, $C_{2\left(\Lambda-\overline{\Lambda}\right)}/C_{2(NBD)}$ values were calculated in the 0-5% most central collisions for three different collision energies (a) 19.6 GeV, (b) 39 GeV, (c) 200 GeV and the results are shown in Figure 4.9. At all three collision energies, the measured C_2 values stay above the baseline expectations and the deviations became larger as the rapidity window increased. This observation is consistent with the relationship shown in Equation 4.4. The rapidity window used in this analysis is $|y| < 0.5$ and in this rapidity window, measured C_2 has a clear deviation ($\sim 2 - 3\%$) from the NBD baseline. This deviation is likely due to the fact that net-Λ fluctuations show sensitivity to the baryon-number conservation as explained in [34].

As the collision energy increased, the rapidity range in which the detected particles are distributed became larger compared to the range of the distribution of particles at low energies. Therefore, according to Equation 4.1, for a fixed rapidity window, α_{acc} decreased as a function of increasing collision energy. As a result, at a fixed rapidity window, the deviation of measured C_2 from the baseline expectation should decrease as a function of increasing collision energy. However, as seen

in Figure 4.9, the deviation of measured C_2 from the baseline stayed approximately equal ($\sim 2-3\%$) and did not decrease as the collision energy increased. This may be because the Λ baryon was not the only contributor to the baryon-number. Also, because the NBD baseline was constructed using both mean and variance of individual particle distributions. There could be a possibility of NBD expectations not showing similar behaviour as when the Skellam baselines were used. However, this matter should be further investigated.

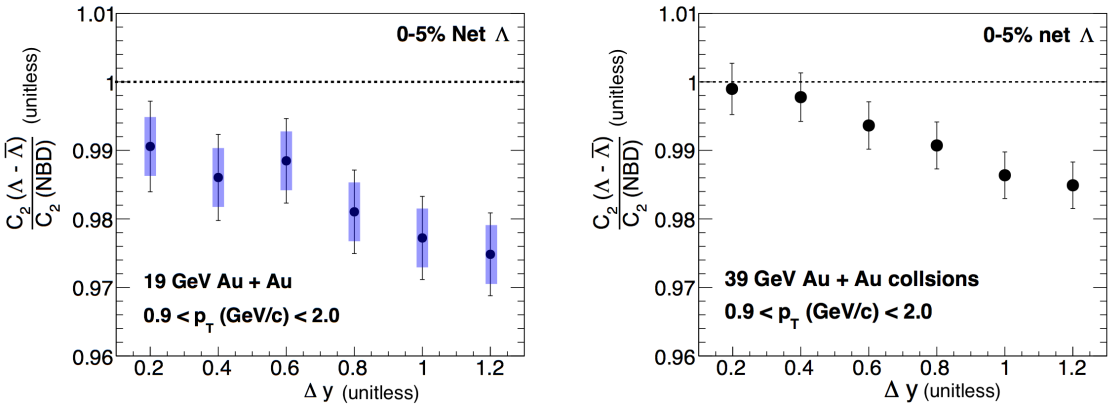

Figure 4.9: Rapidity-dependence of net-Λ C_2 with respect to the NBD expectation in 0-5% central collisions at (a). 19 GeV, (b). 39 GeV, and (c) 200 GeV Au + Au collisions. Results are corrected for the reconstruction efficiency and CBWC applied. Black vertical lines show statistical uncertainties and light blue rectangles show systematic uncertainties.

Chapter 5

Summary

The study of the characteristics of the QCD-phase transition provides important information about strongly interacting matter and the way it evolves as a function of temperature and chemical potential. During heavy-ion collisions at STAR, strongly interacting matter called QGP was created and was analyzed in order to explore the initial stages of hot and dense quark matter. The identified net-particle multiplicity distributions were used as proxies for the net quantum-number fluctuations. Their sensitivity to the correlation length provided possible clues about the QCD critical point. The relationship of fluctuations of the conserved quantum numbers with the susceptibilities of the medium produced in heavy-ion collisions provides information about the freeze-out parameters (temperature and chemical potential) at the QCD-phase transition.

Regarding the search for the QCD critical point, the net-Λ fluctuations do not provide sufficient information because, a.) the C_2/C_1 ratio was not sensitive to the critical point, b.) the C_3/C_2 and the C_4/C_2 measurements were not sensitive due

insufficient statistics. Furthermore, the reduced Λ production at energies below 19.6 GeV, where the effect of critical fluctuations seems strongest based on the STAR net proton results, prohibited any detailed analysis at these energies.

Information about the shapes of net particle multiplicity distributions are reflected by the calculated higher order cumulants. The volume-independent cumulant ratios were related to relevant ratios of the susceptibilities of conserved quantum numbers. The LQCD and HRG models have been successfully used in predicting the freeze-out parameters by comparing the theoretically modeled susceptibilities with the experimentally measured cumulants of net-particle multiplicity distributions. Furthermore, thermal fits to the measured particle yields or ratios of the particles yields can also be used to extract the freeze-out parameters. In the previous fluctuation analyses at STAR, net-charge particles, net-protons, and net-kaons have been used as proxies for the net-charge, net-baryon number, and net-strangeness quantum number fluctuations, respectively. Theoretical predictions and comparisons of the experimental measurements with the theory, showed that there could be a possibility of flavor hierarchy in the process of hadronization. Specifically, the extracted freeze-out curve for strange particles points to a freeze-out temperature higher than that of the particles that consist of light quarks. This observation was studied using the existing net-kaon fluctuation measurements at STAR in the context of net-strangeness fluctuations. In this analysis, the first measurement of net-Λ fluctuations was presented in the context of both baryon number and strangeness fluctuations. The net-Λ together with net-kaon fluctuation measurement provides a more complete net strangeness measurement. On the other hand, net-Λs together with net-protons provide more complete set of the baryon number. In addition, net-Λ measurements can be used for the verification of predicted sequential hadronization.

The heavy-ion collisions that take place at RHIC with variable collision energies provide the data needed for the exploration of different regions of the QCD-phase diagram. The excellent tracking capabilities of the STAR TPC detector provide the information needed for the charged particle identification. The STAR TPC was used for the identification of protons and pions for the reconstruction of invariant mass of the Λ baryon. The purity of the reconstructed V^0 (Λ or $\overline{\Lambda}$) was enhanced ($> 90\%$) by optimizing topological cuts. The efficiency corrected and feed-down corrected net-Λ single cumulants (C_1, C_2, and C_3) and cumulant ratios, C_2/C_1 and C_3/C_2, were calculated for five Au + Au collision energies from 19.6 to 200 GeV. The results were presented as a function of collision centrality, energy, and rapidity.

Several important steps were taken in the analysis procedure in order to investigate the effects of a.) transverse-momentum dependency on the efficiency correction, b.) feed-down correction, c.) centrality bin-width correction. Two methods (p_T-independent and p_T-dependent) were used for the efficiency correction and results from both methods were consistent in the most central collisions of single cumulants and cumulant ratios. Since there was a possibility of contamination due to Λ baryons coming from multi-strange weak decays, the feed-down correction was performed. The single cumulants were increased after the feed-down correction but the cumulant ratios were not affected. To eliminate the volume fluctuation effects, a centrality bin-width correction was applied to the final results. However, the effect of centrality bin-width correction was negligible. The analysis was done in the transverse momentum range: $0.9 < p_T\ (GeV/c) < 2.0$, and in a rapidity window: $|y| < 0.5$, where the statistics of the sample and the V^0 reconstruction efficiency became reasonable. The results were presented with statistical and systematic uncertainties.

The net-Λ single cumulants (C_1, C_2, and C_3) increased as a function of increasing

collision centrality due to the large number of participant nucleons in most central collisions than in the peripheral collisions. This trend is in accordance with the Poisson and the NBD expectations. The net-Λ cumulant ratios, C_2/C_1 and C_3/C_2, showed a weak dependence on the collision centrality and this behaviour was also in accordance with Poisson and NBD expectations. The UrQMD predictions deviate from C_2/C_1, but in C_3/C_2 the deviation was relatively small. The net-Λ C_2/C_1 ratio measurements increase monotonically as a function of increasing collision energy in most central and peripheral collisions as expected by the NBD and the Poisson baselines. Deviation of the UrQMD predictions for C_2/C_1 increased as a function of increasing collision energy. The net-Λ C_3/C_2 ratio decreased as a function of increasing collision energy and approached zero at 200 GeV in most central and peripheral collisions. The UrQMD predictions for C_3/C_2 showed agreement at 200 GeV and 19.6 GeV but deviate in other energies.

The net-Λ cumulant ratios were compared to the HRG calculations based on different freeze-out conditions. The HRG predictions were able to describe the monomaniacal increase and the decrease in C_2/C_1 and C_3/C_2, respectively, as a function of increasing collision energy. The measured net-Λ C_2/C_1 ratio was closer to the C_2/C_1 ratio calculated assuming the kaon freeze-out conditions than the proton/charge freeze-out conditions. This observation could be due to the strangeness number in Λ baryon plays a more prominent role at the freeze-out than the baryon number. The measured higher order cumulant ratio, C_3/C_2, showed less sensitivity to the separate freeze-out conditions which could possibly be due to the contributions from dynamical effects.

The net-Λ C_2/C_1 ratio showed a weak dependence on the rapidity window while the C_3/C_2 ratio showed no dependence. The deviation of the NBD expectation

of net-Λ C_2 values from measured net-Λ C_2 values was studied as a function of rapidity window for 19.6, 39, and 200 GeV most central collisions. At all energies, the deviation increased as a function of increasing rapidity window which could be possibly due to the effects of baryon-number conservation. However, for a given rapidity, the deviation of the NBD baseline from measured C_2 remained similar ($\sim$ 2 - 3%) for all energies (19.6, 39, and 200 GeV). This observation was not expected as a consequence of baryon number conservation and should be further investigated.

Appendix A

Appendix: Centrality classes and data tables

A.1 Centrality classes

Table A.1: Average number of participant nucleons ($\langle N_{part} \rangle$) and RefMult3 lower bound associated with nine centrality classes (0-5% to 70-80%) for five Au + Au collision energies; 19.6, 27, 39, 62.4 and 200 GeV.

$\sqrt{s_{NN}}$ \ Centrality		0-5%	5-10%	10-20%	20-30%	30-40%	40-50%	50-60%	60-70%	70-80%
200 GeV,	$\langle N_{part} \rangle$	349.67	302.22	237.26	169.02	116.73	76.93	47.21	27.43	14.96
	RefMult3	> 725	> 618	> 440	> 301	> 196	> 120	> 67	> 34	> 16
62.4 GeV,	$\langle N_{part} \rangle$	344.4	296.71	232.08	164.59	113.49	75.08	46.26	26.56	13.78
	RefMult3	> 571	> 482	> 338	> 230	> 149	> 91	> 51	> 26	> 12
39 GeV,	$\langle N_{part} \rangle$	341.76	291.95	227.72	160.87	110.54	72.86	45.25	26.23	17.96
	RefMult3	> 522	> 439	> 308	> 209	> 136	> 83	> 47	> 24	> 11
27 GeV,	$\langle N_{part} \rangle$	340.96	291.78	227.42	167.17	110.87	72.93	45.43	26.06	13.43
	RefMult3	> 490	> 412	> 289	> 196	> 127	> 78	> 44	> 22	> 10
19.6 GeV,	$\langle N_{part} \rangle$	340.67	293.93	232.41	167.02	117.86	79.93	51.21	31.43	17.96
	RefMult3	> 448	> 376	> 263	> 178	> 116	> 71	> 40	> 20	> 9

A.2 Data tables - 200 GeV

Table A.2: The Single cumulants (C_1, C_2, C_3), cumulant ratios (C_2/C_1, C_3/C_2), statistical uncertainties, systematic uncertainties, baseline expectation (NBD, Poisson) and UrQMD predictions for 200 GeV Au + Au collisions.

Cum. \ Cent.		70-80%	60-70%	50-60%	40-50%	30-40%	20-30%	10-20%	5-10%	0-5%
C_1,	val.	0.0067	0.0163	0.0372	0.0728	0.1365	0.2362	0.3901	0.5776	0.7433
	±stat.	0.00020	0.00026	0.0006	0.0010	0.0020	0.0038	0.0067	0.0100	0.0121
	±sys.	0.0012	0.0028	0.0066	0.0128	0.0248	0.0452	0.0804	0.1327	0.1890
	NBD	0.0067	0.0163	0.0372	0.0728	0.1365	0.2362	0.3901	0.5776	0.7433
	Poi.	0.0067	0.0163	0.0372	0.0728	0.1365	0.2362	0.3901	0.5776	0.7433
	UrQ.	0.0015	0.0056	0.0164	0.0426	0.0968	0.2008	0.3870	0.6103	0.8504
C_2,	val.	0.0764	0.1778	0.3965	0.7475	1.3434	2.2271	3.5513	5.1258	6.5802
	±stat.	0.0006	0.0012	0.0028	0.0055	0.0108	0.0209	0.0440	0.0702	0.0747
	±sys.	0.0102	0.0282	0.0673	0.1298	0.2461	0.4340	0.7645	1.2636	1.8574
	NBD	0.0776	0.1811	0.4060	0.7676	1.3865	2.3140	3.7055	5.2852	6.6846
	Poi.	0.0773	0.1804	0.4018	0.7573	1.3551	2.2261	3.4901	4.9028	6.1174
	UrQ.	0.0327	0.0765	0.1647	0.3315	0.6221	1.1023	1.8705	2.7318	3.5926
C_3,	val.	0.0068	0.0165	0.0376	0.0756	0.1481	0.2922	0.5189	0.6420	1.2443
	±stat.	0.0005	0.0006	0.0020	0.0046	0.0114	0.0247	0.0630	0.1791	0.3701
	±sys.	0.0009	0.0018	0.0035	0.0083	0.0157	0.0224	0.0539	0.1400	0.4401
	NBD	0.0067	0.0165	0.0386	0.0774	0.1510	0.2995	0.5010	0.7710	1.0015
	Poi.	0.0067	0.0163	0.0372	0.0728	0.1365	0.2362	0.3901	0.5776	0.7433
	UrQ.	0.0016	0.0055	0.0162	0.0403	0.0955	0.1999	0.3793	0.6142	0.8630
C_2/C_1,	val.	11.3914	10.8562	10.6522	10.2583	9.8393	9.4257	9.1030	8.8744	8.8521
	±stat.	0.2840	0.1022	0.1070	0.0817	0.0719	0.0788	0.0574	0.0541	0.0658
	±sys.	0.3551	0.1802	0.1142	0.0810	0.0867	0.0756	0.1086	0.1521	0.2282
	NBD	11.5808	11.0588	10.9081	10.5338	10.1546	9.79322	9.49832	9.15028	8.99271
	Poi.	11.5352	11.0156	10.7940	10.3919	9.9248	9.4213	8.9461	8.4883	8.2296
	UrQ.	31.1348	14.3372	10.4619	7.9371	6.5258	5.5472	4.8646	4.4895	4.2436
C_3/C_2,	val.	0.0891	0.0928	0.0948	0.1012	0.1102	0.1312	0.1461	0.1252	0.1891
	±stat.	0.0061	0.0033	0.0043	0.0051	0.0073	0.0093	0.0147	0.0289	0.0495
	±sys.	0.0036	0.0077	0.0071	0.0153	0.0134	0.0151	0.0144	0.0201	0.0325
	NBD	0.0863	0.0914	0.0950	0.1009	0.1089	0.1294	0.1352	0.1458	0.1498
	Poi.	0.0866	0.0907	0.0926	0.0962	0.1007	0.1061	0.1117	0.1178	0.1215
	UrQ.	0.0462	0.0701	0.0972	0.1210	0.1517	0.1803	0.2021	0.2243	0.2395

A.3 Data tables - 62.4 GeV

Table A.3: Single cumulants (C_1, C_2, C_3), cumulant ratios (C_2/C_1, C_3/C_2), statistical uncertainties, systematic uncertainties, baseline expectation (NBD, Poisson) and UrQMD predictions for 62.4 GeV Au + Au collisions.

Cum. \ Cent.		70-80%	60-70%	50-60%	40-50%	30-40%	20-30%	10-20%	5-10%	0-5%
C_1,	val.	0.0112	0.0304	0.0657	0.1321	0.2675	0.4556	0.7785	1.1351	1.5257
	±stat.	0.0004	0.0010	0.0022	0.0010	0.0026	0.0032	0.0053	0.0076	0.0130
	±sys.	0.0021	0.0056	0.0122	0.0235	0.0484	0.0843	0.1476	0.2285	0.3429
	NBD	0.0112	0.0304	0.0657	0.1321	0.2675	0.4556	0.7785	1.1351	1.5257
	Poi.	0.0112	0.0304	0.0657	0.1321	0.2675	0.4556	0.7785	1.1351	1.5257
	UrQ.	0.0032	0.0100	0.0292	0.0722	0.1589	0.3242	0.6173	0.9746	1.3680
C_2,	val.	0.0515	0.1371	0.2773	0.5299	1.0098	1.6489	2.7047	3.8688	5.0963
	±stat.	0.0008	0.0015	0.0014	0.0021	0.0058	0.0122	0.0112	0.0313	0.1331
	±sys.	0.0057	0.0202	0.0448	0.0882	0.1727	0.2962	0.5072	0.7992	1.2084
	NBD	0.0523	0.1396	0.2815	0.5398	1.0357	1.6919	2.7750	3.9223	5.1959
	Poi.	0.0521	0.1390	0.2792	0.5322	1.0172	1.6520	2.6714	3.7329	4.9323
	UrQ.	0.0172	0.0410	0.0939	0.1996	0.3928	0.7327	1.3004	1.9660	2.6606
C_3,	val.	0.0110	0.0305	0.06389	0.1381	0.2858	0.5196	0.9624	1.7162	1.5548
	±stat.	0.0012	0.0024	0.0067	0.0086	0.0310	0.0581	0.1753	0.2976	0.8326
	±sys.	0.0011	0.0034	0.0057	0.0153	0.0196	0.0552	0.0772	0.4229	0.8806
	NBD	0.0107	0.0311	0.0676	0.1410	0.2953	0.5070	0.9220	1.3755	1.7692
	Poi.	0.0112	0.0304	0.0657	0.1321	0.2675	0.4556	0.7785	1.1351	1.5257
	UrQ.	0.0032	0.0100	0.0286	0.0730	0.1594	0.3241	0.6136	0.9754	1.3588
C_2/C_1,	val.	4.5893	4.5004	4.2160	4.0100	3.7741	3.6189	3.4740	3.4081	3.3401
	±stat.	0.1452	0.1509	0.1878	0.0258	0.0280	0.0309	0.0234	0.0346	0.0694
	±sys.	0.2650	0.1063	0.0564	0.0268	0.0237	0.0152	0.0174	0.0285	0.0531
	NBD	4.6636	4.5815	4.2799	4.0852	3.8707	3.7133	3.5643	3.4553	3.4054
	Poi.	4.6430	4.5642	4.2457	4.0275	3.8015	3.6258	3.4312	3.2884	3.2326
	UrQ.	5.5873	4.2061	3.2731	2.7945	2.4893	2.2687	2.1146	2.0200	1.9475
C_3/C_2,	val.	0.2152	0.2227	0.2303	0.2606	0.2830	0.3151	0.3558	0.4436	0.3050
	±stat.	0.0187	0.0156	0.0210	0.0138	0.0271	0.0303	0.0556	0.0655	0.1417
	±sys.	0.0244	0.0207	0.0215	0.0197	0.0359	0.0348	0.0471	0.0420	0.1133
	NBD	0.2057	0.2228	0.2403	0.2612	0.2851	0.2996	0.3322	0.3506	0.3405
	Poi.	0.2153	0.21909	0.2355	0.2482	0.2630	0.2757	0.2914	0.3040	0.3093
	UrQ.	0.1831	0.2411	0.3014	0.3620	0.4034	0.4405	0.4701	0.4962	0.5101

A.4 Data tables - 39 GeV

Table A.4: Single cumulants (C_1, C_2, C_3), cumulant ratios (C_2/C_1, C_3/C_2), statistical uncertainties, systematic uncertainties, baseline expectation (NBD, Poisson) and UrQMD predictions for 39 GeV Au + Au collisions.

Cum. \ Cent.		70-80%	60-70%	50-60%	40-50%	30-40%	20-30%	10-20%	5-10%	0-5%
C_1,	val.	0.0133	0.0363	0.0786	0.1647	0.3116	0.5521	0.9133	1.2898	1.7370
	±stat.	0.00019	0.00021	0.00026	0.0003	0.0006	0.0009	0.0019	0.0032	0.0099
	±sys.	0.0024	0.0066	0.0137	0.0292	0.0559	0.1018	0.1732	0.2532	0.3666
	NBD	0.0133	0.0363	0.0786	0.1647	0.3116	0.5521	0.9133	1.2898	1.7370
	Poi.	0.0133	0.0363	0.0786	0.1647	0.3116	0.5521	0.9133	1.2898	1.7370
	UrQ.	0.0043	0.0137	0.0364	0.0886	0.1945	0.3929	0.7537	1.1996	1.6881
C_2,	val.	0.0404	0.1065	0.2212	0.4448	0.8021	1.3629	2.1699	2.9846	3.9753
	±stat.	0.0002	0.0003	0.0006	0.0012	0.0016	0.0031	0.0081	0.0132	0.0325
	±sys.	0.0044	0.0154	0.0347	0.0741	0.1379	0.2445	0.4078	0.5954	0.8619
	NBD	0.0411	0.1082	0.2244	0.4522	0.8155	1.3861	2.2087	3.0094	4.0210
	Poi.	0.0410	0.1079	0.2232	0.4470	0.8045	1.3618	2.1500	2.9361	3.8912
	UrQ.	0.0144	0.0356	0.0817	0.1777	0.3577	0.6771	1.2280	1.8845	2.5702
C_3,	val.	0.0136	0.0375	0.0809	0.1750	0.3329	0.6082	1.0035	1.3594	1.8891
	±stat.	0.0003	0.0006	0.0012	0.0034	0.0073	0.0127	0.0365	0.0843	0.2438
	±sys.	0.0017	0.0051	0.0076	0.0162	0.0305	0.0502	0.0834	0.1613	0.4248
	NBD	0.0135	0.0368	0.0814	0.1746	0.3333	0.6007	1.0278	1.4226	1.9567
	Poi.	0.0133	0.0363	0.0786	0.1647	0.3116	0.5521	0.9133	1.2898	1.7370
	UrQ.	0.0044	0.0137	0.0366	0.0883	0.1956	0.3942	0.7588	1.1944	1.6777
C_2/C_1,	val.	3.0234	2.9289	2.8146	2.7006	2.5737	2.4684	2.3757	2.3140	2.2886
	±stat.	0.0274	0.0158	0.0075	0.0053	0.0079	0.0041	0.0054	0.0062	0.0109
	±sys.	0.1773	0.0751	0.0302	0.0182	0.0118	0.0079	0.0113	0.0154	0.0266
	NBD	3.0773	2.9757	2.8549	2.7457	2.6165	2.5104	2.4182	2.3332	2.3149
	Poi.	3.0673	2.9671	2.8395	2.7144	2.5814	2.4665	2.3540	2.27641	2.2401
	UrQ.	3.3823	2.6412	2.2699	2.0201	1.8468	1.7304	1.6335	1.5723	1.5238
C_3/C_2,	val.	0.3363	0.3524	0.3657	0.3936	0.4150	0.4462	0.4624	0.4554	0.4752
	±stat.	0.0067	0.0051	0.0045	0.0060	0.0078	0.0080	0.0142	0.0253	0.0535
	±sys.	0.0242	0.0090	0.0186	0.0210	0.0260	0.0365	0.0513	0.0356	0.0347
	NBD	0.3299	0.3409	0.3629	0.3861	0.4087	0.4334	0.4653	0.4727	0.4866
	Poi.	0.3260	0.3370	0.3521	0.3684	0.3873	0.4054	0.4248	0.4392	0.4463
	UrQ.	0.3038	0.3790	0.4444	0.4942	0.5443	0.5798	0.6170	0.6332	0.6513

A.5 Data tables - 27 GeV

Table A.5: Single cumulants (C_1, C_2, C_3), cumulant ratios (C_2/C_1, C_3/C_2), statistical uncertainties, systematic uncertainties, baseline expectation (NBD, Poisson) and UrQMD predictions for 27 GeV Au + Au collisions.

Cum. \ Cent.		70-80%	60-70%	50-60%	40-50%	30-40%	20-30%	10-20%	5-10%	0-5%
C_1,	val.	0.0177	0.0513	0.1201	0.2661	0.4849	0.8602	1.3932	2.0273	2.5788
	±stat.	0.0002	0.0004	0.0006	0.0007	0.0008	0.0010	0.0017	0.0025	0.0044
	±sys.	0.0021	0.0059	0.0131	0.0301	0.0541	0.0987	0.1656	0.2591	0.3646
	NBD	0.0177	0.0513	0.1201	0.2661	0.4849	0.8602	1.3932	2.0273	2.5788
	Poi.	0.0177	0.0513	0.1201	0.2661	0.4849	0.8602	1.3932	2.0273	2.5788
	UrQ.	0.0061	0.0160	0.0425	0.1025	0.2249	0.4549	0.8770	1.4068	1.9864
C_2,	val.	0.0388	0.1105	0.2484	0.5311	0.9279	1.5868	2.5178	3.6125	4.5832
	±stat.	0.0002	0.0006	0.0010	0.0022	0.0039	0.0064	0.0092	0.0137	0.0570
	±sys.	0.0026	0.0087	0.0225	0.0541	0.0964	0.1727	0.2936	0.4637	0.6663
	NBD	0.0393	0.1125	0.2526	0.5399	0.9434	1.6214	2.5652	3.6466	4.6007
	Poi.	0.0391	0.1113	0.2505	0.5319	0.9276	1.5814	2.4783	3.5266	4.4325
	UrQ.	0.0137	0.0320	0.0758	0.1670	0.3428	0.6571	1.2135	1.8906	2.5994
C_3,	val.	0.0177	0.0525	0.1245	0.2804	0.5281	0.9380	1.7153	2.5739	2.9150
	±stat.	0.0003	0.0015	0.0044	0.0076	0.0147	0.0265	0.0630	0.2148	0.3773
	±sys.	0.0014	0.0027	0.0061	0.01452	0.0308	0.0554	0.1043	0.2892	0.3061
	NBD	0.0176	0.0535	0.1253	0.2838	0.5226	0.9484	1.6124	2.3097	2.9409
	Poi.	0.0177	0.0513	0.1201	0.2661	0.4849	0.8602	1.3932	2.0273	2.5788
	UrQ.	0.0061	0.0161	0.0427	0.1032	0.2265	0.4568	0.8812	1.4016	1.9901
C_2/C_1,	val.	2.1855	2.1513	2.0678	1.9956	1.9135	1.8445	1.8072	1.7819	1.7772
	±stat.	0.0205	0.0135	0.0089	0.0106	0.0059	0.0060	0.0062	0.0054	0.02018
	±sys.	0.1586	0.0647	0.0283	0.01588	0.0113	0.0094	0.0087	0.0127	0.0137
	NBD	2.2155	2.1895	2.1032	2.0286	1.9456	1.8848	1.8412	1.7987	1.7840
	Poi.	2.2067	2.1664	2.0854	1.9987	1.9129	1.8384	1.7789	1.7395	1.7188
	UrQ.	2.2611	2.0198	1.7932	1.6367	1.5300	1.4484	1.3868	1.3445	1.3097
C_3/C_2,	val.	0.4573	0.4752	0.5013	0.5279	0.5691	0.5911	0.6812	0.7125	0.6360
	±stat.	0.0076	0.0118	0.0143	0.0120	0.0135	0.0146	0.0209	0.0532	0.0725
	±sys.	0.0639	0.0189	0.0189	0.0359	0.0461	0.0555	0.05396	0.02460	0.0479
	NBD	0.4480	0.4759	0.4960	0.5256	0.5539	0.5849	0.6285	0.6333	0.6392
	Poi.	0.4531	0.4615	0.4795	0.5003	0.5227	0.5439	0.5621	0.5748	0.5817
	UrQ.	0.4474	0.4984	0.5603	0.6149	0.6568	0.6935	0.7228	0.7404	0.7645

A.6 Data tables - 19.6 GeV

Table A.6: Single cumulants (C_1, C_2, C_3), cumulant ratios (C_2/C_1, C_3/C_2), statistical uncertainties, systematic uncertainties, baseline expectation (NBD, Poisson) and UrQMD predictions for 19.6 GeV Au + Au collisions.

Cum. \ Cent.		70-80%	60-70%	50-60%	40-50%	30-40%	20-30%	10-20%	5-10%	0-5%
C_1,	val.	0.0148	0.0457	0.1139	0.2216	0.4497	0.7709	1.2907	1.8051	2.6104
	±stat.	0.0003	0.0008	0.0017	0.0026	0.0059	0.0089	0.0145	0.0208	0.0285
	±sys.	0.0026	0.0083	0.0205	0.0379	0.0801	0.1369	0.2342	0.3354	0.5178
	NBD	0.0148	0.0457	0.1139	0.2216	0.4497	0.7709	1.2907	1.8051	2.6104
	Poi.	0.0148	0.0457	0.1139	0.2216	0.4497	0.7709	1.2907	1.8051	2.6104
	UrQ.	0.0074	0.0191	0.0489	0.1152	0.2520	0.5147	0.9958	1.6017	2.2515
C_2,	val.	0.0256	0.0770	0.1877	0.3506	0.6901	1.1663	1.9238	2.6006	3.8084
	±stat.	0.0003	0.0015	0.0023	0.0046	0.0084	0.0131	0.0215	0.0340	0.0483
	±sys.	0.0025	0.0102	0.0294	0.0563	0.1176	0.2015	0.3438	0.4837	0.7677
	NBD	0.0259	0.0779	0.1901	0.3547	0.6990	1.1816	1.9476	2.6235	3.8527
	Poi.	0.0258	0.0778	0.1881	0.3516	0.6927	1.1572	1.8851	2.5896	3.7044
	UrQ.	0.0130	0.0306	0.0731	0.1611	0.3361	0.6588	1.2289	1.9282	2.6514
C_3,	val.	0.0149	0.0461	0.1188	0.2290	0.4551	0.8340	1.5174	1.9039	3.0062
	±stat.	0.0005	0.0016	0.0037	0.0055	0.0175	0.0214	0.0843	0.1576	0.2704
	±sys.	0.0023	0.0053	0.0142	0.0247	0.0332	0.0596	0.0978	0.2639	0.2896
	NBD	0.0149	0.0461	0.1194	0.2260	0.4676	0.8356	1.4694	1.8985	2.9519
	Poi.	0.0148	0.0457	0.1139	0.2216	0.4497	0.7709	1.2907	1.8051	2.6104
	UrQ.	0.0074	0.0190	0.0491	0.1146	0.2521	0.5164	1.0002	1.6073	2.2308
C_2/C_1,	val.	1.7284	1.6836	1.6473	1.5822	1.5346	1.5128	1.4905	1.4406	1.4589
	±stat.	0.0261	0.0157	0.0146	0.0103	0.0072	0.0064	0.0064	0.0111	0.0107
	±sys.	0.1525	0.0597	0.0264	0.0122	0.0094	0.0078	0.0089	0.0075	0.0123
	NBD	1.7516	1.7033	1.6683	1.6006	1.5544	1.5327	1.5089	1.4533	1.4758
	Poi.	1.7467	1.6991	1.6502	1.5866	1.5403	1.5011	1.4605	1.4345	1.4191
	UrQ.	1.7800	1.6204	1.5031	1.4031	1.3375	1.2828	1.2363	1.2043	1.1785
C_3/C_2,	val.	0.5850	0.5992	0.6331	0.6532	0.6594	0.7151	0.7887	0.7320	0.7893
	±stat.	0.0152	0.0132	0.0151	0.0101	0.0216	0.0183	0.0358	0.0494	0.0596
	±sys.	0.1575	0.0222	0.0214	0.0284	0.0591	0.0721	0.0671	0.0374	0.0649
	NBD	0.5769	0.5917	0.6280	0.6371	0.6689	0.7071	0.7544	0.7236	0.7661
	Poi.	0.5724	0.5885	0.6059	0.6302	0.6491	0.6661	0.6846	0.6970	0.7046
	UrQ.	0.5663	0.6172	0.6675	0.7094	0.7478	0.7824	0.8127	0.8331	0.8411

Bibliography

[1] J. P. Uzan, "The big-bang theory: Construction, evolution and status," *Sminaire Poincar*, 2016. arXiv.1606.06112[astro-ph.CO].

[2] M. Gyulassy, "The QGP discovered at RHIC," in *Structure and Dynamics of Elementary Matter* (W. Greiner, M. Itkis, J. Reinhardt, and M. Guclu, eds.), vol. 166 of *NATO Science Series (Series II: Mathematics, Physics and Chemistry)*, Dordrecht,The Netherlands: Kluwer Academic Publisher, 2004.

[3] S. Bethke, "Experimental tests of asymptotic freedom," *Progress in Particle and Nuclear Physics*, vol. 58, no. 2, pp. 351–386, 2007.

[4] A. Tawfik and A. Shalaby, "Balance function in high-energy collisions," *Advances in High Energy Physics*, vol. 2015, pp. 1–24, 2015.

[5] F. Karsch, "Determination of freeze-out conditions from lattice QCD calculations," *Central European Journal of Physics*, vol. 10, pp. 1234–1237, 2012. Proceedings, 7th International Workshop on Critical Point and Onset of Deconfinement (CPOD 2011) Wuhan, China, 2011.

[6] R. Bellwied, "Sequential hadronization and the opportunities it presents," *Journal of Physics: Conference Series.*, vol. 736, no. 1, p. 012018, 2016. Proceedings, 32th Winter Workshop on Nuclear Dynamics (WWND 2016): Guadeloupe, French West Indies, 2016.

[7] R. Bellwied, S. Borsanyi, Z. Fodor, S. Katz, and C. Ratti, "Is there a flavor hierarchy in the deconfinement transition of QCD?," *Physical Review Letters*, vol. 111, no. 20, p. 202302, 2013.

[8] R. Bellwied, S. Borsanyi, Z. Fodor, S. Katz, A. Pasztor, C. Ratti, and K. Szabo, "Fluctuations and correlations in high temperature QCD," *Physical Review D*, vol. 92, no. 11, p. 114505, 2015.

[9] R. Bellwied, J. Noronha-Hostler, P. Parotto, I. Vazquez, C. Ratti, and M. Stafford, "Freeze-out temperature from net-Kaon fluctuations at RHIC," 2018. arXiv.1805.00088v1[hep-ph].

[10] "PHOBOS experiment." https://www.bnl.gov/phobos/. Accessed: 2018-10-12.

[11] "BRAHMS experiment." http://www4.rcf.bnl.gov/brahms/WWW/. Accessed: 2018-10-12.

[12] M. Tannenbaum, "Highlights from BNL and RHIC," *Subnuclear Series*, vol. 50, pp. 347–367, 2014. Proceedings, 50th International School of Subnuclear Physics : What we would like LHC to give us (ISSP 2012): Erice, Italy, 2012.

[13] M. Anderson, J. Berkovitz, W. Betts, R. Bossingham, F. Bieser, R. Brown, M. Burks, M. Calderón De La Barca Sánchez, D. Cebra, M. Cherney, J. Chrin, W. Edwards, V. Ghazikhanian, D. Greiner, M. Gilkes, D. Hardtke, G. Harper, E. Hjort, H. Huang, G. Igo, S. Jacobson, D. Keane, S. Klein, G. Koehler, L. Kotchenda, B. Lasiuk, A. Lebedev, J. Lin, M. Lisa, H. Matis, J. Nystrand, S. Panitkin, D. Reichold, F. Retiere, I. Sakrejda, K. Schweda, D. Shuman, R. Snellings, N. Stone, B. Stringfellow, J. Thomas, T. Trainor, S. Trentalange, R. Wells, C. Whitten, H. Wieman, E. Yamamoto, and W. Zhang, "The star time projection chamber: A unique tool for studying high multiplicity events at RHIC," *Nuclear Instruments and Methods in Physics Research Section A: Accelerators, Spectrometers, Detectors and Associated Equipment*, vol. 499, no. 1-2, 2003.

[14] K. Ackermann, F. Bieser, F. Brady, D. Cebra, J. Draper, V. Eckardt, T. Eggert, H. Fessler, K. Foley, V. Ghazikhanian, T. Hallman, M. Heffner, H. Huemmler, J. Klay, S. Klein, A. Lebedev, M. LeVine, T. Ljubicic, G. L. Curto, R. Longacre, M. Oldenburg, H. Ritter, J. Romero, N. Schmitz, A. Schuettauf, J. Seyboth, P. Seyboth, M. Vidal, C. W. Jr., and E. Yamamoto, "The forward time projection chamber (FTPC) in STAR," *Nuclear Instruments and Methods in Physics Research Section A: Accelerators, Spectrometers, Detectors and Associated Equipment*, vol. 499, no. 2-3, pp. 713–719, 2003.

[15] W. Llope, F. Geurts, J. Mitchell, Z. Liu, N. Adams, G. Eppley, D. Keane, J. Li, F. Liu, L. Liu, G. Mutchler, T. Nussbaum, B. Bonner, P. Sappenfield, B. Zhang, and W.-M. Zhang", "The TOFp/pVPD time-of-flight system for STAR," *Nuclear Instruments and Methods in Physics Research Section A: Accelerators, Spectrometers, Detectors and Associated Equipment*, vol. 522, pp. 252–273, 2004.

[16] K. Ackermann, N. Adams, C. Adler, Z. Ahammed, S. Ahmad, C. Allgower, J. Amonett, J. Amsbaugh, B. Anderson, M. Anderson, E. Anderssen, H. Arnesen, L. Arnold, G. Averichev, A. Baldwin, J. Balewski, O. Barannikova, L. Barnby, J. Baudot, M. Beddo, S. Bekele, V. Belaga, R. Bellwied, S. Bennett, J. Bercovitz, J. Berger, W. Betts, H. Bichsel, F. Bieser, L. Bland, M. Bloomer, C. Blyth, J. Boehm, B. Bonner, D. Bonnet, R. Bossingham, M. Botlo, A. Boucham, N. Bouillo, S. Bouvier, K. Bradley, F. Brady, A. Brandin, R. Brown, G. Brugalette, M. Burkes, R. Cadman, H. Caines, M. C. de la

Barca Snchez, A. Cardenas, L. Carr, J. Carroll, J. Castillo, M. Castro, D. Cebra, S. Chattopadhyay, M. Chen, W. Chen, Y. Chen, S. Chernenko, M. Cherney, A. Chikanian, B. Choi, J. Chrin, W. Christie, J. Coffin, L. Conin, C. Consiglio, T. Cormier, J. Cramer, H. Crawford, I. Danilov, D. Dayton, M. DeMello, W. Deng, A. Derevschikov, M. Dialinas, H. Diaz, P. DeYoung, L. Didenko, D. Dimassimo, J. Dioguardi, C. Drancourt, T. Dietel, J. Draper, V. Dunin, J. Dunlop, V. Eckardt, W. Edwards, L. Efimov, T. Eggert, V. Emelianov, J. Engelage, G. Eppley, B. Erazmus, A. Etkin, P. Fachini, V. Faine, C. Feliciano, D. Ferenc, M. Ferguson, H. Fessler, K. Filimonov, E. Finch, Y. Fisyak, D. Flierl, I. Flores, K. Foley, D. Fritz, J. Fu, C. Gagliardi, N. Gagunashvili, J. Gans, L. Gaudichet, M. Gazdzicki, M. Germain, F. Geurts, V. Ghazikhanian, C. Gojak, J. Grabski, O. Grachov, M. Grau, D. Greiner, L. Greiner, V. Grigoriev, D. Grosnick, J. Gross, M. Guedon, G. Guilloux, E. Gushin, J. Hall, T. Hallman, D. Hardtke, G. Harper, J. Harris, M. Heffner, S. Heppelmann, T. Herston, D. Hill, B. Hippolyte, A. Hirsch, E. Hjort, G. Hoffmann, M. Horsley, M. Howe, H. Huang, T. Humanic, H. Hmmler, W. Hunt, J. Hunter, G. Igo, A. Ishihara, Y. Ivanshin, P. Jacobs, W. Jacobs, S. Jacobson, M. Janik, R. Jared, P. Jensen, I. Johnson, P. Jones, E. Judd, M. Kaneta, M. Kaplan, D. Keane, A. Khodinov, J. Kiryluk, A. Kisiel, J. Klay, S. Klein, A. Klyachko, G. Koehler, A. Konstantinov, I. Kotov, M. Kopytine, L. Kotchenda, A. Kovalenko, M. Kramer, P. Kravtsov, K. Krueger, T. Krupien, P. Kuczewski, C. Kuhn, A. Kulikov, G. Kunde, C. Kunz, R. K. Kutuev, A. Kuznetsov, L. Lakehal-Ayat, M. Lamont, J. Landgraf, S. Lange, C. Lansdell, B. Lasiuk, F. Laue, A. Lebedev, T. LeCompte, R. Lednick, W. Leonhardt, V. Leontiev, M. LeVine, Q. Li, C.-J. Liaw, J. Lin, S. Lindenbaum, V. Lindenstruth, P. Lindstrom, M. Lisa, F. Liu, L. Liu, Z. Liu, Q. Liu, T. Ljubicic, W. Llope, G. LoCurto, H. Long, R. Longacre, M. Lopez-Noriega, W. Love, D. Lynn, R. Maier, R. Majka, S. Margetis, C. Markert, L. Martin, J. Marx, H. Matis, Y. Matulenko, C. McParland, T. McShane, J. Meier, F. Meissner, Y. Melnick, A. Meschanin, M. Messer, P. Middlekamp, B. Miller, M. Miller, Z. Milosevich, N. Minaev, B. Minor, J. Mitchell, E. Mogavero, V. Moiseenko, D. Moltz, C. Moore, V. Morozov, M. de Moura, M. Munhoz, G. Mutchler, J. Nelson, P. Nevski, M. Nguyen, T. Nguyen, V. Nikitin, L. Nogach, T. Noggle, B. Norman, S. Nurushev, T. Nussbaum, J. Nystrand, G. Odyniec, A. Ogawa, C. Ogilvie, V. Okorokov, K. Olchanski, M. Oldenburg, D. Olson, G. Ott, D. Padrazo, G. Paic, S. Pandey, Y. Panebratsev, S. Panitkin, A. Pavlinov, T. Pawlak, V. Perevoztchikov, W. Peryt, V. Petrov, W. Pinganaud, S. Pirogov, E. Platner, J. Pluta, I. Polk, N. Porile, J. Porter, A. Poskanzer, E. Potrebenikova, D. Prindle, C. Pruneau, J. Puskar-Pasewicz, G. Rai, J. Rasson, O. Ravel, R. Ray, S. Razin, D. Reichhold, J. Reid, R. Renfordt, F. Retiere, A. Ridiger, J. Riso, H. Ritter, J. Roberts, D. Roehrich, O. Rogachevski, J. Romero, C. Roy, D. Russ, V. Rykov, I. Sakrejda, R. Sanchez, Z. Sandler, S. Salur, J. Sandweiss, A. Saulys, I. Savin, J. Schambach, R. Scharenberg, J. Scheblien, R. Scheetz, R. Schlueter, N. Schmitz,

L. Schroeder, M. Schulz, A. Schttauf, K. Schweda, J. Sedlmeir, J. Seger, D. Seliverstov, P. Seyboth, R. Seymour, E. Shahaliev, K. Shestermanov, S. Shimanskii, D. Shuman, V. Shvetcov, G. Skoro, N. Smirnov, L. Smykov, R. Snellings, K. Solberg, P. Sorensen, J. Sowinski, H. Spinka, B. Srivastava, E. Stephenson, R. Stock, A. Stolpovsky, N. Stone, M. Strikhanov, B. Stringfellow, H. Stroebele, C. Struck, A. Suaide, E. Sugarbaker, C. Suire, M. umbera, T. Symons, A. S. de Toledo, P. Szarwas, A. Tai, J. Takahashi, A. Tang, A. Tarchini, J. Tarzian, J. Thomas, M. Thompson, V. Tikhomirov, M. Tokarev, M. Tonjes, S. Tonse, T. Trainor, S. Trentalange, R. Tribble, V. Trofimov, O. Tsai, K. Turner, T. Ullrich, D. Underwood, I. Vakula, G. V. Buren, A. VanderMolen, A. Vanyashin, I. Vasilevski, A. Vasiliev, S. Vigdor, G. Visser, S. Voloshin, C. Vu, F. Wang, H. Ward, J. Watson, D. Weerasundara, R. Weidenbach, R. Wells, T. Wenaus, G. Westfall, J. Whitfield, C. Whitten, H. Wieman, R. Willson, K. Wilson, J. Wirth, J. Wisdom, S. Wissink, R. Witt, J. Wolf, J. Wood, N. Xu, Z. Xu, A. Yakutin, E. Yamamoto, J. Yang, P. Yepes, A. Yokosawa, V. Yurevich, Y. Zanevski, I. Zborovsk, H. Zhang, W. Zhang, D. Zimmerman, R. Zoulkarneev, and A. Zubarev", "STAR detector overview," *Nuclear Instruments and Methods in Physics Research Section A: Accelerators, Spectrometers, Detectors and Associated Equipment*, vol. 499, no. 1-2, pp. 624–632, 2003.

[17] D. Lynn, R. Bellwied, R. Beuttenmuller, H. Caines, W. Chen, D. DiMassimo, H. Dyke, D. Elliot, V. Eremin, M. Grau, G. Hoffmann, T. Humanic, I. Ilyashenko, I. Kotov, H. Kraner, P. Kuczewski, B. Leonhardt, Z. Li, C. Liaw, G. LoCurto, P. Middelkamp, R. Minor, M. Munhoz, G. Ott, S. Pandey, C. Pruneau, V. Rykov, J. Schambach, J. Sedlmeir, B. Soja, E. Sugarbaker, J. Takahashi, K. Wilson, and R. Wilson", "The STAR silicon vertex tracker: A large area silicon drift detector.," *Nuclear Instruments and Methods in Physics Research Section A: Accelerators, Spectrometers, Detectors and Associated Equipment*, vol. 447, no. 1, pp. 264–273, 2000.

[18] M. Miller, K. Reygers, S. Sanders, and P. Steinberg, "Glauber modeling in high energy nuclear collisions," *Annual Review of Nuclear and Particle Science*, vol. 57, no. 1, pp. 205–243, 2007.

[19] J. Cleymans, H. Oeschler, and K. Redlich, "Influence of impact parameter on thermal description of relativistic heavy ion collisions at GSI/SIS," *Physics Review C*, vol. 59, pp. 1663–1673, 1999.

[20] C. Patrignani and Particle Data Group, "Review of particle physics," *Chinese Physics C*, vol. 40, no. 10, p. 100001, 2016.

[21] L. Adamczyk, J. K. Adkins, G. Agakishiev, M. M. Aggarwal, Z. Ahammed, I. Alekseev, J. Alford, C. D. Anson, A. Aparin, D. Arkhipkin, E. C. Aschenauer, G. S. Averichev, J. Balewski, A. Banerjee, Z. Barnovska, D. R.

Beavis, R. Bellwied, A. Bhasin, A. K. Bhati, P. Bhattarai, H. Bichsel, J. Bielcik, J. Bielcikova, L. C. Bland, I. G. Bordyuzhin, W. Borowski, J. Bouchet, A. V. Brandin, S. G. Brovko, S. Bültmann, I. Bunzarov, T. P. Burton, J. Butterworth, H. Caines, M. Calderón de la Barca Sánchez, D. Cebra, R. Cendejas, M. C. Cervantes, P. Chaloupka, Z. Chang, S. Chattopadhyay, H. F. Chen, J. H. Chen, L. Chen, J. Cheng, M. Cherney, A. Chikanian, W. Christie, J. Chwastowski, M. J. M. Codrington, R. Corliss, J. G. Cramer, H. J. Crawford, X. Cui, S. Das, A. Davila Leyva, L. C. De Silva, R. R. Debbe, T. G. Dedovich, J. Deng, A. A. Derevschikov, R. Derradi de Souza, S. Dhamija, B. di Ruzza, L. Didenko, C. Dilks, F. Ding, P. Djawotho, X. Dong, J. L. Drachenberg, J. E. Draper, C. M. Du, L. E. Dunkelberger, J. C. Dunlop, L. G. Efimov, J. Engelage, K. S. Engle, G. Eppley, L. Eun, O. Evdokimov, R. Fatemi, S. Fazio, J. Fedorisin, P. Filip, E. Finch, Y. Fisyak, C. E. Flores, C. A. Gagliardi, D. R. Gangadharan, D. Garand, F. Geurts, A. Gibson, M. Girard, S. Gliske, D. Grosnick, Y. Guo, A. Gupta, S. Gupta, W. Guryn, B. Haag, O. Hajkova, A. Hamed, L.-X. Han, R. Haque, J. W. Harris, J. P. Hays-Wehle, S. Heppelmann, A. Hirsch, G. W. Hoffmann, D. J. Hofman, S. Horvat, B. Huang, H. Z. Huang, P. Huck, T. J. Humanic, G. Igo, W. W. Jacobs, H. Jang, E. G. Judd, S. Kabana, D. Kalinkin, K. Kang, K. Kauder, H. W. Ke, D. Keane, A. Kechechyan, A. Kesich, Z. H. Khan, D. P. Kikola, I. Kisel, A. Kisiel, D. D. Koetke, T. Kollegger, J. Konzer, I. Koralt, W. Korsch, L. Kotchenda, P. Kravtsov, K. Krueger, I. Kulakov, L. Kumar, R. A. Kycia, M. A. C. Lamont, J. M. Landgraf, K. D. Landry, J. Lauret, A. Lebedev, R. Lednicky, J. H. Lee, W. Leight, M. J. LeVine, C. Li, W. Li, X. Li, X. Li, Y. Li, Z. M. Li, L. M. Lima, M. A. Lisa, F. Liu, T. Ljubicic, W. J. Llope, R. S. Longacre, X. Luo, G. L. Ma, Y. G. Ma, D. M. M. D. Madagodagettige Don, D. P. Mahapatra, R. Majka, S. Margetis, C. Markert, H. Masui, H. S. Matis, D. McDonald, T. S. McShane, N. G. Minaev, S. Mioduszewski, B. Mohanty, M. M. Mondal, D. A. Morozov, M. G. Munhoz, M. K. Mustafa, B. K. Nandi, M. Nasim, T. K. Nayak, J. M. Nelson, L. V. Nogach, S. Y. Noh, J. Novak, S. B. Nurushev, G. Odyniec, A. Ogawa, K. Oh, A. Ohlson, V. Okorokov, E. W. Oldag, R. A. N. Oliveira, M. Pachr, B. S. Page, S. K. Pal, Y. X. Pan, Y. Pandit, Y. Panebratsev, T. Pawlak, B. Pawlik, H. Pei, C. Perkins, W. Peryt, A. Peterson, P. Pile, M. Planinic, J. Pluta, D. Plyku, N. Poljak, J. Porter, A. M. Poskanzer, N. K. Pruthi, M. Przybycien, P. R. Pujahari, J. Putschke, H. Qiu, A. Quintero, S. Ramachandran, R. Raniwala, S. Raniwala, R. L. Ray, C. K. Riley, H. G. Ritter, J. B. Roberts, O. V. Rogachevskiy, J. L. Romero, J. F. Ross, A. Roy, L. Ruan, J. Rusnak, N. R. Sahoo, P. K. Sahu, I. Sakrejda, S. Salur, A. Sandacz, J. Sandweiss, E. Sangaline, A. Sarkar, J. Schambach, R. P. Scharenberg, A. M. Schmah, W. B. Schmidke, N. Schmitz, J. Seger, P. Seyboth, N. Shah, E. Shahaliev, P. V. Shanmuganathan, M. Shao, B. Sharma, W. Q. Shen, S. S. Shi, Q. Y. Shou, E. P. Sichtermann, R. N. Singaraju, M. J. Skoby, D. Smirnov, N. Smirnov, D. Solanki, P. Sorensen, U. G. deSouza, H. M. Spinka, B. Srivastava, T. D. S. Stanislaus, J. R. Stevens, R. Stock, M. Strikhanov, B. Stringfellow,

A. A. P. Suaide, M. Sumbera, X. Sun, X. M. Sun, Y. Sun, Z. Sun, B. Surrow, D. N. Svirida, T. J. M. Symons, A. Szanto de Toledo, J. Takahashi, A. H. Tang, Z. Tang, T. Tarnowsky, J. H. Thomas, A. R. Timmins, D. Tlusty, M. Tokarev, S. Trentalange, R. E. Tribble, P. Tribedy, B. A. Trzeciak, O. D. Tsai, J. Turnau, T. Ullrich, D. G. Underwood, G. Van Buren, G. van Nieuwenhuizen, J. A. Vanfossen, R. Varma, G. M. S. Vasconcelos, A. N. Vasiliev, R. Vertesi, F. Videbæk, Y. P. Viyogi, S. Vokal, S. A. Voloshin, A. Vossen, M. Wada, M. Walker, F. Wang, G. Wang, H. Wang, J. S. Wang, X. L. Wang, Y. Wang, Y. Wang, G. Webb, J. C. Webb, G. D. Westfall, H. Wieman, S. W. Wissink, R. Witt, Y. F. Wu, Z. Xiao, W. Xie, K. Xin, H. Xu, N. Xu, Q. H. Xu, Y. Xu, Z. Xu, W. Yan, C. Yang, Y. Yang, Y. Yang, Z. Ye, P. Yepes, L. Yi, K. Yip, I.-K. Yoo, Y. Zawisza, H. Zbroszczyk, W. Zha, J. B. Zhang, S. Zhang, X. P. Zhang, Y. Zhang, Z. P. Zhang, F. Zhao, J. Zhao, C. Zhong, X. Zhu, Y. H. Zhu, Y. Zoulkarneeva, and M. Zyzak, "Energy dependence of moments of net-proton multiplicity distributions at RHIC," *Physical Review Letters*, vol. 112, no. 3, p. 032302, 2014.

[22] X. Luo, "Unified description of efficiency correction and error estimation for moments of conserved quantities in heavy-ion collisions," *Physical Review C*, vol. 91, no. 3, p. 034907, 2015.

[23] A. DasGupta, "Asymptotic theory of statistics and probability," Springer Texts in Statistics, New York, NY: Springer Verlag, 1 ed., 2008.

[24] J. Xu, "Collision Energy Dependence of Moments of Net-Kaon Multiplicity Distributions at RHIC," *Analysis note (STAR Collaboration)*, 2018. https://www.star.bnl.gov/protected/bulkcorr/xuj/. Accessed : 2018-07-21.

[25] T. Ullrich and Z. Xu, "Treatment of errors in efficiency calculations," 2007. arXiv:physics/0701199 [physics.data-an].

[26] A. Bzdak and V. Koch, "Acceptance corrections to net baryon and net charge cumulants," *Physical Review C*, vol. 86, no. 4, p. 044904, 2012.

[27] T. Nonaka, M. Kitazawa, and S. Esumi, "More efficient formulas for efficiency correction of cumulants and effect of using averaged efficiency," *Physical Review C*, vol. 95, no. 6, p. 064912, 2017.

[28] J. Adams, M. M. Aggarwal, Z. Ahammed, J. Amonett, B. D. Anderson, M. Anderson, D. Arkhipkin, G. S. Averichev, Y. Bai, J. Balewski, O. Barannikova, L. S. Barnby, J. Baudot, S. Bekele, V. V. Belaga, A. Bellingeri-Laurikainen, R. Bellwied, B. I. Bezverkhny, S. Bhardwaj, A. Bhasin, A. K. Bhati, H. Bichsel, J. Bielcik, J. Bielcikova, L. C. Bland, C. O. Blyth, S.-L. Blyth, B. E. Bonner, M. Botje, J. Bouchet, A. V. Brandin, A. Bravar, M. Bystersky, R. V. Cadman, X. Z. Cai, H. Caines, M. Calderón de la Barca Sánchez, J. Castillo, O. Catu, D. Cebra, Z. Chajecki, P. Chaloupka, S. Chattopadhyay, H. F. Chen, J. H.

Chen, Y. Chen, J. Cheng, M. Cherney, A. Chikanian, H. A. Choi, W. Christie, J. P. Coffin, T. M. Cormier, M. R. Cosentino, J. G. Cramer, H. J. Crawford, D. Das, S. Das, M. Daugherity, M. M. de Moura, T. G. Dedovich, M. DePhillips, A. A. Derevschikov, L. Didenko, T. Dietel, P. Djawotho, S. M. Dogra, W. J. Dong, X. Dong, J. E. Draper, F. Du, V. B. Dunin, J. C. Dunlop, M. R. Dutta Mazumdar, V. Eckardt, W. R. Edwards, L. G. Efimov, V. Emelianov, J. Engelage, G. Eppley, B. Erazmus, M. Estienne, P. Fachini, R. Fatemi, J. Fedorisin, K. Filimonov, P. Filip, E. Finch, V. Fine, Y. Fisyak, J. Fu, C. A. Gagliardi, L. Gaillard, J. Gans, M. S. Ganti, V. Ghazikhanian, P. Ghosh, J. E. Gonzalez, Y. G. Gorbunov, H. Gos, O. Grebenyuk, D. Grosnick, S. M. Guertin, K. S. F. F. Guimaraes, Y. Guo, N. Gupta, T. D. Gutierrez, B. Haag, T. J. Hallman, A. Hamed, J. W. Harris, W. He, M. Heinz, T. W. Henry, S. Hepplemann, B. Hippolyte, A. Hirsch, E. Hjort, G. W. Hoffmann, M. J. Horner, H. Z. Huang, S. L. Huang, E. W. Hughes, T. J. Humanic, G. Igo, P. Jacobs, W. W. Jacobs, P. Jakl, F. Jia, H. Jiang, P. G. Jones, E. G. Judd, S. Kabana, K. Kang, J. Kapitan, M. Kaplan, D. Keane, A. Kechechyan, V. Y. Khodyrev, B. C. Kim, J. Kiryluk, A. Kisiel, E. M. Kislov, S. R. Klein, D. D. Koetke, T. Kollegger, M. Kopytine, L. Kotchenda, V. Kouchpil, K. L. Kowalik, M. Kramer, P. Kravtsov, V. I. Kravtsov, K. Krueger, C. Kuhn, A. I. Kulikov, A. Kumar, A. A. Kuznetsov, M. A. C. Lamont, J. M. Landgraf, S. Lange, S. LaPointe, F. Laue, J. Lauret, A. Lebedev, R. Lednicky, C.-H. Lee, S. Lehocka, M. J. LeVine, C. Li, Q. Li, Y. Li, G. Lin, S. J. Lindenbaum, M. A. Lisa, F. Liu, H. Liu, J. Liu, L. Liu, Z. Liu, T. Ljubicic, W. J. Llope, H. Long, R. S. Longacre, M. Lopez-Noriega, W. A. Love, Y. Lu, T. Ludlam, D. Lynn, G. L. Ma, J. G. Ma, Y. G. Ma, D. Magestro, D. P. Mahapatra, R. Majka, L. K. Mangotra, R. Manweiler, S. Margetis, C. Markert, L. Martin, H. S. Matis, Y. A. Matulenko, C. J. McClain, T. S. McShane, Y. Melnick, A. Meschanin, M. L. Miller, N. G. Minaev, S. Mioduszewski, C. Mironov, A. Mischke, D. K. Mishra, J. Mitchell, B. Mohanty, L. Molnar, C. F. Moore, D. A. Morozov, M. G. Munhoz, B. K. Nandi, C. Nattrass, T. K. Nayak, J. M. Nelson, P. K. Netrakanti, V. A. Nikitin, L. V. Nogach, S. B. Nurushev, G. Odyniec, A. Ogawa, V. Okorokov, M. Oldenburg, D. Olson, M. Pachr, S. K. Pal, Y. Panebratsev, S. Y. Panitkin, A. I. Pavlinov, T. Pawlak, T. Peitzmann, V. Perevoztchikov, C. Perkins, W. Peryt, V. A. Petrov, S. C. Phatak, R. Picha, M. Planinic, J. Pluta, N. Poljak, N. Porile, J. Porter, A. M. Poskanzer, M. Potekhin, E. Potrebenikova, B. V. K. S. Potukuchi, D. Prindle, C. Pruneau, J. Putschke, G. Rakness, R. Raniwala, S. Raniwala, R. L. Ray, S. V. Razin, J. Reinnarth, D. Relyea, F. Retiere, A. Ridiger, H. G. Ritter, J. B. Roberts, O. V. Rogachevskiy, J. L. Romero, A. Rose, C. Roy, L. Ruan, M. J. Russcher, R. Sahoo, I. Sakrejda, S. Salur, J. Sandweiss, M. Sarsour, P. S. Sazhin, J. Schambach, R. P. Scharenberg, N. Schmitz, K. Schweda, J. Seger, I. Selyuzhenkov, P. Seyboth, A. Shabetai, E. Shahaliev, M. Shao, M. Sharma, W. Q. Shen, S. S. Shimanskiy, E. Sichtermann, F. Simon, R. N. Singaraju, N. Smirnov, R. Snellings, G. Sood, P. Sorensen, J. Sowinski, J. Speltz, H. M.

Spinka, B. Srivastava, A. Stadnik, T. D. S. Stanislaus, R. Stock, A. Stolpovsky, M. Strikhanov, B. Stringfellow, A. A. P. Suaide, E. Sugarbaker, M. Sumbera, Z. Sun, B. Surrow, M. Swanger, T. J. M. Symons, A. Szanto de Toledo, A. Tai, J. Takahashi, A. H. Tang, T. Tarnowsky, D. Thein, J. H. Thomas, A. R. Timmins, S. Timoshenko, M. Tokarev, T. A. Trainor, S. Trentalange, R. E. Tribble, O. D. Tsai, J. Ulery, T. Ullrich, D. G. Underwood, G. Van Buren, N. van der Kolk, M. van Leeuwen, A. M. Vander Molen, R. Varma, I. M. Vasilevski, A. N. Vasiliev, R. Vernet, S. E. Vigdor, Y. P. Viyogi, S. Vokal, S. A. Voloshin, W. T. Waggoner, F. Wang, G. Wang, J. S. Wang, X. L. Wang, Y. Wang, J. W. Watson, J. C. Webb, G. D. Westfall, A. Wetzler, C. Whitten, H. Wieman, S. W. Wissink, R. Witt, J. Wood, J. Wu, N. Xu, Q. H. Xu, Z. Xu, P. Yepes, I.-K. Yoo, V. I. Yurevich, W. Zhan, H. Zhang, W. M. Zhang, Y. Zhang, Z. P. Zhang, Y. Zhao, C. Zhong, R. Zoulkarneev, Y. Zoulkarneeva, A. N. Zubarev, and J. X. Zuo, "Scaling properties of hyperon production in $\mathrm{Au}+\mathrm{Au}$ collisions at $\sqrt{s_{NN}} = 200$ GeV," *Physics Review Letters*, vol. 98, p. 062301, 2007.

[29] X. Zhu, *Research on the Signatures of Quark-Gluon Plasma Formed in Relativistic Heavy Ion Collisions*. PhD thesis, Tsinghua University, 2007.

[30] M. Bleicher, E. Zabrodin, C. Spieles, S. Bass, C. Ernst, S. Soff, L. Bravina, M. Belkacem, H. Weber, H. Stöcker, and W. Greiner, "Relativistic hadron hadron collisions in the ultrarelativistic quantum molecular dynamics model," *Journal of Physics G: Nuclear and Particle Physics*, vol. 25, pp. 1859–1896, 1999.

[31] L. Adamczyk, J. Adams, J. Adkins, G. Agakishiev, M. Aggarwal, Z. Ahammed, N. Ajitanand, I. Alekseev, D. Anderson, R. Aoyama, A. Aparin, D. Arkhipkin, E. Aschenauer, M. Ashraf, A. Attri, G. Averichev, X. Bai, V. Bairathi, K. Barish, A. Behera, R. Bellwied, A. Bhasin, A. Bhati, P. Bhattarai, J. Bielcik, J. Bielcikova, L. Bland, I. Bordyuzhin, J. Bouchet, J. Brandenburg, A. Brandin, D. Brown, I. Bunzarov, J. Butterworth, H. Caines, M. C. de la Barca Snchez, J. Campbell, D. Cebra, I. Chakaberia, P. Chaloupka, Z. Chang, N. Chankova-Bunzarova, A. Chatterjee, S. Chattopadhyay, J. Chen, X. Chen, X. Chen, J. Cheng, M. Cherney, W. Christie, G. Contin, H. Crawford, S. Das, L. D. Silva, R. Debbe, T. Dedovich, J. Deng, A. Derevschikov, L. Didenko, C. Dilks, X. Dong, J. Drachenberg, J. Draper, L. Dunkelberger, J. Dunlop, L. Efimov, N. Elsey, J. Engelage, G. Eppley, R. Esha, S. Esumi, O. Evdokimov, J. Ewigleben, O. Eyser, R. Fatemi, S. Fazio, P. Federic, P. Federicova, J. Fedorisin, Z. Feng, P. Filip, E. Finch, Y. Fisyak, C. Flores, J. Fujita, L. Fulek, C. Gagliardi, D. Garand, F. Geurts, A. Gibson, M. Girard, D. Grosnick, D. Gunarathne, Y. Guo, S. Gupta, A. Gupta, W. Guryn, A. Hamad, A. Hamed, A. Harlenderova, J. Harris, L. He, S. Heppelmann, S. Heppelmann, A. Hirsch, G. Hoffmann, S. Horvat, X. Huang, H. Huang, T. Huang, B. Huang, T. Humanic, P. Huo, G. Igo, W. Jacobs, A. Jentsch, J. Jia, K. Jiang, S. Jowzaee,

E. Judd, S. Kabana, D. Kalinkin, K. Kang, D. Kapukchyan, K. Kauder, H. Ke, D. Keane, A. Kechechyan, Z. Khan, D. Kikoa, C. Kim, I. Kisel, A. Kisiel, L. Kochenda, M. Kocmanek, T. Kollegger, L. Kosarzewski, A. Kraishan, L. Krauth, P. Kravtsov, K. Krueger, N. Kulathunga, L. Kumar, J. Kvapil, J. Kwasizur, R. Lacey, J. Landgraf, K. Landry, J. Lauret, A. Lebedev, R. Lednicky, J. Lee, C. Li, W. Li, Y. Li, X. Li, J. Lidrych, T. Lin, M. Lisa, P. Liu, F. Liu, H. Liu, Y. Liu, T. Ljubicic, W. Llope, M. Lomnitz, R. Longacre, X. Luo, S. Luo, G. Ma, L. Ma, Y. Ma, R. Ma, N. Magdy, R. Majka, D. Mallick, S. Margetis, C. Markert, H. Matis, K. Meehan, J. Mei, Z. Miller, N. Minaev, S. Mioduszewski, D. Mishra, S. Mizuno, B. Mohanty, M. Mondal, D. Morozov, M. Mustafa, M. Nasim, T. Nayak, J. Nelson, M. Nie, G. Nigmatkulov, T. Niida, L. Nogach, T. Nonaka, S. Nurushev, G. Odyniec, A. Ogawa, K. Oh, V. Okorokov, D. Olvitt, B. Page, R. Pak, Y. Pandit, Y. Panebratsev, B. Pawlik, H. Pei, C. Perkins, P. Pile, J. Pluta, K. Poniatowska, J. Porter, M. Posik, N. Pruthi, M. Przybycien, J. Putschke, H. Qiu, A. Quintero, S. Ramachandran, R. Ray, R. Reed, M. Rehbein, H. Ritter, J. Roberts, O. Rogachevskiy, J. Romero, J. Roth, L. Ruan, J. Rusnak, O. Rusnakova, N. Sahoo, P. Sahu, S. Salur, J. Sandweiss, A. Sarkar, M. Saur, J. Schambach, A. Schmah, W. Schmidke, N. Schmitz, B. Schweid, J. Seger, M. Sergeeva, R. Seto, P. Seyboth, N. Shah, E. Shahaliev, P. Shanmuganathan, M. Shao, M. Sharma, A. Sharma, W. Shen, Z. Shi, S. Shi, Q. Shou, E. Sichtermann, R. Sikora, M. Simko, S. Singha, M. Skoby, D. Smirnov, N. Smirnov, W. Solyst, L. Song, P. Sorensen, H. Spinka, B. Srivastava, T. Stanislaus, M. Strikhanov, B. Stringfellow, T. Sugiura, M. Sumbera, B. Summa, X. Sun, Y. Sun, X. Sun, B. Surrow, D. Svirida, A. Tang, Z. Tang, A. Taranenko, T. Tarnowsky, A. Tawfik, J. Thder, J. Thomas, A. Timmins, D. Tlusty, T. Todoroki, M. Tokarev, S. Trentalange, R. Tribble, P. Tribedy, S. Tripathy, B. Trzeciak, O. Tsai, T. Ullrich, D. Underwood, I. Upsal, G. V. Buren, G. van Nieuwenhuizen, A. Vasiliev, F. Videbk, S. Vokal, S. Voloshin, A. Vossen, F. Wang, Y. Wang, G. Wang, Y. Wang, J. Webb, G. Webb, L. Wen, G. Westfall, H. Wieman, S. Wissink, R. Witt, Y. Wu, Z. Xiao, G. Xie, W. Xie, Z. Xu, N. Xu, Y. Xu, Q. Xu, J. Xu, Q. Yang, C. Yang, S. Yang, Y. Yang, Z. Ye, Z. Ye, L. Yi, K. Yip, I.-K. Yoo, N. Yu, H. Zbroszczyk, W. Zha, X. Zhang, S. Zhang, J. Zhang, J. Zhang, Z. Zhang, S. Zhang, J. Zhang, Y. Zhang, J. Zhao, C. Zhong, L. Zhou, C. Zhou, Z. Zhu, X. Zhu, and M. Zyzak, "Collision energy dependence of moments of net-kaon multiplicity distributions at RHIC," *Physics Letters B*, vol. 785, pp. 551–560, 2018.

[32] P. Alba, W. Alberico, R. Bellwied, M. Bluhm, V. Mantovani, S., M. Nahrgang, and C. Ratti, "Freeze-out conditions from net-proton and net-charge fluctuations at RHIC," *Physics Letters B*, vol. 738, pp. 305–310, 2014.

[33] V. Koch, "Hadronic fluctuations and correlations," in *Relativistic Heavy Ion*

Physics (R. Stock, ed.), vol. 23 of *Landolt-Brnstein - Group I Elementary Particles, Nuclei and Atoms (Numerical Data and Functional Relationships in Science and Technology)*, Heidelberg, Germany: Springer, Berlin, Heidelberg, 2010.

[34] P. Braun-Munzinger, A. Rustamov, and J. Stachel, "Bridging the gap between event-by-event fluctuation measurements and theory predictions in relativistic nuclear collisions," *Nuclear Physics A*, vol. 960, pp. 114–130, 2017.